Precision predictions for jet substructure



Rok Medveš

Rudolf Peierls Centre for Theoretical Physics

University of Oxford

This dissertation is submitted for the degree of

Doctor of Philosophy in Theoretical Physics

2023

To my parents, Aleksander and Tanja

Acknowledgements

First and foremost I would like to thank my supervisor, Gavin Salam for bringing me to Oxford, encouraging me to work as an independent researcher and guiding me with his endless intuition when all seemed lost. I am grateful that I have been able to learn so much from him.

I would like to also give special thanks to my closest collaborators Alba Soto-Ontoso and Gregory Soyez. I look fondly on our many hours of discussions when working on subjet multiplicity. I would additionally like to thank the rest of the PanScales collaboration, particularly Ludo and Keith, with whom I've had the great pleasure of working with.

Finally, I would like to thank Ema for being my beacon of stability, my family for their endless support, and my friends who supported me on this journey. Thank you from the bottom of my heart.

This thesis has been supported by the European Research Council (ERC) under the European Union's Horizon 2020 research and innovation programme (grant agreement No. 788223, PanScales).

Abstract

In this thesis we consider the phenomenology of Quantum Chromodynamics (QCD) in the context of precision predictions for the Large Hadron Collider (LHC). Our emphasis will be given to jets, the collimated sprays of hadrons present at high-energy colliders, their substructure, prediction and simulation.

To this end, we first introduce the fundamentals of QCD, resummation and jet substructure. We then introduce QCD parton shower event generators and the notion of their formal accuracy. We proceed to introduce two new algorithms for incorporating full-colour effects into parton showers and give particular emphasis to their testing and validation. Next, we introduce a novel algorithm for evaluating the (subjet) multiplicity at high-energy colliders called the Lund multiplicity. It is based on the Lund plane jet substructure technique and provides a simple procedure for evaluating the subjet multiplicity with an infra-red cutoff at a general collider. We first apply it to the case of e^+e^- collisions at the Large Electron Positron (LEP) collider. In this context we, for the first time, resum the average Lund and Cambridge multiplicities to next-to-next-to-double logarithmic accuracy and perform a phenomenological theory-to-data comparison with published LEP results. Finally, we extend the study to the context of high-energy jets at the LHC. Particularly, we resum their average Lund multiplicities to next-to-next-to-double logarithmic accuracy in Z+jet and inclusive jet events at the LHC. We then perform a phenomenological analysis for a realistic collider scenario and provide predictions ready for theory-to-data comparison. Alongside the phenomenological applications of this observable, the resummed average Lund multiplicities provide a necessary benchmark for testing the next generation of accurate parton showers.

Statement of Originality

This thesis is a record of the work performed during my DPhil and contains published research.

The material of Chapter 3 contains results published in Ref. [1]. This research was conducted with my co-authors Keith Hamilton, Gavin Salam, Ludovic Scyboz and Gregory Soyez. Particularly, the material covered in Sec. 3.2.2 is based on work done with Ludovic Scyboz, while the material covered in Secs. 3.2.1 and 3.2.3 contains results that I was involved in only to a lesser degree.

The material of Chapter 4 contains results published in Ref. [2]. This research was conducted with my co-authors Alba Soto-Ontoso and Gregory Soyez. Particularly, I was closely involved with all but the following aspects of the presented material: Sec. 4.4.1, particularly the running of the `Event2` generator. Fig. 4.9a, particularly the running of the Herwig7.2 and Sherpa2.2 event generators.

The material of Chapter 5 contains results published in Ref. [3]. This research was conducted with my co-authors Alba Soto-Ontoso and Gregory Soyez. Particularly, I was closely involved with all but the following aspects of the presented material: anything requiring the running of the `NLOJet++` or `MadGraph` event generators. More specifically, this includes the material of Sec. 5.2.3.1, the computation of the values in Tab. 5.2, and the computation of $\langle \overline{N^{(\text{Lund})}} \rangle_{\text{fo}}$ contributing to Eq. (5.3.2) and Fig. 5.5. Furthermore, I was not involved with the running of the Herwig7.2 and Sherpa2.2 event generators which contributed to Fig. 5.6a.

Finally, I was closely involved with all but the following aspects of the material presented in Appendix A: the numerical simulations which produced Fig. A.1, and Fig. A.2.

Contents

1 Introduction **1**

2 Theoretical Framework **4**

2.1 Quantum Chromodynamics 4

2.1.1 The QCD Lagrangian 4

2.1.2 Running of the QCD coupling 6

2.1.3 Soft and collinear factorisation 7

2.1.4 Colour coherence and angular ordering 9

2.1.5 Local parton-hadron duality and collinear factorisation . . . 10

2.2 Jets in high-energy collisions 11

2.2.1 Jet clustering algorithms 12

2.2.2 The Lund diagram 16

2.3 Resummation 18

2.3.1 The Lund plane and logarithmic counting 21

3 Parton shower accuracy and colour **23**

3.1 Overview of parton showers and their accuracy 24

3.2 Colour in final-state dipole parton showers 27

3.2.1 Segments, NODS, CFFE 29

3.2.2 Matrix element tests 31

3.2.3 Numerical tests for observables: Particle multiplicity 35

3.3 Parton showers beyond NLL accuracy 39

4 Lund multiplicity in e^+e^- collisions **41**

4.1 Lund multiplicity algorithm in e^+e^- collisions 41

4.2 Revisiting DL and NDL results 44

4.2.1 Double-logarithmic (DL) accuracy 44

4.2.2 Next-to-double-logarithmic (NDL) accuracy 49

4.3 Calculation at NNDL accuracy 56

4.3.1 Contributions and master formula 56

4.3.2 Corrections involving a pure α_s contribution 63

4.3.3 Corrections involving two $\alpha_s L$ factors 75

4.3.4 Corrections involving the running of the strong coupling . . 84
4.3.5 Final result 87
4.4 Validation and phenomenology 92
4.4.1 Fixed-order validation 92
4.4.2 Matching with fixed-order 94
4.4.3 Comparison to LEP data 97

5 Lund multiplicity in *pp* collisions **100**
5.1 Lund multiplicity algorithm in *pp* collisions 101
5.2 Calculation of the average Lund multiplicity in jets 102
5.2.1 DL accuracy 103
5.2.2 NDL accuracy 104
5.2.3 NNDL accuracy 108
5.2.4 Final result 119
5.2.5 From fixed kinematics to fiducial cuts 120
5.3 Numerical results 122
5.3.1 Resummation 122
5.3.2 Phenomenological predictions 125

6 Conclusions **131**

Appendices

A Additional consideration for Lund multiplicity **136**
A.1 Angular ordered vs k_t-based clustering algorithms 136
A.2 Recombination scheme independence 137
A.3 The Cambridge jet multiplicity 138

References **143**

1 Introduction

Since the discovery of the Higgs Boson in July 2012 at the Large Hadron Collider (LHC), and the confirmation of the Standard Model of particle physics, increasing efforts have been poured into stress-testing its validity in what has widely been called the "precision LHC era". The aim of the precision LHC programme is to compare high-precision experimental measurements [4–6] with highly accurate theoretical predictions of the Standard Model in order to experimentally establish all aspects of it, and to potentially find a discrepancy and thus sign of new physics.

In the Standard Model, Quantum Chromodynamics (QCD), the theory of the strong interaction, contributes significantly to collider processes, governing both the initial-state collision conditions through the substructure of the proton, and final measurement through the intrinsic splitting and hadronisation mechanisms which produce final-state hadrons. Particularly, QCD is responsible for the formation of final-state collimated sprays of hadronic radiation known as "jets", the most abundant objects at the LHC. Their formation is tied to the *parton shower*, a mechanism by which particles, participating in a high-energy collision, lose their energy through a sequence of iterated splittings.

Experimentally, the imprint of the parton shower can be seen through measuring and analysing the jet's substructure. Particularly, in recent years, jet substructure has become an intense field of research, receiving significant scrutiny from both the

experimental [7] and theoretical [8] communities. It has been successfully applied to problems such as precision phenomenology, (boosted) jet tagging, parton shower testing, as well as machine learning. Key to these efforts is the ability of the theoretical community to accurately model QCD, which can either be performed through dedicated analytical methods or generic numerical ones. In this thesis we contribute to both of these aspects. We develop new precision physics observables applicable to current and future colliders based on jet substructure, as well as comment on how to improve and test numerical tools for simulating jet substructure.

The thesis is organised as follows. In Chap. 2 we begin by introducing the fundamentals of QCD, jet substructure, and resummation. In Chap. 3 we comment on Monte Carlo parton shower event generators, which due to their flexibility are a staple tool in experimentalists' arsenals. Particularly, we address and contribute to the recent developments on parton shower accuracy by introducing two new algorithms which reintroduce full-colour information into parton showers and validate their implementation. In Chap. 4 we develop a new observable for precision physics based on jet substructure called the *Lund multiplicity*. It provides the simplest collider-generic way to evaluate the subjet multiplicity with an infra-red (IR) cutoff. In this chapter, we focus on its application at e^+e^- colliders and for the first time resum the average Lund and Cambridge multiplicities in $e^+e^- \to q\bar{q}$ and $e^+e^- \to gg$ events up to next-to-next-to-double-logarithmic accuracy, an order higher than what was available in the literature previously. Using these results we perform a phenomenological study and compare the measured average Cambridge multiplicities at LEP to our computation. In Chap. 5 we extend the previous study by considering the average Lund multiplicity in the context of a pp collider, such as the LHC. Most significantly, we compute, for the first time, the next-to-next-to-double logarithmic resummation of the average subject multiplicity at the LHC. The final phenomenological predictions, which we specialise to the case of Z+jet events and inclusive jet samples is ready for theory-to-data analysis, thus contributing to the precision LHC physics programme. Furthermore, the above resummed results provide key benchmarks for testing the future generations of accurate parton shower

event generators. We conclude our discussion in Chap. 6 and comment on some subtleties relating to Lund multiplicities in App. A.

2
Theoretical Framework

The basis of this thesis is the discussion of Quantum Chromodynamics (QCD), its phenomenological implications, computation and simulation. In this chapter we introduce the basic concepts that will inform our discussion in later chapters.

2.1 Quantum Chromodynamics

2.1.1 The QCD Lagrangian

QCD, the theory of the strong interaction, is a gauge theory with the gauge group $SU(3)$. It's Lagrangian is given by

$$\mathcal{L}_{\text{QCD}} = \sum_f \bar{\psi}_{f,i}(i\gamma_\mu D^\mu_{ij} - \delta_{ij} m_f)\psi_{f,j} - \frac{1}{4} F^A_{\mu\nu} F^{A\,\mu\nu}. \tag{2.1.1}$$

In Eq. (2.1.1) $\psi_{f,i}$ are the quark fields which are in the fundamental representation of the $SU(3)$ group. The subscript $f = 1, 2, \ldots, n_f$ indexed the flavour of the quarks up to n_f number of flavours, and $i = 1, 2, 3$ corresponds to the colour indices. We note that throughout the thesis we will be working in a limit where for $f = 1, \ldots, 5$, all quarks are taken to be massless, $m_f = 0$. The covariant derivative D^μ_{ij} is defined as

$$D^\mu_{ij} = \delta_{ij}\partial^\mu + i g_s A^\mu_B t^B_{ij}, \tag{2.1.2}$$

where A^{μ}_{B} are the gluon fields, which transform in the adjoint representation of $SU(3)$, with $B = 1, 2, ..., 8$. The matrices t^{B}_{ij} are the generators of the $SU(3)$ (colour) algebra in the fundamental representation, which satisfy

$$[t^{A}, t^{B}]_{ab} = if^{ABC}t^{C}_{ab}, \tag{2.1.3}$$

with f^{ABC} the structure constants of the $SU(3)$ group. Furthermore, in Eq. (2.1.1), the field strength tensor is defined as $F^{A}_{\mu\nu} = \partial_{\mu}A^{A}_{\nu} - \partial_{\nu}A^{A}_{\mu} - g_{s}f^{ABC}A^{B}_{\mu}A^{C}_{\nu}$, with g_{s} the QCD coupling. We note here some commonly occurring identities which will be useful in future chapters

$$\begin{aligned} \mathrm{Tr}\left[t^{A}_{ik}t^{B}_{kj}\right] &= T_{R}\delta^{AB}, \qquad T_{R} = \frac{1}{2}, \\ \sum_{A} t^{A}_{ik}t^{A}_{kj} &= C_{F}\delta_{ij}, \qquad C_{F} = \frac{N_{\mathrm{C}}^{2}-1}{2N_{\mathrm{C}}} = \frac{4}{3}, \\ \mathrm{Tr}\left[T^{C}_{AB}T^{D}_{BE}\right] = \sum_{AB} f^{ABC}f^{ABD} &= C_{A}\delta^{DC}, \qquad C_{A} = N_{\mathrm{C}} = 3, \end{aligned} \tag{2.1.4}$$

where $(T^{A})_{BC} \equiv -if^{ABC}$ are the generators of the $SU(3)$ algebra in the adjoint representation. Note that we have left the number of colours (N_{C}=3) explicit in Eq. (2.1.4) so as to facilitate discussion in later chapters. We will commonly call the parameters T_{R}, C_{F}, and C_{A} "colour factors".

Since QCD is a gauge theory, one must ensure that it is invariant under local $SU(3)$ gauge transformations. That is, one must guarantee that the physical content of the theory is preserved under $SU(3)$ redefinition of the quark fields

$$\psi_{a}(x) \to \psi'_{a}(x) = \exp\left(ig_{s}t^{B}\theta_{B}(x)\right)_{ab}\psi_{b}(x) \equiv U_{ab}(x)\psi_{b}(x). \tag{2.1.5}$$

Correspondingly, to guarantee that Eq. (2.1.1) remains invariant under the above transformations, the following transformations also hold

$$D_{\mu} \to D'_{\mu} = U(x)D_{\mu}U^{\dagger}(x), \tag{2.1.6a}$$

$$t^{B}A^{B}_{\mu} \to t^{B}A^{B\prime}_{\mu} = U(x)t^{B}U^{\dagger}(x)\,A^{B}_{\mu} + \frac{i}{g_{s}}(\partial_{\mu}U(x))U^{\dagger}(x), \tag{2.1.6b}$$

$$F^{A}_{\mu\nu} \to F^{A\prime}_{\mu\nu} = U(x)F^{A}_{\mu\nu}U^{\dagger}(x), \tag{2.1.6c}$$

where we have omitted the colour (triplet) indices in the above equation for readability. While Eqs. (2.1.6) are enough to guarantee the gauge invariance

of the QCD Lagrangian, one still needs to remove the gauge redundancy in the theory by choosing a gauge. The gauge fixing procedure can be reviewed in standard QCD textbooks, for example Ref. [9], and we choose not to discuss it here as it will not play an important role in our discussions going forward.

2.1.2 Running of the QCD coupling

Beyond the leading order in perturbation theory one must include both real emissions as well as "virtual" loop diagrams, consistently keeping track of the powers in the strong coupling constant

$$\alpha_s = \frac{g_s^2}{4\pi}. \tag{2.1.7}$$

It is well known that including loop diagrams leads to the appearance of ultraviolet (UV) divergences, which need to be renormalised in order to guarantee the consistency of the theory. A consequence of renormalising QCD, for example in dimensional regularisation, is that the strong coupling, Eq. (2.1.7), gains a scale dependence on an unphysical parameter μ. This dependence is described by the Renormalisation Group Equations

$$\mu^2 \frac{\partial \alpha_s(\mu^2)}{\partial \mu^2} = \beta\left(\alpha_s(\mu^2)\right), \tag{2.1.8}$$

where β is the beta function, given in terms of a power expansion in α_s

$$\beta\left(\alpha_s(\mu^2)\right) = -\alpha_s^2(\mu^2)\left(\beta_0 + \alpha_s\beta_1 + \dots\right), \tag{2.1.9}$$

which is known up to 5 loops [10–14]. We will refer to this dependence of α_s on μ as "the running of the coupling". A key property of the beta function, Eq. (2.1.9), is that it is always negative, $\beta(\alpha_s) < 0$, leading to a decrease of $\alpha_s(\mu^2)$ as μ increases. This means that QCD is asymptotically free, allowing us to use quarks and gluons as the relevant quantum states for performing perturbative calculations down to some energy scale, called the *hadronisation scale*, where $\alpha_s(\mu^2)$ would become of order 1. Below this scale, the mechanisms governed by QCD become intrinsically non-perturbative. A good proxy for the hadronisation scale is the QCD Landau

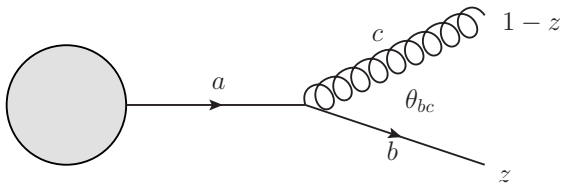


Figure 2.1: Representation of a soft-and-collinear $q \to qg$ splitting.

pole, defined by $\alpha_s(\Lambda_{\text{QCD}}) = \infty$, at some value Λ_{QCD}. This value is renormalisation-scheme dependant, and we quote here the $\overline{\text{MS}}$ value of $\Lambda_{\text{QCD}} = 341\,\text{MeV}$, extracted from ($n_f = 3$) Lattice QCD [15].

A further remark regarding $\alpha_s(\mu^2)$ is the choice of the parameter μ. For measurements of α_s, it is most common to quote its value on the Z-mass pole, $\alpha_s(M_Z^2) = 0.1179 \pm 0.0009$ [16]. However, when computing collider observables, such as cross-sections, it is more advantageous to choose μ as some physical scale in the problem. Throughout this thesis we will be making two common choices: in cases where we consider fixed-order computation of collider observables, we will set μ to some physical scale, such as the collision centre-of-mass energy $\mu = \sqrt{s}$. This choice ensures that the contributions from higher orders in α_s do not come with particularly large logarithms of $\ln(\sqrt{s}/\mu)$. Alternatively, when we will be considering the contributions of individual emissions to an observable in the context of all-order resummation or parton shower simulations, we will set $\mu = k_t$, where k_t is the measure of an emission's transverse momentum.

2.1.3 Soft and collinear factorisation

In this section we briefly review a useful result in perturbative QCD. That is, when considering emissions at largely separated scales, their matrix elements, phase spaces and differential cross-sections factorise.

To make the discussion concrete, we consider a generic collider process, characterised by the grey circle in Fig. 2.1 with matrix element $\mathcal{M}_n$, with an outgoing massless quark leg a which splits into a quark b and gluon c. This process' matrix element is given by $\mathcal{M}_{n+1}$. We assume that the $a \to bc$ splitting happens in the collinear limit, where the relative angle θ_{bc} in much smaller than any other

angle in the system, or alternatively, $\theta_{bc} \to 0$. In such a limit, we parametrise $E_b = zE_a$, $E_c = (1-z)E_a$, where z is the momentum fraction remaining after the gluon splitting. Computing the spin-and-colour-averaged squared matrix element for the process in Fig. 2.1 yields [9]

$$|\mathcal{M}_{n+1}|^2 \approx |\mathcal{M}_n|^2 \, \frac{8\pi\alpha_s}{z(1-z)E_a^2\theta_{bc}^2} P_{qq}(z); \qquad P_{qq}(z) = C_F \frac{1+z^2}{1-z}, \tag{2.1.10}$$

where $P_{qq}(z)$ is known as the $(q \to qg)$ splitting function, and the scale of the running coupling is implicitly evaluated at $k_t = \min(E_b, E_c)\theta_{bc}$. A key insight of Eq. (2.1.10) is that for sufficiently collinear splittings, the matrix element for an additional splitting ($|\mathcal{M}_{n+1}|^2$) factorises away from the rest of squared amplitude ($|\mathcal{M}_n|^2$, associated with the grey circle in Fig. 2.1). Furthermore, the phase space for $n+1$ emissions similarly factorises into the phase space for n emissions, times the phase space for one emission,

$$\mathrm{d}\Phi_{n+1} \approx \mathrm{d}\Phi_n \times \mathrm{d}\Phi_1 = \mathrm{d}\Phi_n \times \frac{z(1-z)E_a^2}{4(2\pi)^3} \, \mathrm{d}\theta_{bc}^2 \, \mathrm{d}z \, \mathrm{d}\phi. \tag{2.1.11}$$

Putting together Eq. (2.1.10) and Eq. (2.1.11), we find that the differential cross-section for the $q \to qg$ process factorises as

$$\mathrm{d}\sigma_{n+1} \approx \mathrm{d}\sigma_n \, \frac{\alpha_s}{2\pi} \frac{\mathrm{d}\theta^2}{\theta^2} \, P_{qq}(z) \, \mathrm{d}z, \tag{2.1.12}$$

where we have averaged over the ϕ coordinate.

Two important remarks are in order regarding the above equations. First, the form of Eq. (2.1.12) is universal, that is, it holds also for $q \to qg$, $g \to gg$, as well as $g \to q\bar{q}$ splitting. The choice of particular process is reflected in the content of the collinear splitting function, $P_{ab}(z)$, which equals

$$P_{qq}(z) = C_F \frac{1+z^2}{1-z}, \tag{2.1.13a}$$

$$P_{gg}(z) = C_A \left[\frac{1-z}{z} + \frac{z}{1-z} + z(1-z) \right], \text{ and} \tag{2.1.13b}$$

$$P_{qg}(z) = T_R \left[z^2 + (1-z)^2 \right], \tag{2.1.13c}$$

for $q \to qg$, $g \to gg$ and $g \to q\bar{q}$ processes respectively. Second, Eqs. (2.1.12) and (2.1.13) show that massless splittings suffer from infra-red (IR) divergences

when $\theta \to 0$ or $z \to 1$ (with the exception for $g \to q\bar{q}$ splittings, which do not suffer from a $z \to 1$ divergence). Indeed, for any of the three processes, integrating inclusively over $\mathrm{d}z$ and $\mathrm{d}\theta^2$ would produce logarithmic divergences. We note that these divergences vanish after summing over both real and virtual diagrams as a consequence of the KLN theorem [17, 18].

2.1.4 Colour coherence and angular ordering

In this section we review colour coherence, which asserts that soft-large-angle emissions also factorise from the hard process, similarly to collinear emissions as discussed in the previous section. Furthermore, these soft emissions can only be emitted at certain angles, due to a property called *angular ordering* [19–23].

We consider a generic final-state event with n outgoing massless legs, the differential cross-section for which is given by $\mathrm{d}\sigma_n$. The differential cross-section for emitting a soft gluon g with momentum k from this configuration, with energy E much smaller than any other energy in the system, is given by [9]

$$\mathrm{d}\sigma_{n+1} = \mathrm{d}\sigma_n \frac{\alpha_s}{2\pi}\frac{\mathrm{d}E}{E}\frac{\mathrm{d}\phi}{2\pi}\mathrm{d}\cos\theta \sum_{i,j}(-2T_i \cdot T_j)(k|p_i p_j), \text{ with} \tag{2.1.14}$$
$$(k|p_i p_j) = E_k^2 \frac{(p_i \cdot p_j)}{(p_i \cdot k)(p_j \cdot k)},$$

where ϕ and θ are the azimuthal and polar angles respectively, the sum i, j runs over distinct pairs of particles in the event, and T_i represents the colour charges associated with particle i. Concretely, when i is a quark (gluon), $T_q = t$ ($T_g = T$) corresponds to the $SU(3)$ algebra generator in the fundamental (adjoint) representation such that $T_q^2 \equiv C_F$ ($T_g^2 \equiv C_A$), in line with Eq. (2.1.4). Furthermore, we note that the reference direction defining ϕ and θ can freely be specified on a per-integral basis as a consequence of Lorentz invariance. Finally, we note that the functions $(k|p_i p_j)$ are sometimes called antenna functions.

The antenna function defined in Eq. (2.1.14), which encodes the interference contributions from lines i and j, has two collinear divergences – one associated with

$\theta_{ki} \to 0$, and another associated with $\theta_{kj} \to 0$. One can make these divergences explicit in the antenna function by defining

$$\begin{aligned}(k|p_i p_j) &= (k|p_i p_j)_{[i]} + (k|p_i p_j)_{[j]}, \qquad \text{with} \\ (k|p_i p_j)_{[i]} &= \frac{1}{2}\left((k|p_i p_j) + \frac{1}{1-\cos\theta_{ki}} - \frac{1}{1-\cos\theta_{kj}}\right),\end{aligned} \tag{2.1.15}$$

and analogously for $(k|p_i p_j)_{[j]}$. We note that the function $(k|p_i p_j)_{[i]}$ now only has a collinear divergence when $\theta_{ki} \to 0$. More importantly, these functions follow a remarkable property known as angular ordering. Averaging $(k|p_i p_j)_{[i]}$ over the azimuthal angle ϕ_{ki}, defined in reference to $\vec{p}_i$, one can find that (for a proof see e.g. [9])

$$\int_0^{2\pi} \frac{\mathrm{d}\phi_{ki}}{2\pi} (k|p_i p_j)_{[i]} = \begin{cases} 1/(1-\cos\theta_{ki}), & \text{if } \theta_{ki} \leq \theta_{ij} \\ 0, & \text{otherwise,} \end{cases} \tag{2.1.16}$$

that is, soft emissions are confined to a cone of relative size θ_{ij} around each pair of emitting legs i, j. The angular ordering property of soft emissions goes hand in hand with QCD colour coherence, which states that gluons emitted at angles $\theta_{ki}, \theta_{kj} > \theta_{ij}$, cannot resolve the individual i and j partons' colour charges, but rather only their collective colour charge.

2.1.5 Local parton-hadron duality and collinear factorisation

Up until now we have mostly been concerned with the properties of QCD in the perturbative regime, valid at energies above Λ_{QCD}. However, in realistic collider processes, one does not measure quarks and gluons as asymptotic final or initial states, but rather confined, colourless, hadrons. In this section we connect the descriptions provided by perturbative QCD calculations to realistic collider samples.

In the case of final-state particles, partons remain a good proxy for hadrons as long as we consider observables which probe scales sufficiently above Λ_{QCD}. This property is called *local parton-hadron duality* [24], and asserts that hadronisation only slightly modifies or disturbs the flow of momentum and quantum numbers established at parton level. For example, it has been observed that hadronisation typically

reduces a QCD jet's $p_\perp$ only by $\mathcal{O}(1\text{ GeV})$ [25], typically a $\sim 1\%$ effect. Thus, for the remainder of the thesis, we will describe calculations in perturbative QCD, keeping in mind that the final results are applicable also to realistic collider scenarios.

For the case of initial-state particles, for example colliding pp bunches at the LHC, one can relate the initial-state hadrons to initial-state partons via the collinear factorisation theorem [26, 27]. It states that the hadronic cross-section σ for two colliding hadrons with momenta p_1, p_2, and squared centre-of-mass energy $s = (p_1 + p_2)^2$ is related to its partonic counterpart, $\hat{\sigma}$, up to power corrections in $\Lambda_{\text{QCD}}/\sqrt{s}$, via a convolution with parton distribution functions (PDFs)

$$\sigma(p_1, p_2, s) = \sum_{a,b} \int_{Q^2/s}^{1} \mathrm{d}x_1 \mathrm{d}x_2 \, f_a(x_1, \mu_F^2) f_b(x_2, \mu_F^2) \, \hat{\sigma}_{ab}(x_1 p_1, x_2 p_2, Q^2, \mu_F^2), \quad (2.1.17)$$

where the sum is performed over all parton constituents a, b of the in-coming hadrons, $x_{1,2}$ are the momentum fractions being carried by the partons, $f(x_i, \mu_F^2)$ are the parton distribution functions parametrising the partonic content of the hadrons, Q represents the partonic centre-of-mass energy, and μ_F^2 the so-called factorisation scale, which, similarly to the renormalisation scale, is typically chosen to be some hard scale in the problem.

Using Eq. (2.1.17), it's differential counterpart, and local parton-hadron duality, one can thus compute collider observables in partonic processes and straightforwardly relate them to experimentally-measurable, hadronic, ones.

2.2 Jets in high-energy collisions

We now consider the phenomenological implications of QCD at high energy colliders. Fig. 2.2 shows a visual representation of a sample proton-proton collider event. It begins with two colliding protons. Due to the factorisation theorem described in Sec. 2.1.5, we imagine that two partons, in the case of Fig. 2.2 a gluon and a quark (blue lines), get 'picked' from each proton, which then participate in the hard collision (blue box). The resulting out-going final-state partons have an energy significantly above Λ_{QCD}, and thus continue to fragment in a process called the parton shower (red lines). We note that due to the logarithmically-divergent nature of the QCD

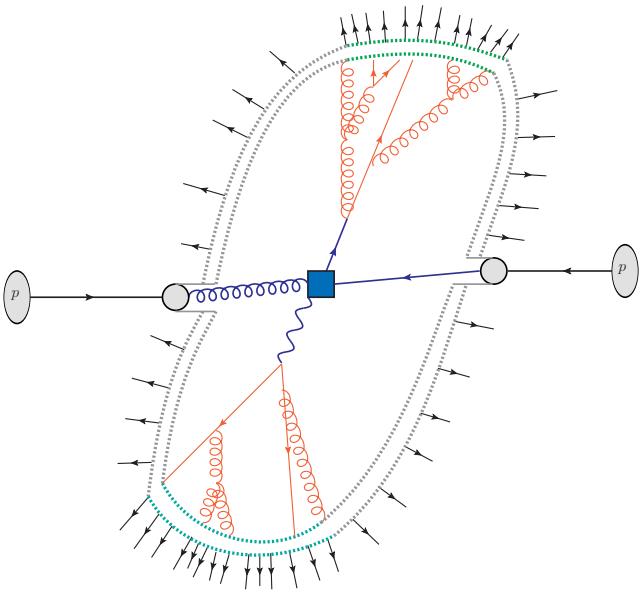


Figure 2.2: The anatomy of a proton-proton collision. A gluon and quark (blue lines), each originating from a proton, participate in a $2 \to 2$ hard collision (blue box). The resulting particles continue to fragment in the parton shower (red lines) until hadronising (dotted boundary).

matrix element, Eq. (2.1.10), soft and collinear splittings dominate in this process, thus leading to a collimated spray of particles, known as a *jet*. As the system evolves and the relevant energy scales become of order Λ_{QCD}, the system begins to hadronise. After hadronisation the partonic jets produced in the parton shower become hadronic jets as can intuitively be understood through local parton-hadron duality.

2.2.1 Jet clustering algorithms

Hadronic jets are some of the most common objects to appear in collider events [8] and have a rich structure which probes QCD at multiple scales. One of the most important roles a jet plays in collider physics is that it provides a well-defined object which can be calculated in perturbative QCD and measured at a high-energy collider. The backbone of this is the concept of infrared-and-collinear (IRC) safety, which in the context of jet definitions asserts that soft or collinear unresolved emissions do not spoil the definition of a jet.

Jets can be defined through a variety of ways, see Ref. [25] for a review. Commonly, jets are defined through a recursive clustering sequence which, given

an event of n particles, finds a pair of particles i, j which minimises some distance measure d_{ij}, which is then compared to a jet resolution parameter d_{cut}. Typically, if $d_{ij} < d_{\text{cut}}$, the particles i, j are recombined into a pseudojet, otherwise, they are deemed to be part of a different jet. We note that the recombination procedure is not unique and thus subject to what is known as a recombination scheme. Unless stated otherwise, we will use the so-called E-scheme, in which the four-momenta of the particles i, j are summed together, $p_{ij}^{\text{recombined}} = p_i + p_j$.

2.2.1.1 The Durham algorithm

One of the simplest sequential recombination jet algorithms was given in Ref. [28] in the context of e^+e^- collisions. Today, it is called the Durham algorithm, or the e^+e^--k_t algorithm due to using a distance measure proportional to k_t^2. Given a collider event in the e^+e^- centre-of-mass-frame, it is defined as follows:

1. For every pair of objects i, j, compute the corresponding separation y_{ij}, defined by

$$y_{ij} = 2\min\left(E_i^2, E_j^2\right)(1 - \cos\theta_{ij})/Q^2. \tag{2.2.1}$$

   where Q denotes the centre-of-mass collision energy, E_i the energy of particle i, and θ_{ij} the angle between particles i and j.

2. Find the minimum y_{min} of all the y_{ij}.

3. If y_{min} is below some jet resolution y_{cut}, then recombine particles i and j and repeat from step 1.

4. Otherwise, declare all remaining particles in the event to be jets and terminate the procedure.

It is simple to demonstrate that this prescription yields IRC-safe jets. For example, at parton level, adding an arbitrarily soft gluon g to a collection of n particles would cause that gluon to have the smallest distance measure y_{gj} in the event, where the particle j corresponds to the particle closest in angle to g. Thus, it would be

recombined with particle j, yielding a collection of n particles. Furthermore, due to the soft nature of g, the overall kinematics would be unmodified compared to the case where g is not added to the event, thus satisfying IR safety. On the other hand, were we to have added an arbitrarily collinear splitting to a collection of n particles, $\tilde{i} \to ij$, we would again be in a situation where y_{ij} was the smallest in the event. Thus, after recombining i and j we would again recover the original kinematics of the system, satisfying collinear safety.

2.2.1.2 The Cambridge algorithm

While the Durham algorithm, Sec. 2.2.1.1, has many powerful properties, it does not have good non-perturbative behaviour and is prone to misclustering, impeding jet substructure studies [29]. Due to this, a new e^+e^- algorithm was introduced in Ref. [29] which amended some of these issues by ensuring that particles close in angle cluster first, and that soft "junk jet" formation is suppressed.

The Cambridge algorithm is a sequential recombination algorithm which utilises two distance measures between particles. First, $v_{ij} = 2(1 - \cos\theta_{ij})$ (i.e. the squared angle in the small-angle limit) is used, then the measure defined in Eq. (2.2.1). Specifically, given a given a collider event it is defined as follows:

1. If only one particle is left, call it a jet and stop.
2. Otherwise, find the pair of particles i, j with the smallest v_{ij}, i.e. which are closest in angle.
3. If the corresponding $y_{ij} < y_{\text{cut}}$, recombine i and j and repeat from step 1.
4. Otherwise, take the less energetic of i and j, remove it from the list of particles and call it a jet. Then, repeat from step 1.

On the surface, this algorithm seems like a simple extension of the Durham algorithm. However, clustering particles with respect to angular proximity connects the Cambridge clustering sequence to the concept of angular ordering, Sec. 2.1.4, which ensures excellent theoretical behaviour. Thus, the Cambridge algorithm has been one of the most widely adopted algorithms in e^+e^- collisions.

2.2.1.3 The Cambridge/Aachen algorithm

We now discuss algorithms which are primarily designed for hadron colliders. In this case, it is standard to view the event in frame of the hadronic collision and to use variables which are invariant under longitudinal boosts along the beam axis. To define the algorithm, we first define a particle i's transverse momentum, $p_{\perp,i}$, as the component of it's three-momentum perpendicular to the beam. Second, we define it's azimuthal angle with respect to the beam as ϕ_i, defined between $[-\pi, \pi]$. Finally, we define it's rapidity as $y_i = \frac{1}{2} \ln \left(\frac{E+p_z}{E-p_z} \right)$, where the z axis is taken along the beam direction. We note that for massless particles, which we will mostly be considering throughout this thesis, y_i is equal to the pseudo-rapidity $\eta_i = -\ln(\tan(\theta_{iB}/2))$, and $p_{\perp,i} = E_i \sin\theta_{iB}$, where θ_{iB} is the angle between the beam and the particle i.

With these variables, we define the so-called Cambridge/Aachen algorithm, which takes inspiration for the Cambridge algorithm, and was originally defined in deep inelastic scattering in Ref. [30]. Today it is most often used in the context of hadron-hadron collisions using the distance measures

$$d_{ij} = \frac{\Delta R_{ij}^2}{R^2}, \qquad \Delta R_{ij}^2 = (y_i - y_j)^2 + (\phi_i - \phi_j)^2, \qquad d_{iB} = 1, \tag{2.2.2}$$

where d_{ij} defines the distance between particles i and j, d_{iB} defines the distance between the beam and particle i, and ΔR_{ij}^2 is a boost-invariant measure of the relative angular distance between particles i and j.[1] The parameter R in Eq. (2.2.2) is a free parameter which we call the "jet radius". Given these measures, the Cambridge/Aachen algorithm is defined as follows:

1. Work out the distances d_{ij} for all pairs of particles and d_{iB} for each particle in the event.

2. Find the minimum of the d_{ij} and d_{iB}.

3. if $d_{ij} < d_{iB}$, then recombine i and j into a pseudojet and return to step 1.

[1] Indeed, it is possible to show in the collinear limit $\theta_{ij} \to 0$ that $\Delta R_{ij}^2 \to \theta_{ij}^2 / \sin^2(\theta_{iB})$.

4. Otherwise, if $d_{iB} < d_{ij}$, then declare i to be a final-state jet, and remove it from the list of particles. Then return to step 1.

5. Stop when no particles remain.

In effect the Cambridge/Aachen jet algorithm clusters all particles into jets which are separated by an angular distance $\Delta R_{ij}^2 > R^2$. Due to the algorithm clustering particles in terms of angular proximity, the Cambridge/Aachen algorithm also enjoys good theoretical and physical properties as a consequence of angular ordering, Sec. 2.1.4.

2.2.1.4 The anti-k_t algorithm

Finally, we describe the most widely used sequential jet clustering algorithm in experiments called the anti-k_t algorithm [31]. It generalises the approach of the Cambridge/Aachen algorithm from Sec. 2.2.1.3, using the exact same clustering procedure, but opts to use the following distance measures instead

$$d_{ij} = \min(p_{\perp,i}^{-2}, p_{\perp,j}^{-2}) \frac{\Delta R_{ij}^2}{R^2}, \quad \Delta R_{ij}^2 = (y_i - y_j)^2 + (\phi_i - \phi_j)^2, \quad d_{iB} = p_{\perp,i}^{-2}. \tag{2.2.3}$$

Due to the modified distance measure, this algorithm ensures that soft particles cluster around hard "seeds" first, preferentially producing circular jets in the (ϕ, y) plane.

2.2.2 The Lund diagram

At the Large Hadron Collider (LHC), jet formation happens between the $\mathcal{O}(1\text{ TeV})$ and $\mathcal{O}(\Lambda_{\text{QCD}})$ scales, spanning three orders of magnitude. The imprint of this formation process can be seen in the jet's substructure, which has, in recent years, seen thorough theoretical and experimental scrutiny [7, 8]. For example, jet substructure has frequently been utilised for tagging jets, machine learning, and constructing precision observables, which can be used to test QCD experimentally. A more refined construction, inspired by Lund diagrams [32], which visualise the substructure of a jet in a 2D representation, was introduced in Ref. [33]. Dubbed the "Lund jet plane", it maps the available emission phase-space in a jet to a triangle in logarithmic $(\ln k_t, -\ln(\Delta R))$ coordinates. The phase-space associated with the hard

branch of the jet is represented by the "primary Lund plane", and further emissions' phase space is represented by corresponding "Lund leaves". The use of logarithmic $(\ln k_t, -\ln(\Delta R))$ coordinates means that the Lund plane naturally reflects the singularity structure of QCD, graphically capturing its soft and collinear limits.

In this section we focus on the definition of the Lund jet plane construction and return to its theoretical implications and its connection to precision observables in Sec. 2.3.1. We begin by considering a jet, which has already been clustered, for example with the anti-k_t algorithm. To construct this jet's primary Lund plane, we (re-)cluster the jet's constituents using the Cambridge/Aachen algorithm, Sec. 2.2.1.3. Given this new clustering sequence, we work backwards through the Cambridge/Aachen clustering. Starting with the full jet, denoted by j, we iteratively repeat the following steps [33]

1. Undo the last step of the clustering: $j \to j_1 + j_2$, where j_1 is taken to be the harder branch, i.e. $p_{\perp,1} > p_{\perp,2}$.

2. Record the properties of the branching, defining

$$\Delta_{12} \equiv \Delta R_{j_1 j_2}, \quad k_t \equiv p_{\perp,2}\Delta_{12}, \quad z \equiv \frac{p_{\perp,2}}{p_{\perp,1} + p_{\perp,2}}, \quad \psi \equiv \arctan \frac{y_1 - y_2}{\phi_1 - \phi_2} \tag{2.2.4}$$

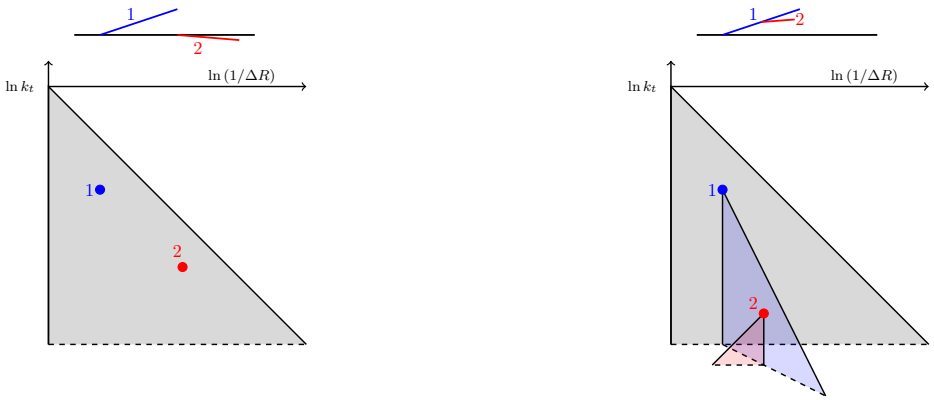
   where $\Delta R_{j_1 j_2}$ was defined in Eq. (2.2.2). Typically this information is organised in terms of a tuple $\mathcal{T} = \{k_t, \Delta_{12}, z, \psi\}$.

3. Redefine $j \leftarrow j_1$ and iterate from step 1.

4. Stop when j can no longer be declustered.

In essence, the above algorithm traverses through the hard branch of an angular-ordered jet, tracking each clustering's properties. Iterating the above procedure for all soft branches defines the full Lund diagram.

In Fig. 2.3 we visualise the Lund jet plane for a simple system of three particles. Fig. 2.3a shows the primary Lund plane resulting from two particles which cluster with the hardest leg in the jet each at its own relative $(\ln k_t, -\ln \Delta R)$. If the particle



(a) Primary Lund plane. **(b)** Full Lund diagram.

Figure 2.3: Simple examples of a primary Lund plane and full Lund diagram for a system of 3 particles. The corresponding particle-level configuration is drawn above each diagram.

denoted by the red circle were to have been closer in angle to the particle denoted by the blue circle, it would not have appeared on the primary plane. In that case, its relative clustering coordinated with respect to the blue particle can be visualised on the full Lund diagram, Fig. 2.3b, which is comprised of the primary Lund plane (grey), and Lund leaves associated with the blue and red particles.

2.3 Resummation

In this section we review the ideas underpinning resummation. The basis of any perturbative calculation is identifying the (typically small) expansion parameter with which we describe our perturbative expansion. So-called "fixed-order" QCD calculations of collider observables, expand them in terms of the QCD strong coupling, Eq. (2.1.7). More concretely, an observable or collider property $P(\alpha_s)$ admits the expansion

$$P(\alpha_s) = P_0 + \alpha_s P_1 + \alpha_s^2 P_2 + \dots , \tag{2.3.1}$$

where P_0 is the leading-order (LO) value of the observables, $\alpha_s P_1$ it's next-to-leading order (NLO) correction and so on. If the coefficients P_n are numerically commensurate, the increasing powers of α_s^n guarantee good convergence of this expansion.

However, in certain contexts, the expansion in Eq. (2.3.1) can be invalidated, particularly when probing configurations close to the Born-level event. To see this, consider an $e^+e^- \to q\bar{q}$ system, where the quark and anti-quark are back-to-back and we cluster the system with the Durham algorithm. At $\mathcal{O}(\alpha_s)$ and in the soft-and-collinear limit, the total cross-section for all emissions to have y, Eq. (2.2.1), below some maximal value y_{cut}, $\Sigma(y < y_{\text{cut}})$, is given by

$$\begin{aligned}\frac{\Sigma(\alpha_s, y < y_{\text{cut}})}{\sigma_0} &\equiv 1 + \frac{1}{\sigma_0}\int \left[\mathrm{d}\sigma^{\text{real}}_{\mathcal{O}(\alpha_s)}\Theta(y < y_{\text{cut}}) + \mathrm{d}\sigma^{\text{virtual}}_{\mathcal{O}(\alpha_s)}\right] \\ &\approx 1 + \frac{\alpha_s C_F}{\pi}\int_0^1 \frac{\mathrm{d}y}{y}\int_{-\frac{1}{2}\ln(1/y)}^{\frac{1}{2}\ln(1/y)} \mathrm{d}\eta\ \Theta(y < y_{\text{cut}}) + (\text{virtual contribution}),\end{aligned} \tag{2.3.2}$$

where σ_0 is the Born-level cross-section, $\mathrm{d}\sigma^{\text{real}}_{\mathcal{O}(\alpha_s)}$ the soft-collinear emission rate extracted from Eq. (2.1.14), $\eta = -\ln(\tan(\theta/2)) \approx -\ln(\theta/2)$ is the pseudo-rapidity in the collinear limit, and the limits on the $\mathrm{d}\eta$ integral come from kinematic constraints. An obvious issue with the real emission contribution to Eq. (2.3.2) is that it is divergent due to the IR divergence as $y \to 0$. However, due to the KLN theorem, Sec. 2.1.3, this IR divergence must cancel against the virtual contribution. Since it needs to compensate only the lower bound of the $\mathrm{d}y$ integral in Eq. (2.3.2), we can write, up to terms proportional to $\alpha_s \ln y_{\text{cut}}$, the virtual contribution to be identical to the real one, modulo a sign difference. Additionally, the $\Theta(y < y_{\text{cut}})$ function is omitted as it is inapplicable to virtual corrections

$$(\text{virtual contribution}) = (-1)\frac{\alpha_s C_F}{\pi}\int_0^1 \frac{\mathrm{d}y}{y}\int_{-\frac{1}{2}\ln(1/y)}^{\frac{1}{2}\ln(1/y)} \mathrm{d}\eta. \tag{2.3.3}$$

Combining Eq. (2.3.2) and Eq. (2.3.3), we get

$$\begin{aligned}\frac{\Sigma(\alpha_s, y < y_{\text{cut}})}{\sigma_0} &= 1 - \frac{\alpha_s C_F}{\pi}\int_0^1 \frac{\mathrm{d}y}{y}\int_{-\frac{1}{2}\ln(1/y)}^{\frac{1}{2}\ln(1/y)} \mathrm{d}\eta\ \Theta(y > y_{\text{cut}}) \\ &= 1 - \frac{\alpha_s C_F}{\pi}\frac{1}{2}\ln^2\left(1/y_{\text{cut}}\right).\end{aligned} \tag{2.3.4}$$

We note that both the soft and the collinear divergence have left their imprint in the form of two $\ln(1/y_{\text{cut}})$ factors. Furthermore, we note that as long as $y_{\text{cut}} \ll 1$, this soft-and-collinear contribution dominates over any other contribution at this order. Iterating the analysis, we would have found that at order α_s^n, the cross

section contains terms proportional to $\alpha_s^n \ln^{2n}(1/y_{\text{cut}})$. A key observation here is that if we were in a regime where $\alpha_s \ln^2(1/y_{\text{cut}}) \sim 1$, then each term in the perturbative expansion for $\Sigma(\alpha_s, y < y_{\text{cut}})$, see Eq. (2.3.1), is commensurate with each other. In other words, it would no longer justifiable to expand $\Sigma(\alpha_s, y < y_{\text{cut}})$ in terms of α_s alone, but rather, one should expand the series in terms of the *logarithmic accuracy* of the observable.

To make the discussion concrete, suppose again then that we calculate some property $P(\alpha_s, L)$ of an event, where α_s is the strong coupling at a scale close to the hard scale, Q, and L is the logarithm of a ratio of scales. There are two ways of classifying logarithmic accuracy.

1. For observables that exponentiate (typically event shapes and some jet rates), one can organise logarithmically enhanced terms as follows [34]:

$$P(\alpha_s, L) = P(\alpha_s, 0) \exp\left(\underbrace{\alpha_s^{-1} g_1(\alpha_s L)}_{\text{LL}} + \underbrace{g_2(\alpha_s L)}_{\text{NLL}} + \underbrace{\alpha_s g_3(\alpha_s L)}_{\text{NNLL}} + \cdots \right) + \mathcal{O}\left(e^{-|L|}\right). \tag{2.3.5}$$

   LL stands for leading-logarithmic accuracy, NLL for next-to-leading logarithmic, and so forth. The N^{k}LL functions, $\alpha_s^{k-1} g_{k+1}(\alpha_s L)$, resum terms $\alpha_s^n L^{n+1-k}$. The LL function, $\alpha_s^{-1} g_1(\alpha_s L)$, starts off with a double logarithmic term $\alpha_s L^2$. Certain observables, such as energy flow into a limited angular region, start only from the g_2 function, (in much of the literature, the g_2 function is then called LL; for consistency across the full set of observables, here we still call it NLL). We note that the final term in Eq. (2.3.5) reflects the fact that the expansion is correct only up to power corrections.

2. For other observables, for example average subjet multiplicities, $\langle N(\alpha_s; L) \rangle$, which we will be extensively considering throughout this thesis, there is no simple exponentiation of double logarithmic (DL) terms. One may instead write

$$\langle N(\alpha_s; L) \rangle = \left[\underbrace{h_1(\alpha_s L^2)}_{\text{DL}} + \underbrace{\sqrt{\alpha_s} h_2(\alpha_s L^2)}_{\text{NDL}} + \underbrace{\alpha_s h_3(\alpha_s L^2)}_{\text{NNDL}} + \ldots \right] + \mathcal{O}\left(e^{-|L|}\right). \tag{2.3.6}$$

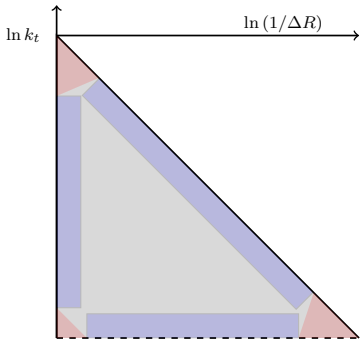


Figure 2.4: Regions of the Lund plane associated with double- (grey), single- (blue) and non- (red) logarithmic log counting.

where the N^{k}DL function, i.e. $\alpha_s^{k/2} h_{k+1}(\alpha_s L^2)$, resums terms $\alpha_s^n L^{2n-k}$. In other work, this classification is often called N^{k}LL (or occasionally N^{k}LL$_\Sigma$). We adopt the N^{k}DL nomenclature in this thesis to avoid confusion with the N^{k}LL of Eq. (2.3.5).

We note that the N^{k}LL and N^{k}DL expansions correspond to slightly different limits. While the N^{k}LL expansion assumes $\alpha_s \ll 1$ and $\alpha_s L \sim 1$, the N^{k}DL expansion works in the limit $\alpha_s \ll 1$ and $\alpha_s L^2 \sim 1$ (implying $\alpha_s L \ll 1$). Since $\alpha_s L \ll 1$ in the N^{k}DL limit, it means that only a finite number of single-logarithmic corrections have to be included in the all-order resummation.

2.3.1 The Lund plane and logarithmic counting

In order to resum observables, one needs to be able to understand the relation between divergences in QCD and the logarithmic counting. The Lund plane, introduced in Sec. 2.2.2, provides an excellent tool for connecting particles' locations in the Lund diagram with associated logarithms of given observables.

Consider, for example, an $\mathcal{O}(\alpha_s)$ process where a single gluon g is emitted off a jet initiator. The primary Lund plane for this process is shown in Fig. 2.4. We first note that depicting the emissions phase space of g in terms of logarithmic coordinates, $(\ln k_t, -\ln \Delta R)$, is very closely connected to the emission probability in both the soft or collinear limits, see Sec. 2.1.3 and Sec. 2.1.4. Second, we note that constraining an observable using g's kinematics is equivalent to putting a phase space cut on the

Lund diagram, see for example Eq. (2.3.4). Indeed, Fig. 2.4 shows the phase space available to all emissions whose $k_t > k_{t,\text{cut}}$, indicated by the dashed lower boundary.

Since the Lund plane shows the logarithmic phase space for emissions, integrating over a two-dimensional, $\mathcal{O}(L) \times \mathcal{O}(L)$, region must, after accounting for both real and virtual emissions, yield two logarithms, i.e. $\alpha_s L^2$. This is possible only in the bulk of the Lund plane (grey in Fig. 2.4), and corresponds to soft and collinear emissions, as seen in our calculation in Sec. 2.3. On the other hand, integrating the emission in a region which is of $\mathcal{O}(1)$ extent in one direction and $\mathcal{O}(L)$ in another (blue regions in Fig. 2.4), leads to only a single-logarithmic contribution, $\alpha_s L$. These configurations come for example from hard-collinear emissions, soft-large-angle emissions, or emissions close to the boundary drawn out by the Θ-function from the observable measurement. Finally, if the integration phase-space in limited to an $\mathcal{O}(1)$ region of the Lund plane (red regions in Fig. 2.4), then this bring a non-logarithmic contribution to the observable, proportional to $\alpha_s \times 1$. This is possible when an emission is, for example, hard and emitted at large angles, hard-and-collinear or soft-large-angle and with a near-boundary value of the observable.

Not only do the above observations provide a valuable tool for understanding the logarithmic structure of observables, they also provide a natural way to systematise ones approach to resumming these observables. In other words, because the list is finite and can be made exhaustive, all possible contributions to a given logarithmic accuracy can easily be enumerated given Lund diagram analyses, as we will see in the following chapters.

3

Parton shower accuracy and colour

In the precision LHC era, a precise theoretical determination of collider observables is paramount. While such predictions can be achieved with dedicated analytic techniques, such as the ones discussed in Sec. 2.3, they are both time-consuming and highly specialised. That is, while the established analytic techniques in the literature can produce high-accuracy predictions for some observables, they are not always easily generalisable to other ones. Thus, the theoretical and experimental communities often instead turn to numerical simulations for collider events with so-called called general-purpose event generators, see Ref. [35] for a recent review. These tools can then be used to yield theoretical predictions for any generic observable of interest.

A particular class of event generators, called parton shower Monte Carlo event generators, simulate the recursive splittings of particles which participated in the hard scattering, evolving them from the hard scale Q to the hadronisation scale, as depicted by the red lines in Fig. 2.2. Going forward we will call QCD parton shower Monte Carlo event generators just 'parton showers' for simplicity. Since parton showers essentially simulate the branching of a few hard partons into jets, they mainly encode soft-and/or-collinear physics. In practice this means that the parton shower probes the logarithmically-divergent matrix elements of QCD. This complements resummation techniques, which, as discussed in Sec. 2.3, often precisely

aim to analytically capture these effect in the form of a resummed logarithm L. Due to this overlap, it has been realised that it is possible to compute numeric resummations of general collider observables with a parton shower. And furthermore, that it is possible to discuss a parton shower's formal accuracy by how well it is able to reproduce known analytic resummation results [36, 37]. This, alongside the fact that differences between parton shower codes are beginning to dominate systematic uncertainties in experimental analyses, for example in the case of the jet energy-scale systematic uncertainty [38, 39], has made parton shower accuracy a key area of research in recent years.

In this chapter we explore in more detail the interplay between parton showers, their accuracy, and resummed observables. We begin by briefly discussing the ideas underpinning parton showers and their accuracy in Sec. 3.1. We then continue by giving an example of evaluating a parton shower's accuracy in Sec. 3.2. It is here that we highlight the work in Ref. [1], which asserted that sub-leading colour contributions are an important consideration when addressing a parton shower's accuracy. Finally, we highlight in Sec. 3.3 that in order to advance parton shower accuracy, we also need a thorough analytical understanding of precision collider observables.

3.1 Overview of parton showers and their accuracy

Today in the literature there is a multitude of parton showers, many of which are still in active development. While these showers are diverse in either implementation, those which are most popular implement a set of common ingredients in order to generate realistic collider events. First, they generate sequential emissions according to a kinematic ordering variable v, which is often proportional to a transverse momentum k_t, or an angle θ. This brings with it both a straightforward implementation of physical properties of QCD, such as angular ordering, see Sec. 2.1.4, as well as benefits for algorithmic implementation. Second, parton showers implement a strategy for generating new emissions and assigning their kinematics. In this regard, the majority of today's most commonly used showers

fall into the dipole family [40], which make use of the idea of approximating QCD as if it had a large number of colours (N_{C}). In this picture, for a given "radiating" dipole, we only need the local dipole kinematics in order to generate a new emission. We return to the topic of the large-N_{C} approximation in Sec. 3.2, but continue to specialise our discussion to dipole parton showers in this chapter due to their abundance. Third, parton showers account for energy conservation through the choice of a recoil scheme. That is, once a new emission is generated, a parton shower takes care of energy conservation either through a local recoil scheme, where the energy conservation is handled locally within the emitting dipole, or a global recoil scheme, where all particles in an event are reweighted to account for energy conservation. Finally, fourth, the emission probability, sometimes called the shower splitting kernel, implements the physical properties of QCD. Typically, the shower splitting kernel is taken in the soft-and/or-collinear limit, making the shower description particularly valid in logarithmically-divergent regions of phase space due to soft-collinear factorisation.

Given the above components, it is not unreasonable to expect that parton showers should consistently generate realistic collider events, correctly modelling soft and collinear regions of phase-space. However, due to the complex interplay between the above components, certain regions of phase space can still be mismodelled. For example, it was shown in Ref. [36] that the properties of common dipole-local recoil schemes in parton showers can spoil the radiation patterns of particles already at $\mathcal{O}\left(\alpha_s^2\right)$, even when particles are strongly ordered in angle. These studies have put into the forefront the question of how to formally define the accuracy of a given parton shower as a cohesive whole.

Parton shower accuracy, as originally defined in Refs. [36, 37], is intimately connected with the concept that a parton shower should be able to reproduce the squared matrix elements and emission probabilities in cases when partons are emitted at disparate scales, e.g. energies or angles, as asserted in Secs. 2.1.3, 2.1.4. That is, a parton shower should offer a good description of QCD when probing regions of phase space dominated by logarithmically-divergent contributions.

Particularly, the work in Refs. [36, 37] established the initial criteria for assessing the logarithmic accuracy of a parton shower

1. One should identify the kinematic configurations for which a shower correctly reproduces tree-level squared matrix elements. For a shower to be LL accurate, it should be able to reproduce the correct tree-level squared matrix element when emissions are widely separated in both relative angle and k_t (or sometimes, energy). In terms of the Lund diagrams discussed in Sec. 2.2.2, this corresponds to a configuration where all emissions are well-separated in both coordinates of the Lund plane. Conversely, at NLL accuracy, a parton shower should be able to reproduce the tree-level squared matrix element in a limit where any number of emissions are well-separated in either k_t or angle, i.e. well-separated in at least one direction of the Lund diagram.

2. One should evaluate the logarithmic accuracy of the shower's predictions for a range of common observables. Particularly, a LL (NLL) accurate parton shower should be able to reproduce the resummation structure of both (a) exponentiating observables as defined in Eq. (2.3.5) up to terms marked LL (NLL), and (b) non-exponentiating observables as defined in Eq. (2.3.6) up to terms marked DL (NDL).

Within this framework it was shown that typical parton showers used in the literature, such as Pythia [41], Sherpa [42], or Herwig [43–45], are at most LL accurate.[1] To amend this, Ref. [37] defined the PanScales family of parton showers, which provided the first implementation of NLL accurate dipole showers withing the above criteria. More concretely, the PanScales showers come in two varieties: the PanLocal family, which implements a dipole-local recoil scheme, and the PanGlobal family, which implements a global recoil scheme. Both families are parametrised

[1] Angular ordering, see Sec. 2.1.4, is a key feature of the Herwig family of showers, which should generate the correct LL terms by construction, as well as NLL terms for global observables (though internal cuts in phase-space can complicate the picture [46]). However, there are certain classes of NLL terms, those associated with non-global logarithms [47], that cannot be accounted for in angular-ordered showers [48], and so angular ordered showers do not at this stage appear to provide the foundations needed for systematic improvements beyond LL across all classes of logarithmically enhanced terms.

by a parameter $0 \leq \beta < 1$, which determines a shower's ordering variable – for example, $\beta = 0$ corresponds to transverse-momentum ordering, and $\beta = 1$ would corresponded to virtuality ordering; see Ref. [37] for full details. A key property of these showers is that they are derived in the large-N_c for e^+e^- collisions. In the following section we consider more closely the effects of sub-leading colour corrections in e^+e^- parton showers. We then describe associated algorithms which extend the NLL accuracy of leading-N_C parton showers to full colour.

3.2 Colour in final-state dipole parton showers

The majority of today's commonly used showers, in particular those of the dipole family, make use of the idea of approximating QCD as if it had a large number of colours (N_C). Within this approximation one can view each event as a collection of independent colour dipoles: each gluon in an event functions as the colour-triplet end of one dipole and the colour anti-triplet end of another, while each (anti-)quark is the colour (anti-)triplet end of a single dipole. Those dipoles then radiate independently (and incoherently) from each other in the spirit of Eq. (2.1.14), where the sum over i, j is taken only over neighbouring particles, and $T_i \cdot T_j = -N_c/2$. This makes it relatively straightforward, at each stage of the showering, to generate a radiation pattern that is correct across small and large angles in the large-N_C limit.

There are several ongoing efforts to include subleading-N_C corrections, see for example Refs. [1] and references therein. However, including subleading colour corrections in full generality is computationally challenging, because as the parton multiplicity increases one should keep track of a rapidly-growing number of possible colour configurations. Here we explore a complementary approach, one which connects the questions of subleading colour and subleading logarithmic contributions. For concreteness, we extend the two criteria defining parton shower accuracy, described the in above section 3.1, to also keep track of the number of colours. Making these explicit, the leading-colour (LC) part of the LL function, LL-LC, involves terms $\alpha_s^n N_\mathrm{C}^n L^{n+1}$, while the next-to-leading colour (NLC) part, LL-NLC,

involves terms $\alpha_s^n N_{\rm C}^{n-2} L^{n+1}$ and so forth. When needed, we will use the abbreviation FC to explicitly denote contributions that include the full colour structure.

Standard dipole showers correctly capture the full set of LL-LC terms (or DL-LC terms, as appropriate for the event property being measured). For exponentiating event properties, such as event shapes, it is natural to consider values of the logarithm around $L \sim 1/\alpha_s$ where NLL terms are of order 1 (cf. Eq. (2.3.5)). Keeping in mind that, numerically, $\alpha_s \sim 1/N_{\rm C}^2 \sim 0.1$, one then concludes that LL-NLC and NLL-LC terms are of comparable importance.[2] For observables that do not exponentiate, one instead considers values of the logarithm around $L \sim 1/\sqrt{\alpha_s}$, and with the same $\alpha_s \sim 1/N_{\rm C}^2$ equivalence, one may take DL-NLC terms to be comparable to NNDL-LC terms. At this point, to consistently control all subleading aspects beyond the LL-LC approximation, it becomes essential to identify approaches to construct showers that are correct not just at NLL-LC, such as the approaches in Refs. [37, 49, 50], but also LL-NLC (such approaches tend also to bring DL-NLC accuracy), explored in Refs. [1, 51].

In this section, we highlight the work in Ref. [1], which presents two novel algorithms for reintroducing colour information into parton showers, and give emphasis to validating and testing their implementation. The underlying observation of the presented approaches is that to achieve NLL-FC accuracy, one does not necessarily need to account for the full colour algebra in its generality. Because the dominant configurations that contribute to, for example, event shapes at NLL accuracy involve configurations of particles commensurate in k_t but well-separated in angle [52], it suffices to correctly capture the properties of colour coherence, Sec. 2.1.4. Specifically, when angles are disparate, one can use colour coherence to identify the colour factor for radiation, either C_F if all emissions at smaller angles form a net colour (anti-)triplet, or C_A if they form a net colour octet.

[2] Strictly, the expansion parameters that should be compared in the large-$N_{\rm C}$ limit are $\alpha_s N_{\rm C}/\pi$, which would be held constant under the operation of taking $N_{\rm C} \to \infty$, and $1/N_{\rm C}^2$. However, for $N_{\rm C} = 3$, the numerical similarity between the two expansion parameters remains.

3.2.1 Segments, NODS, CFFE

To make our discussion concrete, it will be useful to have an illustration of the existing algorithms for assigning colour in parton showers.

In standard dipole showers (e.g. the Pythia 8 shower [53] or the Dire v1 shower [54]), each dipole is split into two elements called the "emitter" and "spectator". Roughly speaking, each element accounts for the rapidity phase-space that extends from zero rapidity in the dipole centre-of-mass frame to the extremity of rapidity phase-space at the emitter end. For gluon emission, each element acquires the full-colour splitting function associated with the flavour of the emitter, i.e. yielding $P_{gq}(z) \equiv P_{qq}(1-z) = 2C_F/z$ ($P_{gg}(z) = C_A/z$) for emission of a soft gluon with momentum fraction $z \ll 1$ if the emitter is a quark (gluon). Accordingly, we refer to this approach as the "colour-factor from emitter" (CFFE) approach. Ref. [36] showed that the CFFE approach yields wrong DL-NLC terms starting from second order, $\alpha_s^2 L^4$, for some observables, e.g. the thrust.

In Ref. [1] we also examined the CFFE approach in PanScales-like showers, where the phase-space is again divided between the two elements of the dipole, at an angle that is roughly equidistant between the emitter and spectator ends of the dipole, in the *event* centre-of-mass frame.[3] Using the approach of Ref. [36], one can show that the method still yields incorrect DL-NLC terms starting from second order, $\alpha_s^2 L^4$, for some observables.

To address these shortcomings, we introduced in Ref. [1] two new schemes based on colour coherence, which provide insight into the colour structure of emissions at widely separated angles - the kinematic configuration which contributes at NLL accuracy. The first of these schemes, nicknamed the Segments scheme, uses an ordered list of transition points in rapidity defined with respect to dipole ends to assign a colour factor for further emissions in accordance with colour coherence.[4] This list is built iteratively from the initial $q\bar{q}$ or gg system. For each dipole

[3] For soft and collinear emissions, this is similar to the colour assignment discussed in Ref. [51].

[4] The scheme bears resemblance to the scheme introduced in Ref. [55] (sec. 4.2), which implemented ideas by Gustafson, Ref. [56], who realised the potential of using Lund diagrams and colour coherence to understand the structure of colour assignment in dipole branchings.

in an event it describes angular regions where emissions should be assigned a $C_A/2 = N_c/2$ or $C_F = (N_c^2 - 1)/2N_c$ colour factor. The positions of these transition points is in accordance with angular ordering, Eq. (2.1.16), which connects colours factors with splitting angles earlier in the showering process. Consequently this scheme captures the full structure of angular ordering for any configuration of emissions widely separated in rapidity.

The second of these schemes utilises a local matrix-element correction factor. More precisely, each dipole in the event keeps track of auxiliary momenta, which are used to compute a local double-soft correction factor in line with Eq. (2.1.14). The resulting multiplicative factor ensures that the correct full-colour emission pattern is reproduced when any number of pairs of emissions are at commensurate rapidities, but disparate energies. Consequently we call this scheme the Nested-Ordered-Double-Soft scheme, or NODS scheme for short. Importantly, the NODS scheme allows us to capture the correct full-colour azimuthal structure of pairs of commensurate-angle energy-ordered emissions. Consequently, both the NODS and the Segments schemes produce identical results with global observables, which are insensitive to azimuthal angles.

For full details on the Segments (NODS) scheme we refer the reader to the original paper [1], section 3.4 (4.3). By design, they both capture the correct coherent colour structure of angular-ordered emissions, i.e. the configuration which contributes at NLL accuracy. Thus, they enable showers to reproduce NLL-FC resummation results for global observables. Sub-leading colour issues still remain in the case of non-global observables.

Below we test the above three algorithms in the context of the parton shower accuracy criteria described in Sec. 3.1. First, we test whether the NLL-LC PanScales showers equipped with either the CFFE, Segments, or NODS scheme, correctly describe tree-level matrix elements in limits where all emissions are well-separated in at least one direction of the Lund diagram. Second, we perform an equivalent test for resummed observables, particularly subjet multiplicity.

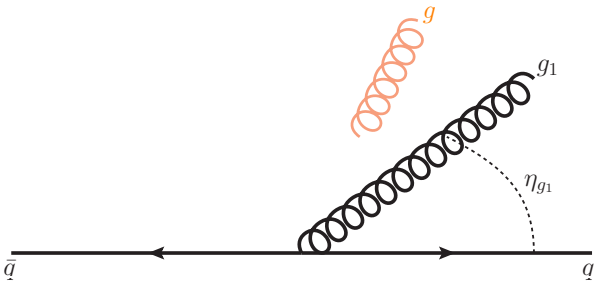


Figure 3.1: Sketch of $e^+e^- \to \bar{q}g_1q$ (black lines) in the $\bar{q}q$ centre-of-mass frame, which coherently emits an additional soft gluon g (orange line) in the $E_q \gg E_{g_1} \gg E_g$ limit.

3.2.2 Matrix element tests

In order to demonstrate how the methods presented above effectively incorporate subleading-colour effects, we examine parton shower results at fixed order for $2 \to 3 + g$ final states, concretely $e^+e^- \to \bar{q}g_1q + g$, where g is an additional soft gluon that is radiated from the $\bar{q}g_1q$ system, Fig. 3.1. We focus on the case where the additional soft gluon g can be at angles commensurate with any other particle (while still strongly ordered in energy compared to them). Below, we compare the parton-shower (PS) result $\mathrm{d}\sigma_{\mathrm{PS}}/\mathrm{d}\eta\mathrm{d}\psi$ (σ_{PS} for brevity) to the exact ratio of full-colour squared matrix elements $\mathrm{d}\sigma_{\mathrm{FC}}/\mathrm{d}\eta\mathrm{d}\psi = \mathrm{d}\Phi_g|M_{\bar{q}g_1q+g}|^2/|M_{\bar{q}g_1q}|^2$ given by Eq. (2.1.14). Here, η and ψ are the rapidity and azimuthal variables as obtained from a Lund declustering procedure (see Eq. (2.2.4)). We do this for each of the CFFE, Segment and NODS parton-shower colour schemes.

All differential plots shown below are produced with the PanGlobal shower, with $\beta = 0$ (see [37] for details). To set up the event ($e^+e^- \to \bar{q}g_1q$, see Figs. 3.1), we let the parton shower split the initial $\bar{q}q$ dipole, which emits a gluon g_1 with predefined kinematics, corresponding in our soft-collinear case to

$$z_{g_1} = 10^{-8}, \quad \eta_{g_1} = 5, \quad \psi_{g_1} = \pi\,, \tag{3.2.1}$$

in the event frame. The emission of the additional gluon, g, is then also performed by the parton shower: we fix the value of the evolution variable $\ln v$ ($\equiv \ln k_t$ for the PanGlobal $\beta = 0$ shower), while sampling over the two remaining shower degrees of freedom. We cluster the event with the Cambridge/Aachen algorithm, Sec. 2.2.1.3,

and work backwards through the clustering history to determine the effective Lund diagram, see Sec. 2.2.2. We call this procedure Lund declustering. We then log the event weight in a histogram in variables (η, ψ) defined with respect to the emission's parent Lund leaf. We fill separate histograms for emission on the primary and secondary Lund leaves. Starting from the same initial $\bar{q}g_1q$ configuration, we also sample the exact full-colour analytic tree-level matrix element, see Eq. (4.4) of Ref. [1], neglecting any recoil from the last emission (since the impact of the emitted soft gluon g is negligible). Finally, we take the ratio of the parton shower and exact full-colour histograms.

The results are collected in Fig. 3.2 for the CFFE, Segment and NODS colour schemes. The labels on each panel, q and g_1, refer to the parton with which the gluon g is clustered by the C/A algorithm (i.e. the emitter according to the Lund declustering sequence). At the top of each column, a diagram indicates the corresponding part of the event that the Lund rapidity η refers to (primary Lund plane, along the quark direction, or secondary plane along the gluon direction). Note that in the following, we do not show differential results at the $\bar{q}$-end since, in this collinear configuration, the emission correctly gets an overall factor of C_F for all colour schemes that we consider (to within corrections suppressed by powers of $e^{-|\eta-\eta_{g_1}|}$). To help see the effective colour factor applied by the parton shower for each method, the upper row in Fig. 3.2 depicts ratios, $\sigma_{\mathrm{PS}}/\sigma_{\mathrm{LC}}$, of the various parton-shower colour schemes to the leading-colour result σ_{LC}. For the latter, we use a constant colour factor $C_F = C_A/2 = 3/2$ irrespective of the position of the emission. The ratio $\sigma_{\mathrm{PS}}/\sigma_{\mathrm{LC}}$ is 1 (yellow in Fig. 3.2) when the effective colour factor is $C_A/2$, while it is $8/9 = 2C_F/C_A$ (green) when the effective colour factor is C_F. In the lower row, we plot the relative deviation $(\sigma_{\mathrm{PS}} - \sigma_{\mathrm{FC}})/\sigma_{\mathrm{FC}}$ between the parton-shower weight and the analytic full-colour matrix element. Regions where the shower agrees with the full-colour matrix element come out in white (to within statistical fluctuations).

The two collinear limits of interest, $g \parallel q$ and $g \parallel g_1$, are always mapped to the large-η region of the corresponding panels, i.e. the q-leaf (left column) and g_1-leaf

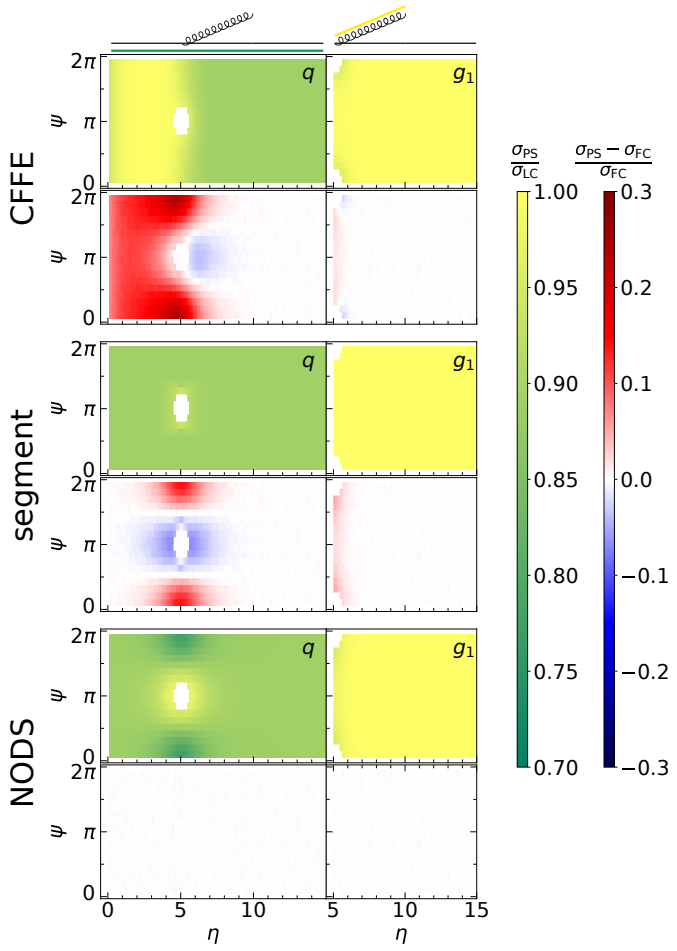


Figure 3.2: Tree-level fixed-order expansion of the parton shower density for emission of a soft gluon from a $\bar{q}g_1q$ system (as represented in Fig. 3.1). The results are shown for the CFFE (top), Segment (middle) and NODS (bottom) colour schemes, as implemented for the PanGlobal shower with $\beta = 0$. The first row in each pair of plots depicts the ratio $\sigma_{\rm PS}/\sigma_{\rm LC}$ (green–yellow colour bar). The second row shows the relative deviation $(\sigma_{\rm PS} - \sigma_{\rm FC})/\sigma_{\rm FC}$ between the parton shower and the analytic matrix element (blue–red colour bar). The left-hand panels corresponds to the primary-emission phase-space region, while the right-hand panels corresponds to emission from g_1, as emphasised in the diagrams at the top.

(right column). Rapidities cover the range $\eta_{\rm p} < \eta < \infty$, where $\eta_{\rm p}$ corresponds to the opening angle between the parent parton and the next particle in the declustering sequence (with $\eta_{\rm p} = 0$ for radiation on the primary plane). Holes correspond to the point where the emission moves across leaves, from a primary to a secondary plane (from the q-leaf to the g_1-leaf, in our example).

Let us examine the three colour methods in turn:

- The CFFE method incorrectly assigns a colour factor $C_A/2$ to the region

$0 < \eta < \eta_{g_1} = 5$. The fact that it extends from zero up to η_{g_1} means that the wrong colour factor is being used for the emission of the soft gluon g in a double-logarithmically enhanced region (for fixed kinematics of the soft gluon g, the double log arises from the integration over the transverse momentum and rapidity of g_1). This ultimately will lead to incorrect subleading N_{C} contributions to LL and DL terms.

- Instead, with the Segments method, colour factors are clearly separated into a C_F region for emissions belonging to the q-leaf, and a $C_A/2$ region for those belonging to the g_1-leaf. A residual deviation from the exact matrix element is present in a region of rapidity localised around η_{g_1}, and reaches the level of $+15\%$ for $\psi = 0$, as shown in the lower row of plots (blue-red colour scale). If one integrates over azimuthal angle and rapidity, the blue and red regions will compensate each other. In section 6.3 of Ref. [1], we verified that that compensation is exact for large η_{g_1}, so that the method reproduces the correct total rate of soft emission needed for NDL-FC accuracy in observables such as multiplicities.

- The NODS procedure reproduces the full squared tree-level matrix element (up to statistical fluctuations associated with our Monte Carlo sampling), as it should, since in this kinematic region the method is effectively using that full tree-level result to correct the leading-colour shower matrix element.

In Ref. [1] similar fixed-order matrix element tests were also performed on more intricate $2 \to 4 + g$ final states such as $e^+e^- \to \bar{q}q\bar{q}'q' + g$ and $e^+e^- \to \bar{q}qgg + g$ with largely similar result. This, alongside the above observations, demonstrates that NLL-LC showers equipped with the Segments or NODS schemes meet the matrix element criteria described in Sec. 3.1 for NLL-FC accuracy, while those equipped with CFFE do not.

3.2.3 Numerical tests for observables: Particle multiplicity

In this section, we investigate the second point underpinning parton shower accuracy, defined in Sec. 3.1. We follow the approach proposed in Ref. [37] for testing the logarithmic structure of showers with specific observables in e^+e^- collisions. Such tests implicitly probe virtual as well as real corrections and so provide a powerful verification of the correct overall assembly of the different shower elements. Generally, as discussed in Secs. 2.3 and 3.1, the tests can be separated into two broad classes, according to whether one is probing a double-logarithmic structure (DL, NDL, etc.) of Eq. (2.3.6), or an exponentiated (LL, NLL, etc.), Eq. (2.3.5), structure.

In this section, we will primarily be concerned with double-logarithmic tests, although single-logarithmic ones were also explored in Ref. [1]. To this end, we specialise the discussion to the average subjet multiplicity observable, defined here as the event-wide multiplicity obtained by running the Durham algorithm, Sec. 2.2.1.1, at a fixed value of y_{cut}. This observable follows a double-logarithmic counting, Eq. (2.3.6). In this case, when analysing the average subjet multiplicity $N(\alpha_s, L)$,[5] we will fix

$$\xi = \alpha_s L^2 \,, \tag{3.2.2}$$

and examine the behaviour of $N(\alpha_s, L)$ in the limit $\alpha_s \to 0$ (with L scaling as $1/\sqrt{\alpha_s}$). Concretely to test $\mathrm{N^kDL}$ accuracy of the parton shower with subjet multiplicity, we will study a quantity such as

$$\delta N_{\mathrm{N^kDL}} = \lim_{\alpha_s \to 0} \left(\frac{N_{\mathrm{PS}}(\alpha_s, \sqrt{\xi/\alpha_s}) - N_{\mathrm{N^kDL}}(\alpha_s, \sqrt{\xi/\alpha_s})}{\alpha_s^{k/2}} \right), \tag{3.2.3}$$

where $N_{\mathrm{N^kDL}}$ is the known $\mathrm{N^kDL}$ prediction from resummation and N_{PS} is the result from the parton shower. For a parton shower that is correct to $\mathrm{N^kDL}$ accuracy, $\delta N_{\mathrm{N^kDL}}$ should be zero. Alternatively, in some tests, we will use a variant of (3.2.3) where the denominator is taken as $N_{\mathrm{N^kDL}} - N_{\mathrm{N^{k-1}DL}}$, except when it vanishes. This has the advantage of providing a meaningful relative deviation at $\mathrm{N^kDL}$ for

[5] For simplicity, we omit the angular brackets in this section, writing $N(\alpha_s, L)$ in place of $\langle N(\alpha_s, L) \rangle$.

situations where $\delta N_{\mathrm{N}^k\mathrm{DL}}$ does not converge to zero as $\alpha_s \to 0$. Values of ξ for different momentum ranges are shown in table 1 of Ref. [1]. In practice we will often use $\xi = \alpha_s L^2 = 5$, which is towards the upper end of the phenomenologically relevant combinations of α_s and L accessible at the LHC. Throughout we will run with the physical colour factors, $N_\mathrm{C} = 3$, $C_F = (N_\mathrm{C}^2 - 1)/(2N_\mathrm{C}) = 4/3$, $C_A = N_\mathrm{C}$ and $n_f = 5$ (except for leading-N_C comparison results, where we use $C_F = \frac{1}{2}C_A = \frac{3}{2}$). The above test is of the most powerful tests of a parton shower, as reproducing the NDL multiplicity requires correct modelling of a variety of aspects of a parton shower, including nested $g \to gg$ and $g \to q\bar{q}$ splittings.

Ref. [37] demonstrated agreement between a range of dipole showers and NDL-LC predictions. We thus examine the remaining question of whether the CFFE, Segments and NODS colour schemes extend these leading-colour results to full colour, yielding the expected NDL-FC results.

To obtain N_PS in Eq. (3.2.3), a parton shower was run as normal, but with the running coupling set to zero below some threshold transverse momentum $k_{t,\mathrm{cut}}$. At NDL accuracy, the particle multiplicity with such a procedure should be identical to the number of subjets clustered with the Durham (see Sec. 2.2.1.1) algorithm [28] with a clustering threshold for the subjets of $y_\mathrm{cut} = k_{t,\mathrm{cut}}^2/Q^2$. Only starting from NNDL do we expect differences to arise between the multiplicity for a shower definition of a k_t cutoff and the k_t algorithm definition.[6] It was explicitly verified in Ref. [1] that this is the case at leading colour.

The analytic expression for the multiplicity in $e^+e^- \to q\bar{q}$ events, $N_{\mathrm{N}^k\mathrm{DL}}$ in Eq. (3.2.3), up to and including NDL terms, can be straightforwardly extracted from Ref. [57],

$$N = 2\frac{C_F}{C_A}\left(1 - \frac{b(2B-1)}{8\pi}\sqrt{\alpha_s\xi}\right)\cosh\left(\sqrt{\frac{2C_A}{\pi}}\xi\right) + 2\left(1 - \frac{C_F}{C_A}\right)\left(1 - \frac{2n_f C_F}{3\pi C_A}\sqrt{\alpha_s\xi}\right) - \sqrt{\frac{\alpha_s}{32\pi C_A}}\frac{2C_F}{C_A}\left[6C_A + \left(\frac{5}{2} - 3B - \frac{C_A\xi}{\pi}\right)b\right]\sinh\left(\sqrt{\frac{2C_A}{\pi}}\xi\right), \tag{3.2.4}$$

[6] As will become apparent in Chap. 4, those differences can for example arise because of details of the specific definition of transverse momentum in the collinear limit, and because of effects related to the jet algorithm's clustering properties.

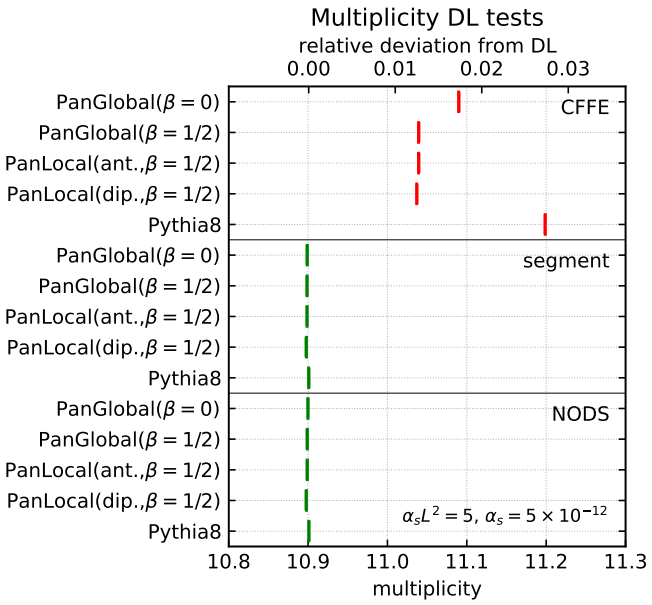
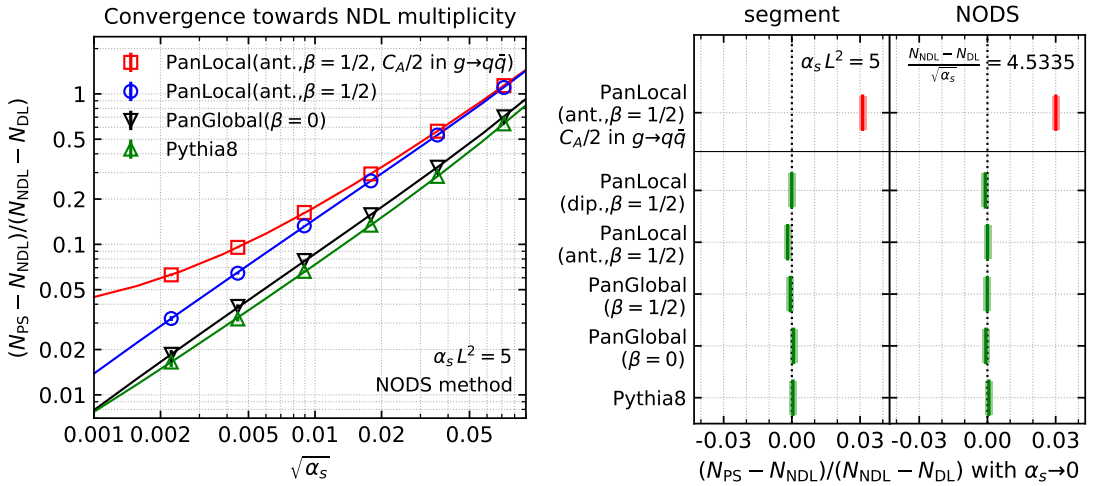


Figure 3.3: DL shower multiplicity tests, showing results for the parton multiplicity at $\xi = \alpha_s L^2 = 5$ in various parton showers and colour schemes, for a sufficiently small value of α_s that NDL terms can be neglected. The DL expectation from Eq. (3.2.4) is $N_{\mathrm{DL}} \simeq 10.9008$.

in the approximation that $L \gg 1$, with $b = \frac{11C_A - 2n_f}{3}$ and $B = 1 + \frac{4n_f(C_A - C_F)}{3bC_A}$. Fig. 3.3 shows the multiplicity N for $\xi = 5$ at a value of $\alpha_s = 5 \times 10^{-12}$, which is sufficiently tiny that one can neglect subleading corrections to within an accuracy of $\sqrt{\alpha_s} \simeq 2.24 \times 10^{-6}$. The figure compares several shower algorithms (the main PanScales showers and the PanScales implementation of the Pythia 8 shower), and three colour schemes, with the analytic DL result. We see that the CFFE scheme, the default in many showers including Pythia 8, differs by up to $\sim 3\%$ from the analytic result. A 3% difference is not a huge effect, but it remains a subleading-N_{C} DL difference and gives a measure of the practical impact of such contributions, i.e. $\sim 1/(3N_{\mathrm{C}}^2)$. For comparison, the differential matrix element plot, Figs. 3.2, showed $\sim 10\%$ differences for the CFFE approach in extended phase-space regions. The Segment and NODS approaches coincide well with the DL analytic multiplicity result for all showers, including when applied to the Pythia 8 shower.

To test the NDL multiplicity terms, we need to examine δN_{NDL}, as defined in Eq. (3.2.3). For this comparison, we need α_s to be large enough for $\sqrt{\alpha_s}$ terms in the multiplicity to be visible after summing over a finite number of Monte



(a) **(b)**

Figure 3.4: NDL shower multiplicity tests. (a) Results for $\frac{N_{\rm PS}-N_{\rm NDL}}{N_{\rm NDL}-N_{\rm DL}}$, for a variety of parton showers in the NODS colour scheme, as a function of $\sqrt{\alpha_s}$, showing that they vanish as $\alpha_s \to 0$, as required to achieve full-colour NDL accuracy. The curves depict a fit that is a polynomial in powers of $\sqrt{\alpha_s}$. (b) Explicit extrapolation of $\frac{N_{\rm PS}-N_{\rm NDL}}{N_{\rm NDL}-N_{\rm DL}}$ to $\alpha_s = 0$, for a range of showers, with the Segment and NODS colour schemes. In both plots we also illustrate the NDL-level discrepancy that arises in a scheme where quarks from $g \to q\bar{q}$ splittings erroneously continue to emit with a $C_A/2$ colour factor.

Carlo events, while also small enough that we can safely extrapolate away $\mathcal{O}(\alpha_s)$ terms. To this end, Fig. 3.4a shows

$$\frac{N_{\rm PS}-N_{\rm NDL}}{N_{\rm NDL}-N_{\rm DL}} = \frac{N_{\rm PS}-N_{\rm DL}}{N_{\rm NDL}-N_{\rm DL}} - 1, \tag{3.2.5}$$

a quantity conceptually similar to $\delta N_{\rm NDL}$ in Eq. (3.2.3) (since $N_{\rm NDL}-N_{\rm DL} \propto \sqrt{\alpha_s}$), as a function of $\sqrt{\alpha_s}$. It shows results for the NODS method for several showers and one sees that most of the results go to zero as $\alpha_s \to 0$, with the exception of the red curve, to which we return below (the Segment method, not shown, gives almost identical results). The result of the actual $\alpha_s \to 0$ extrapolation (using a cubic polynomial extrapolation based on $\alpha_s = \{0.000005, 0.00032, 0.00128, 0.00512\}$) is shown in Fig. 3.4b for each shower and for each of the Segment and NODS methods. All results are consistent with the (full-colour) NDL result, to within the small statistical errors.

Fig. 3.4 also includes results (red points) obtained using a deliberately erroneous prescription that omits the insertion of new C_F Segments following $g \to q\bar{q}$ branchings, resulting in those quarks emitting with a $C_A/2$ colour factor. While

this prescription gives the correct DL-FC result, one should expect it to fail to reproduce the NDL-FC results, because $g \to q\bar{q}$ splittings start to contribute to the multiplicity from NDL terms onwards, as can be verified by inspecting the n_f terms in Eq. (3.2.4).[7] We see in Fig. 3.4a that with this incorrect treatment of $g \to q\bar{q}$ splittings, the limit $\sqrt{\alpha_s} \to 0$ fails to converge to the NDL expectation, validating out approach. Instead the extrapolated NDL coefficient is $\sim 3\%$ larger than the analytic expectation, giving a measure of the impact of subleading N_c corrections to the average multiplicity.

In Ref. [1] we also carried out similar tests for the multiplicity in $e^+e^- \to H \to gg$ events for all showers shown in Fig. 3.4 and found a similar level of agreement with the full-colour NDL predictions for both the Segment and NODS colour prescriptions.

3.3 Parton showers beyond NLL accuracy

QCD parton showers event generators are invaluable tools in both theoretical and experimental particle physics. In the current precision landscape, the topic of parton shower accuracy has come to the forefront of theoretical discussions. In the above sections we established the concept of a parton shower's formal accuracy. In short, a parton shower's accuracy is closely connected to whether it can accurately describe logarithmically-divergent regions of phase space (the soft and collinear limits of QCD) both at fixed order (Sec. 3.2.2), as well as in the case of 'all-orders' resummed observables (Sec. 3.2.3).

A necessary ingredient for testing parton shower accuracy is the availability of all-orders resummations in the literature (indeed, the fixed-order landscape has already been well explored as a consequence of soft and collinear factorisation). To push the frontier of parton shower accuracy beyond the NLL/NDL mark, one would need to tap into, for example, analytical NNDL accurate results for the average subjet multiplicity, similar to what we explored in Sec. 3.2.3. However,

[7] The prescription bears similarities with that of Ref. [55], based on Ref. [56], which concentrated on corrections of the colour factor for primary gluon emissions.

up until the publication of Ref. [1], which led the discussion of this chapter, such results did not exists in the literature.

In the following chapters we compute the average subjet multiplicity up to NNDL accuracy both in e^+e^- collisions (Chap. 4), as well as pp collisions (Chap. 5). These results are relevant both in their own right as stand-alone theoretical predictions for collider observables, worthy of direct theory-to-data comparisons. However, they are also invaluable for testing the next generation of NNLL accurate parton showers, complementing the recent developments on NLL-accurate pp parton showers [58, 59] as well as NNDL developments in e^+e^- parton showers [60].

4

Lund multiplicity in e^+e^- collisions

Motivated by our discussion in Sec. 3.3, we introduce the Lund multiplicity algorithm both within e^+e^- as well as pp collisions, and provide its resummation up to NNDL accuracy. Phenomenologically, multiplicities are amongst the most fundamental observables studied in collider physics and are valuable as they probe the full branching structure of QCD.

The Lund multiplicity algorithm is based on the Lund diagram jet substructure procedure, Sec. 2.2.2, due to its ability to naturally capture theoretical properties of QCD, see Sec. 2.3.1 and, in contrast to past definitions of subjet multiplicities, due to its flexibility with respect to collision system. We begin our discussion in this chapter by analysing the Lund multiplicity in e^+e^- collisions, including its definition, calculation and phenomenological implications. We only then address the additional pieces needed for a full pp prediction in the following chapter, Chap. 5.

4.1 Lund multiplicity algorithm in e^+e^- collisions

We begin by introducing a novel algorithm for evaluating the multiplicity of jets with a relative k_t above a given $k_{t,\text{cut}}$ in e^+e^- collisions. The algorithm draws from the Lund diagram representation of the phase-space where the emission kinematics is visualised in the $(\ln k_t, \eta)$ plane [32, 33, 61], where η is the rapidity

of the emission. The underlying algorithm is similar to that of Sec. 2.2.2, but applied to the whole event.

The procedure to compute the Lund multiplicity, $N^{(\text{Lund})}$, is the following. The starting point is to cluster the full event with the Cambridge algorithm, see Sec. 2.2.1.2, with resolution parameter $y_{\text{cut}} = 1$ so as to generate a single jet with an angular-ordered clustering sequence. We first undo the last step of the clustering i.e. get the two exclusive Cambridge jets. We work in the centre-of-mass of the collision, where this yields a pair of back-to-back jets, splitting the event in two hemispheres. For each jet, we proceed as follows (still working in the centre-of-mass of the collision)

1. Set $N^{(\text{Lund})} = 1$.

2. Undo the last clustering step to generate two subjets j_1 and j_2, with j_1 the most energetic, i.e. $E_1 > E_2$.

3. Calculate the relative transverse momentum of the splitting as

$$k_t \equiv \min(E_1, E_2) \sin\theta = E_2 \sin\theta \,, \tag{4.1.1}$$

   with θ the opening angle between the pair of subjets.

4. If $k_t \geq k_{t,\text{cut}}$ the splitting contributes to the Lund multiplicity, i.e. $N^{(\text{Lund})}$ is incremented by one, and we go back to step 2 for *each* of the two subjets.

5. Otherwise, if $k_t < k_{t,\text{cut}}$, repeat from step 2 following only the hardest subjet j_1.

The procedure terminates when there is nothing left to decluster. The event-wide Lund multiplicity would then be the sum of the results obtained for each of the two exclusive jets.

Naturally, the Lund multiplicity fluctuates on an event-by-event basis. In this chapter, we compute the average $\langle N^{(\text{Lund})} \rangle$, up to NNDL accuracy.

Relation to other multiplicities. The Lund-based definition of multiplicity shares some similarities with other multiplicities in the literature. Let us first discuss its relation with previous definitions of multiplicity using the Cambridge algorithm [29]. We show in Appendix A.3 that, in the e^+e^- case, the Lund procedure is equivalent to running the standard Cambridge algorithm with $y_{\rm cut} = 1$ and counting the total number of clusterings for which $k_t > k_{t,\rm cut}$, provided that the Lund k_t definition, Eq. (4.1.1), is used in both cases. If one uses instead the Cambridge definition for the relative transverse momentum of a clustering

$$k_t^{(\rm Cam)} = \min(E_i, E_j)\sqrt{2(1-\cos\theta_{ij})}, \tag{4.1.2}$$

and imposes the condition $k_t^{(\rm Cam)} > k_{t,\rm cut}$, one obtains a different average multiplicity. We show in Sec. 4.3 that it starts to differ from the Lund multiplicity at NNDL accuracy and we compute the difference. Furthermore, the *standard* definition of the Cambridge jet multiplicity would instead count the number of jets obtained when running the Cambridge algorithm with $y_{\rm cut} = k_{t,\rm cut}^2/Q^2$, where Q is the collision centre of mass energy. We show in Appendix A.3 (and Sec. 4.3) that, at our targeted NNDL accuracy, this is also equivalent to counting the total number of clusterings in the Cambridge sequence with $y_{\rm cut} = 1$ using the definition (4.1.2) for the relative transverse momentum.

An approach often used in the literature is to define the jet multiplicity using the Durham (k_t) algorithm (as done, for example in Ref. [57], see also Eq. (3.2.4)). At NDL accuracy, one gets the same multiplicity whether one uses the Cambridge or Durham algorithm. However, the two definitions start to differ at NNDL. We argue in Appendix A.1 that the use of the Cambridge algorithm considerably simplifies the NNDL calculation, while reaching NNDL accuracy with the k_t algorithm would require semi-numerical ingredients.

Finally, we show in Appendix A.2 that using a different recombination scheme, such as the winner-takes-all [62], would only bring differences beyond our targeted NNDL accuracy.

4.2 Revisiting DL and NDL results

In this section, we derive the average Lund and Cambridge multiplicities at double (DL) and next-to-double (NDL) logarithmic accuracy. These agree with the NDL result of Ref. [57] based on the Durham algorithm, Eq. (3.2.4), although they would start to differ at NNDL accuracy.

For the all-order NDL resummation, we will introduce a new formalism compared to what was initially used in Refs. [29, 57, 63]. This new formalism is considerably simpler and can almost straightforwardly be extended to NNDL accuracy as we will show in Sec. 4.3. The DL resummation is presented in Sec. 4.2.1, with the NDL resummation following in Sec. 4.2.2.

4.2.1 Double-logarithmic (DL) accuracy

To gain insight into the resummation structure of double logarithms, we start by discussing the first orders in the strong coupling. For simplicity, we calculate the multiplicity in one of the two hemispheres, $\langle N_i^{(\text{Lund})}\rangle \equiv \langle N^{(\text{Lund})}\rangle/2$, with $i = q, g$, which depends only on the flavour of the hard partons produced in the underlying Born-level process (at least at the accuracy we are interested in here). We denote by $h^{(i)}_{1,2,3}$ the corresponding DL, NDL and NNDL functions that appear in Eq. (2.3.6) (for a single hemisphere).

We consider two hard processes at Born-level: (i) a back-to-back $q\bar{q}$ pair produced by the decay of a Z boson and (ii) the equivalent situation but for gluons arising from a Higgs boson, i.e. $e^+e^- \to H \to gg$. In this way, we compute the multiplicity for both quark and gluon jets. The centre-of-mass energy of the e^+e^- system is denoted by Q.

Initially, at order α_s^0 we have a single parton in each hemisphere and thus $\langle N_i^{(\text{Lund})}\rangle = 1$. At $\mathcal{O}(\alpha_s)$, we can either have a real emission or a 1-loop virtual correction. We thus write

$$\langle N_i^{(\text{Lund})}\rangle_{\mathcal{O}(\alpha_s)} = \frac{1}{\sigma_0+\sigma_1}\left\{\sigma_0 + \int \mathrm{d}\Phi\, |\mathcal{M}_R|^2\, [1+\Theta(k_t > k_{t,\text{cut}})] + \int \mathrm{d}\Phi\, |\mathcal{M}_V|^2\, [1]\right\}, \tag{4.2.1}$$

where σ_0 is the Born-level cross-section, σ_1 the $\mathcal{O}(\alpha_s)$ correction to the inclusive cross-section, $|\mathcal{M}_{R(V)}|^2$ is the real (virtual) matrix element, and $\mathrm{d}\Phi$ schematically represents the phase-space element for real or virtual emissions. Note that this $\mathcal{O}(\alpha_s)$ expression is completely general so as to facilitate future discussions at higher logarithmic accuracy.

In Eq. (4.2.1), the first term is the Born-level contribution with a single parton in the hemisphere, the second term is the real $\mathcal{O}(\alpha_s)$ correction which, in addition to the hard parton, can receive an additional contribution to the multiplicity if the emitted gluon has a k_t above $k_{t,\mathrm{cut}}$, and the last term is the one-loop virtual correction where there is again a single parton in the hemisphere. The contribution from the hard parton in the real and virtual $\mathcal{O}(\alpha_s)$ terms gives (by definition) the correction σ_1 to the inclusive cross-section, therefore cancelling the overall normalisation. Furthermore, in the contribution from the new emission (proportional to $\Theta(k_t > k_{t,\mathrm{cut}})$) the σ_1 correction in the normalisation can be neglected since it's beyond NDL accuracy,[1] leading to

$$\langle N_i^{(\mathrm{Lund})} \rangle_{\mathcal{O}(\alpha_s)} = 1 + \int \mathrm{d}\Phi \frac{|\mathcal{M}_R|^2}{\sigma_0} \Theta(k_t > k_{t,\mathrm{cut}}). \tag{4.2.2}$$

At DL accuracy, it is sufficient to consider the emission of a soft-and-collinear gluon, in which case the Born-level kinematics factorises from the gluon emission, as discussed in Sec. 2.1.3, and Eq. (4.2.2) becomes

$$\langle N_i^{(\mathrm{Lund})} \rangle_{\mathcal{O}(\alpha_s)} = 1 + \int [\mathrm{d}k] \, |\mathcal{M}(k)|^2 \, \Theta(k_t > k_{t,\mathrm{cut}}), \tag{4.2.3}$$

with $[\mathrm{d}k] \equiv \mathrm{d}^4k \, \delta(k^2)/(2\pi)^3$. In the soft-and-collinear limit, we have

$$k_t \approx \frac{Q}{2} z\theta \approx Qze^{-\eta}, \tag{4.2.4}$$

with z the energy fraction of the emitted gluon, i.e. $E_k = zQ/2$, θ its emission angle, and $\eta = -\ln\tan(\theta/2)$ its rapidity. Furthermore, the matrix element integration

[1] As we will see in Sec. 4.3.2.2, this also holds at NNDL accuracy, where σ_1 can also be neglected.

becomes, see Eq. (2.1.12),

$$\int [\mathrm{d}k]\, |\mathcal{M}(k)|^2\, \Theta(k_t > k_{t,\mathrm{cut}}) = \frac{2\alpha_s C_i}{\pi} \int_0^{\ln(Q/k_{t,\mathrm{cut}})} \mathrm{d}\eta \int_{k_{t,\mathrm{cut}} e^{\eta}/Q}^{1} \frac{\mathrm{d}z}{z} \\ = \frac{2\alpha_s C_i}{\pi} \int_0^{\ln(Q/k_{t,\mathrm{cut}})} \mathrm{d}\eta \int_{k_{t,\mathrm{cut}}}^{Qe^{-\eta}} \frac{\mathrm{d}k_t}{k_t}, \tag{4.2.5}$$

where C_i is the colour factor of the emission. Then, the integration in Eq. (4.2.3) yields

$$\langle N_i^{(\mathrm{Lund})} \rangle_{\mathcal{O}(\alpha_s)} = 1 + \bar{\alpha} \frac{C_i}{C_A} \frac{L^2}{2}, \qquad \text{with} \qquad L = \ln \frac{Q}{k_{t,\mathrm{cut}}}, \quad \bar{\alpha} = \frac{2\alpha_s C_A}{\pi}, \tag{4.2.6}$$

with $C_i = C_F$ for quarks and $C_i = C_A$ for gluons. As expected, we obtain the double-logarithmic enhancement characteristic of soft-and-collinear emissions.

Moving on to $\mathcal{O}(\alpha_s^2)$, we restrict the discussion to the configurations relevant in the double-logarithmic limit. That is, we need to account for two soft-and-collinear emissions each either real or virtual. The $\mathcal{O}(\alpha_s^2)$ contribution to the Lund multiplicity can be written as

$$\begin{aligned} \langle N_i^{(\mathrm{Lund})} \rangle_{\mathcal{O}(\alpha_s^2)} = \left(\frac{2\alpha_s}{\pi}\right)^2 \int_0^\infty \mathrm{d}\eta_1 \int_0^1 \frac{\mathrm{d}z_1}{z_1} \int_0^1 \frac{\mathrm{d}z_2}{z_2} \\ \Big\{ C_i^2 \int_0^\infty \mathrm{d}\eta_{2i} \Big[1\Big] - C_i^2 \int_0^\infty \mathrm{d}\eta_{2i} \Big[1 + \Theta(k_{t,2} > k_{t,\mathrm{cut}})\Big] \\ - C_i^2 \int_0^\infty \mathrm{d}\eta_{2i} \Big[1 + \Theta(k_{t,1} > k_{t,\mathrm{cut}})\Big] \\ - C_i C_A \int_0^\infty \mathrm{d}\eta_{21} \Big[1 + \Theta(k_{t,1} > k_{t,\mathrm{cut}})\Big] \Theta(\eta_{21} > \eta_1) \\ + C_i^2 \int_0^\infty \mathrm{d}\eta_{2i} \Big[1 + \Theta(k_{t,1} > k_{t,\mathrm{cut}}) + \Theta(k_{t,2} > k_{t,\mathrm{cut}})\Big] \\ + C_i C_A \int_0^\infty \mathrm{d}\eta_{21} \Big[1 + \Theta(k_{t,1} > k_{t,\mathrm{cut}}) + \Theta(k_{t,21} > k_{t,\mathrm{cut}})\Big] \Theta(\eta_{21} > \eta_1) \Big\}, \end{aligned} \tag{4.2.7}$$

where the first line includes the virtual-virtual (VV) and virtual-real (VR) cases, the second and third lines correspond to the real-virtual (RV) case and the last two lines contain the real-real case (RR). We have accounted for the fact that the second emission, when being real, can be either a *primary* emission (i.e. a radiation from the leading parton, with a colour factor C_i), or a *secondary* emission (i.e. a radiation from the first gluon, with a colour factor C_A). In writing Eq. (4.2.7), we have defined η_{2j} as the rapidity of emission 2 with respect to its emitter j, i.e. with respect to the parent parton for primary emissions, $\eta_{2i} = -\ln\tan(\theta_{2i}/2)$, and with respect

to the first emitted gluon for secondary emissions, $\eta_{21} = -\ln\tan(\theta_{21}/2)$, as made explicit by the individual integrals. With this in mind, we note the presence of the angular-ordering constrain ($\Theta(\eta_{21} > \eta_1)$) for the (secondary) C_iC_A contribution in both the RR and RV contributions.[2] At DL accuracy where we have strong angular ordering, the relative transverse momentum with respect to the emitter coincides with the transverse momentum measured by the Lund multiplicity algorithm. In the soft-and-collinear limit we therefore have $k_{t,2} \approx E_2\theta_{2i} \approx Qz_2e^{-\eta_{2i}}$ for primary emissions and $k_{t,21} \approx E_2\theta_{21} \approx Qz_2e^{-\eta_{21}}$ for secondary emissions. Finally, while in an exact $\mathcal{O}(\alpha_s^2)$ calculation the multiplicity should be normalised by the $\mathcal{O}(\alpha_s^2)$ inclusive cross-section, at DL accuracy it can safely be normalised by the Born-level condition for reasons equivalent to those discussed above at $\mathcal{O}(\alpha_s)$. Taking these facts into account, we find that the only terms that do not cancel in Eq. (4.2.7) are

$$\langle N_i^{(\text{Lund})}\rangle_{\mathcal{O}(\alpha_s)^2} = \bar{\alpha}^2\frac{C_i}{C_A}\int_0^1\frac{\mathrm{d}z_1}{z_1}\int_0^\infty \mathrm{d}\eta_1\int_0^1\frac{\mathrm{d}z_2}{z_2}\int_{\eta_1}^\infty \mathrm{d}\eta_2\;\Theta(k_{t,21} > k_{t,\text{cut}}), \quad (4.2.8)$$

where we have defined $\eta_2 \equiv \eta_{21}$. The key observation in Eq. (4.2.8) is that all the real contributions cancel against virtual corrections except the contribution from the second gluon emission in the real C_iC_A term, i.e. the secondary gluon radiation. Physically, this comes from the fact that, in an angular-ordered picture, the leading parton carries on radiating independently of whether the first emitted gluon is real or virtual.

At DL accuracy, it is relatively straightforward to show that the above arguments at $\mathcal{O}(\alpha_s^2)$ generalise to all orders. More precisely, at order α_s^n, the only non-zero contribution comes from the kinematic configuration where the n soft gluon emissions are *nested*, i.e. where the second gluon is collinear to the first, the third is collinear to the second, ... , and the n^{th} gluon is collinear to the $(n-1)^{\text{th}}$. This is schematically represented in Fig. 4.1. To write down the all-orders expression, it is useful to introduce for a given emission i its energy fraction with respect to the initial hard parton x_i, i.e. $x_i = 2E_i/Q = \prod_{j\leq i} z_j$ with z_j the energy fraction of each emission with respect to the previous one, and the product running over all previous emissions.

[2]Both these terms share the same soft matrix element (modulo an overall sign). Angular ordering arises after azimuthal averaging, as discussed in Sec. 2.1.4.

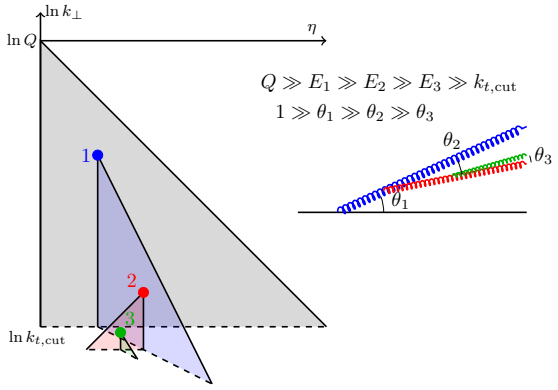


Figure 4.1: Representation of the nested gluon-emission pattern, strongly-ordered in both energies and angles, which constitutes the all-order DL contribution.

We do so since x_i is the strongly ordered variable. We can therefore write the all-orders expression for the Lund multiplicity at DL accuracy as:

$$\begin{aligned}\langle N_i^{(\mathrm{Lund})}\rangle_{\mathrm{DL}} &= 1+\frac{C_i}{C_A}\sum_{n=1}^{\infty}\bar{\alpha}^n\int_0^{\infty}\mathrm{d}\eta_1\int_{\eta_1}^{\infty}\mathrm{d}\eta_2\cdots\int_{\eta_{n-1}}^{\infty}\mathrm{d}\eta_n \\ &\qquad \int_0^1\frac{\mathrm{d}x_1}{x_1}\int_0^{x_1}\frac{\mathrm{d}x_2}{x_2}\cdots\int_0^{x_{n-1}}\frac{\mathrm{d}x_n}{x_n}\Theta(x_n e^{-\eta_n}>e^{-L}) \\ &= 1+\frac{C_i}{C_A}\sum_{n=1}^{\infty}\bar{\alpha}^n\int_0^{L}\mathrm{d}\eta_1\int_{\eta_1}^{L}\mathrm{d}\eta_2\cdots\int_{\eta_{n-1}}^{L}\mathrm{d}\eta_n\frac{(L-\eta_n)^n}{n!} \\ &= 1+\frac{C_i}{C_A}\sum_{n=1}^{\infty}\frac{(\bar{\alpha}L^2)^n}{(2n)!}.\end{aligned} \tag{4.2.9}$$

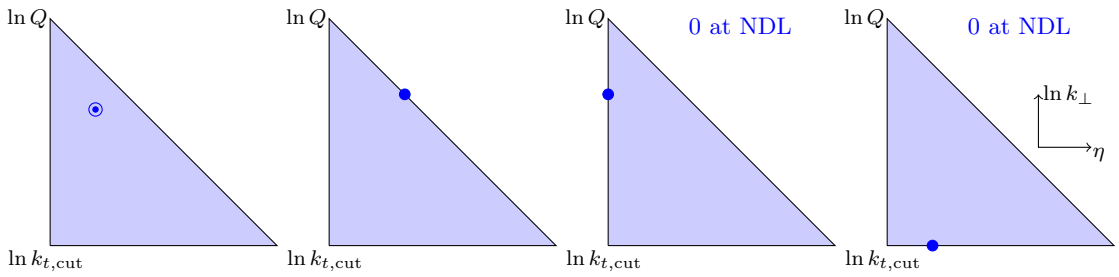
We note that the above calculation can be interpreted geometrically as an integral over the total area of all nested Lund triangles which lie above a given value of $k_{t,\mathrm{cut}}$. The series in Eq. (4.2.9) can easily be summed to get

$$N_i^{(\mathrm{DL})} \equiv \langle N_i^{(\mathrm{Lund})}\rangle_{\mathrm{DL}} = 1+\frac{C_i}{C_A}\left(\cosh\nu-1\right), \tag{4.2.10}$$

where we introduce the following notations which will be helpful throughout this thesis:

$$\nu=\sqrt{\bar{\alpha}L^2}=\sqrt{\frac{2C_A\xi}{\pi}}=\sqrt{\frac{2C_A\alpha_s L^2}{\pi}}. \tag{4.2.11}$$

Eq. (4.2.10) is in agreement with earlier results in the literature [57]. In this soft-and-collinear limit, both hard legs in a $Z\to q\bar{q}$ or $H\to gg$ process are independent of one another. Thus, the average Lund multiplicity is $\langle N_Z^{\mathrm{DL}}\rangle = 2N_q^{(\mathrm{DL})}$ and $\langle N_H^{\mathrm{DL}}\rangle = 2N_g^{(\mathrm{DL})}$, respectively.



(a) Running coupling **(b)** Hard-coll. splitting **(c)** Large or commensurate angle splitting **(d)** $k_{t,\text{emission}} \sim k_{t,\text{cut}}$

Figure 4.2: Lund representation of the configurations that potentially contribute to the multiplicity at NDL. The diagrams are drawn for the primary Lund plane but similar contributions exist for subsidiary planes as well.

$N_i^{(\text{DL})}$ is the total number of Lund declusterings above a fixed $k_{t,\text{cut}}$. In future discussions we also consider the *differential* distribution, i.e. the distribution of Lund declusterings at a given k_t, which can be trivially obtained from the cumulative result:

$$n_i^{(\text{DL})} = \frac{\mathrm{d}N_i^{(\text{DL})}}{\mathrm{d}L} = \frac{C_i}{C_A}\sqrt{\bar{\alpha}}\sinh\nu. \tag{4.2.12}$$

4.2.2 Next-to-double-logarithmic (NDL) accuracy

We now move to the calculation of the NDL h_2 function in Eq. (2.3.6), where $\sqrt{\alpha_s}h_2$ resums terms of order $\alpha_s L(\alpha_s L^2)^n$. This result can be extracted from Ref. [57], but we here propose a more simple and explicit derivation of h_2, thereby introducing a resummation procedure that will be helpful for the NNDL resummation as well.

The central observation is that contributions of the form $\alpha_s L(\alpha_s L^2)^n$ can only be obtained with n soft-collinear emissions, each contributing a factor $\alpha_s L^2$, and a single correction to one of the emissions in the full sequence giving the extra factor $\alpha_s L$. To find the potential configurations that can yield a factor $\alpha_s L$, it is sufficient to go back to the $\mathcal{O}(\alpha_s)$ expression discussed at DL accuracy and list all possible NDL corrections. From Eq. (4.2.3), we see that we can get corrections beyond DL from either the matrix element, or from the expression of the relative transverse momentum k_t. NDL, single-logarithmic, corrections to the matrix element, Eq. (4.2.5), can be of three origins: (i) one-loop running-coupling corrections to α_s, (ii) hard-collinear corrections where one would have to

take into account the full Altarelli–Parisi [64] splitting functions at large z, and (iii) potential soft large-angle corrections away from the collinear limit. These three contributions are schematically represented with the help of Lund diagrams in Figs. 4.2a-4.2c. Finally, potential corrections associated with the $k_t > k_{t,\text{cut}}$ condition are depicted in Fig. 4.2d.

The diagrams in Fig. 4.2b-4.2d clearly exhibit a single-logarithmic behaviour, where the logarithm stems from integrating over a line in the Lund plane, i.e. over a region which extends over a distance of order L in one direction and is limited to an extent of order 1 in the other direction, as discussed in Sec. 2.3.1.

Out of the 4 possibilities sketched in Fig. 4.2, neither the large-angle correction to the matrix element, Fig. 4.2c, nor the emission near the $k_{t,\text{cut}}$ boundary, Fig. 4.2d, contribute at NDL. The case of corrections with $k_t \sim k_{t,\text{cut}}$, Fig. 4.2d, is particularly trivial: single-logarithmic emissions along the $k_{t,\text{cut}}$ boundary are soft and collinear; the DL relations in Eq. (4.2.4) as well as the DL simplification of the matrix-element, Eq. (4.2.5), are therefore still valid, yielding no NDL correction in Eq. (4.2.3).

Let us therefore discuss the case of emissions at large angle. The matrix element times phase space for a soft emission, p_k, off a dipole with legs (p_i, p_j) is given by the eikonal factor, Eq. (2.1.14),

$$\begin{aligned}\int [\mathrm{d}k] |M(k)|^2 &= \frac{\alpha_s}{2\pi}(-2T_i \cdot T_j) \int \frac{\mathrm{d}E_k}{E_k} \frac{\mathrm{d}^2\theta_k}{2\pi}\, E_k^2 \frac{(p_i \cdot p_j)}{(p_i \cdot p_k)(p_j \cdot p_k)} \\ &\equiv \frac{\alpha_s}{2\pi}(-2T_i \cdot T_j) \int \frac{\mathrm{d}E_k}{E_k} \frac{\mathrm{d}^2\theta_k}{2\pi}\, (p_k|p_i p_j),\end{aligned} \tag{4.2.13}$$

with $T_{i,j}$ the colour matrices associated with the dipole legs, and $\mathrm{d}^2\theta_k/2\pi \equiv \mathrm{d}\cos\theta_k\, \mathrm{d}\phi_k/2\pi$. Since the NDL correction can take place anywhere in the chain of DL emissions, we have two cases to consider: either a soft primary emission at large angles, or any subsidiary soft emission which happens at commensurate angle compared to another soft-collinear emission. If the emission is primary, the ij dipole in Eq. (4.2.13) corresponds to the initial $q\bar{q}$ (gg) pair and is, therefore, in a back-to-back configuration. In this case, $-2T_i \cdot T_j = 2C_i$ and one can easily show that Eq. (4.2.13) corresponds exactly to the soft-and-collinear matrix element, Eq. (4.2.5), and, therefore, no new NDL correction arises. Conversely, if we have the

emission of a soft gluon, say k_2, at an angle commensurate to a previous collinear emission, k_1, it follows from our discussion in Sec. 2.1.4 that after integrating after the azimuthal angle of the soft gluon, one recovers the property of angular ordering [9, 65], i.e. $\Theta(\theta_2 < \theta_1) = \Theta(\eta_2 > \eta_1)$. This again reproduces the DL result with no NDL correction. Physically, we can view the absence of large-angle contribution at NDL accuracy as a consequence of the fact that the soft-emission matrix element depends trivially on η both at small and large angles. We note that while the above-made arguments for secondary emissions remain true in a more general collision system, the arguments for the absence of a correction stemming from a first large-angle soft emission required the collision system to be back-to-back. We will thus need to revisit this correction in Chap. 5 when considering the average Lund multiplicity in a pp collider.

In summary, the e^+e^- NDL h_2 function in Eq. (2.3.6) receives only two non-zero contributions:

$$h_2(\nu) = h_{2,\beta_0}(\nu) + h_{2,\mathrm{hc}}(\nu), \tag{4.2.14}$$

that are derived in Eqs. (4.2.19), (4.2.23), (4.2.25) and (4.2.27). The resulting final expression for (4.2.14) agrees with what was originally obtained in Ref. [57].

While these two contributions could be computed in a similar fashion to Eq. (4.2.9), we instead propose a new resummation scheme that relies on the above-mentioned observation that for any set of emissions, only one would be associated with the NDL, yielding a contribution of order $\alpha_s L$, with all other emissions being treated in the DL soft-and-collinear approximation. These soft-collinear emissions can then be resummed using explicitly the DL results in Eqs. (4.2.10) and (4.2.12).

To illustrate this more concretely, we define $\ell \equiv \ln Q/k_t$, where k_t denotes the scale at which the emission takes place. More concretely, a generic NDL correction can stem either from real emissions or from virtual corrections, and can happen either for an emission from the leading parton (i.e. for an emission in the primary Lund plane) or for an emission off a previous DL emission (at any order in α_s).

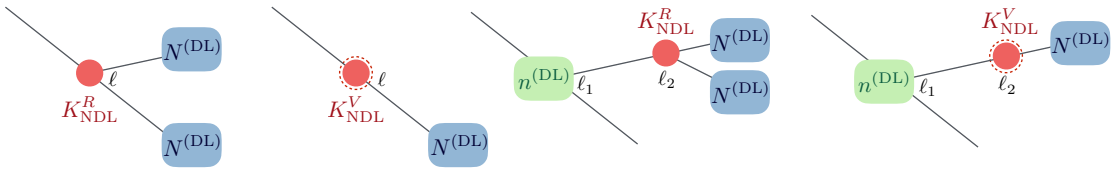


Figure 4.3: Sketch of the method used to compute NDL corrections from two basic ingredients: a single genuine NDL emission, the (red) solid vertex, and towers of DL emissions, either before (green box, Eq. (4.2.12)) or after (blue box, Eq. (4.2.10)) the NDL emission. The four diagrams represent the four options for the NDL vertex: a real emission from the leading parton, a virtual correction from the leading parton, a real emission from any subsidiary DL gluon, or a virtual correction from a subsidiary DL gluon (from left to right).

This leads to a total of four possible contributions that are sketched in Fig. 4.3. More formally, we can write the NDL correction as

$$\delta N_i^{(\rm NDL)} = \int_0^L \mathrm{d}\ell \left\{ K^R_{\rm NDL} \left[N^{(\rm DL)}_{\rm hard}(L;\ell) + N^{(\rm DL)}_{\rm soft}(L;\ell) \right] - K^V_{\rm NDL} N_i^{(\rm DL)}(L;\ell) \right\}$$
$$+ \int_0^L \mathrm{d}\ell_1 n_i^{(\rm DL)}(\ell_1) \int_{\ell_1}^L \mathrm{d}\ell_2 \left\{ K^R_{\rm NDL} \left[N^{(\rm DL)}_{\rm hard}(L;\ell_2) + N^{(\rm DL)}_{\rm soft}(L;\ell_2) \right] - K^V_{\rm NDL} N_g^{(\rm DL)}(L;\ell_2) \right\}, \tag{4.2.15}$$

where the 'hard' and 'soft' indices correspond to the flavours of the harder and softer post-splitting branches respectively. First, we denote by $\delta N_i^{(\rm NDL)} \equiv \sqrt{\alpha_s} h_2^{(i)}$ the NDL corrections to the average Lund plane multiplicity, computed here for a single hemisphere of flavour $i = q, g$. Similarly, $N^{(\rm DL)}(L;\ell)$ denotes the double-logarithmic evolution starting from a parton of transverse momentum scale $e^{-\ell}Q$ down to the cutoff scale $e^{-L}Q$. At this accuracy, $N^{(\rm DL)}(L;\ell) = N^{(\rm DL)}(L-\ell)$. The first line of Eq. (4.2.15) corresponds to the case where the NDL correction occurs in the primary Lund plane, i.e. is associated with an emission off the leading parton as represented in the leftmost two sketches of Fig. 4.3. In this case, the NDL factor $\alpha_s L$ arises after integrating over the k_t of the emission (with $\ell = \ln Q/k_t$). Correspondingly, the second line is associated with NDL corrections for an emission off a subsidiary gluon, displayed in the two rightmost sketches of Fig. 4.3. In this case, we have a tower of DL emissions, yielding a gluon at a relative transverse momentum $k_{t,1}$, with $\ell_1 = \ln(Q/k_{t,1})$. This gluon further splits at a transverse momentum scale $k_{t,2}$, with $\ell_2 = \ln(Q/k_{t,2})$ and the NDL correction, proportional to $\alpha_s L$, stems from the integration over ℓ_2. Also, we have to take into account

that the emission associated with the NDL correction can be either real or virtual. In the former case, both offspring can further emit DL gluons, hence the two contributions $N^{(\mathrm{DL})}_{\mathrm{hard}}(L;\ell_2)$ (emissions from the $k_{t,1}$ gluon at scales smaller than $k_{t,2}$) and $N^{(\mathrm{DL})}_{\mathrm{soft}}(L;\ell_2)$ (emissions off the $k_{t,2}$ gluon, the soft branch), while for the virtual correction, only one parton can further radiate. This DL radiation follows the same pattern of nested radiation as discussed in Sec. 4.2.1, except that it covers scales between $k_{t,2}$ and $e^{-L}Q$ as denoted explicitly by the arguments of $N^{(\mathrm{DL})}_{\mathrm{hard}}(L;\ell_2)$ in Eq. (4.2.15). Finally, the kernels $K^{R,V}_{\mathrm{NDL}}$ denote the genuine NDL corrections, for real and virtual emissions respectively. Since the single-logarithmic contribution has been explicitly written as an integration over ℓ (or ℓ_2), the kernels are proportional to α_s (potentially with extra double-logarithmic factors proportional to $\alpha_s L^2$). The form of Eq. (4.2.15) also implies that the expressions for the NDL kernels, $K^{R,V}_{\mathrm{NDL}}$, can be obtained from the study of a single emission (treated at fixed order) and then inserted in Eq. (4.2.15) to obtain the all-orders result.[3]

In what follows, we use Eq. (4.2.15) to compute the two contributions appearing in Eq. (4.2.14) for one hemisphere.

4.2.2.1 Running coupling effects

We first consider the NDL correction associated to the running of the strong coupling, see Fig. 4.2a. At 1-loop we have, following Sec. 2.1,

$$\alpha_s(k_t) = \frac{\alpha_s}{1-2\alpha_s\beta_0\ln\frac{\mu_R}{k_t}} \approx \alpha_s + 2\alpha_s^2\beta_0\ln\left(\frac{\mu_R}{k_t}\right) + \mathcal{O}\left(\alpha_s^3\right), \tag{4.2.16}$$

where $\alpha_s \equiv \alpha_s(\mu_R)$ with μ_R the renormalisation scale of order Q. Unless explicitly stated otherwise, we assume $\mu_R = Q$. Furthermore $\beta_0 = (11C_A - 4n_f T_R)/(12\pi)$ is the 1-loop β function. At NDL accuracy, one of the emissions in the chain will get a correction $2\alpha_s^2\beta_0\ln(\mu_R/k_t)$, bringing a factor of order $\alpha_s L$ compared to the dominant α_s contribution at DL.

[3] We note that there are no Sudakov factors in Eq. (4.2.15). To understand this, take for example the evolution between ℓ_1 and ℓ_2 in the second line of Eq. (4.2.15). By construction, all the emissions between these two scales can be taken in the DL approximation. At this accuracy, we have already shown in Sec. 4.2.1, that the real emissions between ℓ_1 and ℓ_2 exactly cancel the virtual corrections between these two scales and therefore no Sudakov factors appear in the final expression.

We focus on the contribution from the second line in Eq. (4.2.15) — the rightmost sketches in Fig. 4.3 — noting that the contribution from the first line can straightforwardly be deduced by setting ℓ_1 to zero. Consider therefore that an emission with relative transverse momentum $k_{t,2}$ is radiated off a gluon created itself at a scale $k_{t,1}$, as in Fig. 4.3. This new emission can be emitted over a rapidity range $\ln(k_{t,1}/k_{t,2}) \equiv \ell_2 - \ell_1$ that we can integrate out so as to find

$$K_{\mathrm{NDL},\beta_0} = \frac{2\alpha_s C_A}{\pi} \times (2\alpha_s\beta_0\ell_2) \times (\ell_2 - \ell_1), \tag{4.2.17}$$

valid for both real emissions and virtual corrections.

Since running coupling corrections do not alter the flavour of the leading parton, the real contribution alongside the hard branch and the virtual correction cancel exactly and we are only left with the real contribution from emissions off the soft branch. Using the fact that $n_i^{(\mathrm{DL})} = n_g^{(\mathrm{DL})} C_i/C_A$, we obtain

$$\delta N_{i,\beta_0}^{(\mathrm{NDL})} = \frac{C_i}{C_A} \int_0^L \mathrm{d}\ell_1 \left[\delta(\ell_1) + n_g^{(\mathrm{DL})}(\ell_1)\right] \bar{\alpha} \int_{\ell_1}^L \mathrm{d}\ell_2 (2\alpha_s\beta_0\ell_2)\,(\ell_2 - \ell_1)\, N_g^{(\mathrm{DL})}(L - \ell_2), \tag{4.2.18}$$

where the $\delta(\ell_1)$ term in the square bracket accounts for the correction on the primary Lund plane, as given by the first line of Eq. (4.2.15). Inserting the DL expressions for $N_g^{(\mathrm{DL})}(L - \ell_2)$ and $n_g^{(\mathrm{DL})}(\ell_1)$, Eqs. (4.2.10) and (4.2.12), we can perform the integrations and get

$$h_{2,\beta_0}^{(i)} = \frac{C_i}{C_A}\frac{\beta_0}{2}\sqrt{\frac{\pi}{2C_A}}\left[(\nu^2 - 1)\sinh\nu + \nu\cosh\nu\right]. \tag{4.2.19}$$

4.2.2.2 Hard-collinear correction

In the hard-collinear regime the emission probability given by Eq. (4.2.5) has to be amended in order to incorporate the full DGLAP splitting functions, which can be written as:

$$P_{g\to gg}(z) = 2C_A\left[\frac{1-z}{z} + \frac{z}{2}(1-z)\right], \qquad P_{q\to qg}(z) = 2C_F\left(\frac{1-z}{z} + \frac{z}{2}\right),$$
$$P_{g\to q\bar{q}}(z) = n_f T_R\left[z^2 + (1-z)^2\right], \tag{4.2.20}$$

with n_f the number of flavours and $T_R = 1/2$.[4] In addition to the DL contribution coming from the soft, $z \ll 1$, limit of the splitting function, i.e. $P_{i\to ig} \approx 2C_i/z$, this introduces hard-collinear corrections at finite z. For such a hard-collinear emission happening at a rapidity η, one can simply, at NDL accuracy, integrate the non-divergent part of the splitting function over z, yielding the familiar B coefficients [52]:

$$B_{gg} \equiv \int_0^1 \mathrm{d}z \left[\frac{1}{2C_A} P_{g\to gg}(z) - \frac{1}{z}\right] = -\frac{11}{12}, \quad B_q \equiv \int_0^1 \mathrm{d}z \left[\frac{1}{2C_F} P_{q\to qg}(z) - \frac{1}{z}\right] = -\frac{3}{4},$$
$$B_{gq} \equiv \int_0^1 \mathrm{d}z \, \frac{1}{2C_A} P_{g\to q\bar{q}}(z) = \frac{n_f T_R}{3C_A}, \tag{4.2.21}$$

and identify the k_t scale of the emission, ℓ, with η_2, which is equivalent to neglecting any further dependence on the z fraction in subsequent branchings. The NDL kernel associated with hard-collinear branchings, valid for both real and virtual contributions, is therefore

$$K_{\mathrm{NDL,hc}} = \frac{2\alpha_s C_i}{\pi} \times B, \tag{4.2.22}$$

where C_i and B depend on the flavour channel under consideration.

Below, we consider separately the case of gluon emissions and the case of a flavour-changing $g \to q\bar{q}$ splitting. We thus split the flavour-diagonal (fd) and flavour-changing (fc) contributions and write

$$h_{2,\mathrm{hc}} = h_{2,\text{hc-fd}} + h_{2,\text{hc-fc}}. \tag{4.2.23}$$

Flavour-diagonal Real emissions off the hard branch cancel exactly with the virtual corrections, as in the running coupling calculation, leaving only the contributions from DL radiation off the newly emitted parton $k_{t,2}$ in Eq. (4.2.15). For primary radiation, one gets either a coefficient $B_i = B_q$ or a coefficient $B_i = B_{gg}$ depending on whether the leading jet parton is a quark or a gluon. However, since subsidiary DL emissions are always gluons, their NDL hard-collinear corrections come with a B_{gg} factor. We therefore obtain

$$\delta N^{(\mathrm{NDL})}_{i,\text{hc-fd}} = \frac{C_i}{C_A} \int_0^L \mathrm{d}\ell_1 \left[B_i \delta(\ell_1) + B_{gg} n_g^{(\mathrm{DL})}(\ell_1)\right] \bar{\alpha} \int_{\ell_1}^L \mathrm{d}\ell_2 \, N_g^{(\mathrm{DL})}(L - \ell_2), \tag{4.2.24}$$

[4] Note that we have symmetrised $P_{g\to gg}$ so as to only have a divergence at $z = 0$. This is allowed since both $P_{g\to gg}$ and the observable definitions are symmetric under the $z \to 1 - z$ transformation.

where we have used Eq. (4.2.21) to integrate over the z-coordinate. Performing the remaining integrals yields

$$h^{(i)}_{2,\text{hc-fd}} = \frac{C_i}{C_A}\sqrt{\frac{C_A}{2\pi}}\left[2B_i \sinh\nu + B_{gg}(\nu\cosh\nu - \sinh\nu)\right] . \tag{4.2.25}$$

Flavour-changing The contribution from flavour-changing $g \to q\bar{q}$ splittings involves two modifications with respect to the flavour-diagonal part. First, primary $g \to q\bar{q}$ branchings are only possible for gluon jets. Second, while after a real splitting both resulting subjets are quarks, one still has a gluon after a virtual correction. As a consequence, one no longer has an exact cancellation between the real term $N^{(\text{DL})}_{\text{hard}}$ and the virtual correction which involves $N^{(\text{DL})}_g$, meaning that all the contributions have to be kept. Taking these differences into account, one arrives at the following expression:

$$\begin{aligned}&\delta N^{(\text{NDL})}_{i,\text{hc-fc}} = \\ &\frac{C_i}{C_A}B_{gq}\int_0^L \mathrm{d}\ell_1 \left[\delta_{ig}\delta(\ell_1) + n^{(\text{DL})}_g(\ell_1)\right] \bar{\alpha}\int_{\ell_1}^L \mathrm{d}\ell_2 \left[2N^{(\text{DL})}_q(L-\ell_2) - N^{(\text{DL})}_g(L-\ell_2)\right],\end{aligned} \tag{4.2.26}$$

where δ_{ig} selects gluon-initiated jets. After integration, we get

$$h^{(q)}_{2,\text{hc-fc}} = \frac{C_F}{C_A}\sqrt{\frac{C_A}{2\pi}}B_{gq}\left[c_\delta \nu\cosh\nu + (2-3c_\delta)\sinh\nu + 2(c_\delta - 1)\nu\right] , \tag{4.2.27a}$$

$$h^{(g)}_{2,\text{hc-fc}} = \sqrt{\frac{C_A}{2\pi}}B_{gq}\left[c_\delta \nu\cosh\nu + (2-c_\delta)\sinh\nu\right] , \tag{4.2.27b}$$

for quark and gluon-initiated jets respectively. For the sake of conciseness, we introduced

$$c_\delta \equiv \frac{2C_F - C_A}{C_A}. \tag{4.2.28}$$

4.3 Calculation at NNDL accuracy

4.3.1 Contributions and master formula

We start the NNDL calculation by providing a systematic construction of the physical contributions appearing at NNDL accuracy. Each contribution which is not trivially vanishing will then be discussed in the following subsections. Therefore,

here we lay out the main physics arguments, so as to factor them from the more technical calculations in the following sections.

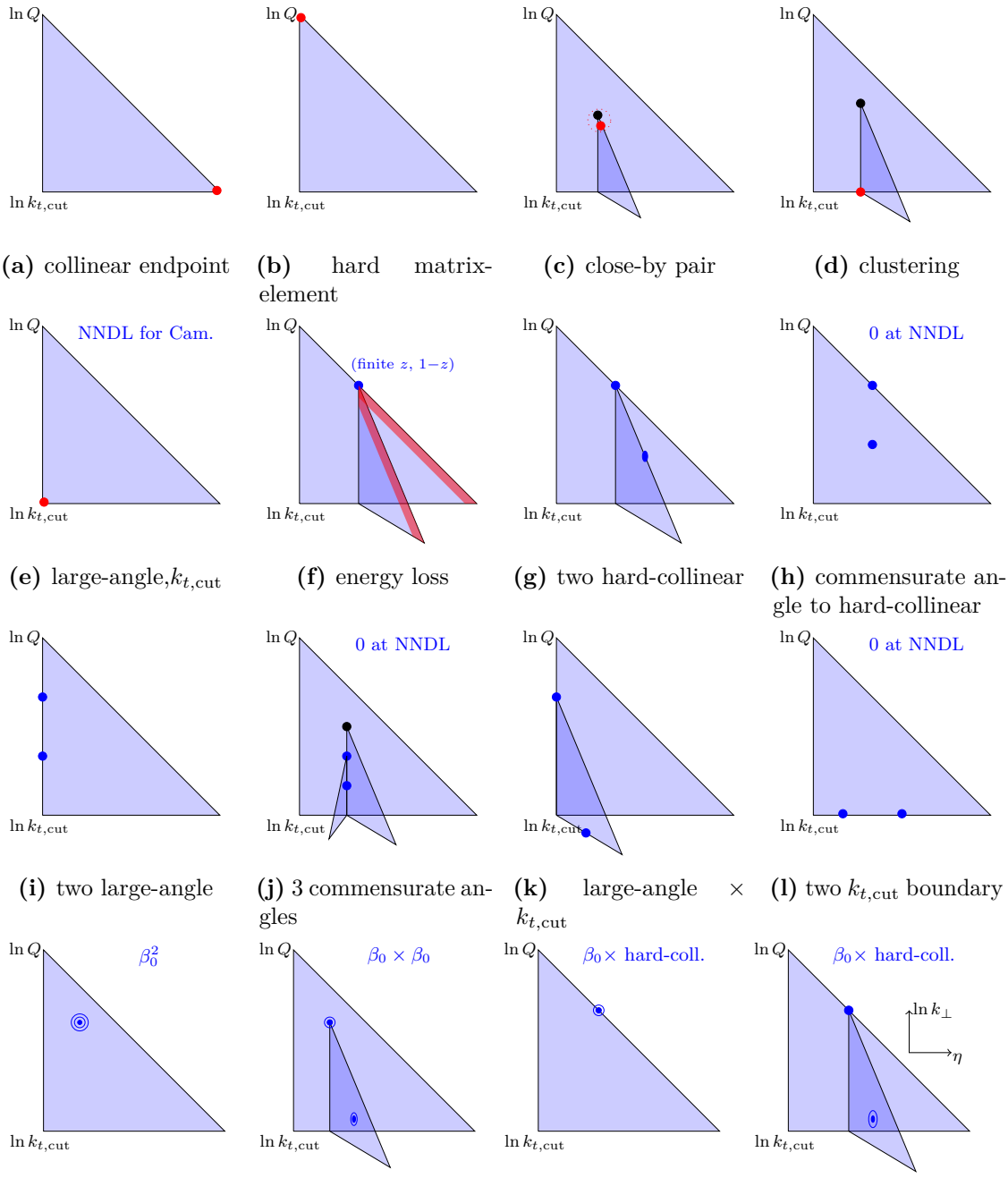
To reach NNDL accuracy, we need to compute the NNDL h_3 function, resumming terms of order $\alpha_s^n L^{2n-2}$, in Eq. (2.3.6). A term of such form can be obtained by either having (A) a single emission contributing a pure factor α_s with no logarithmic enhancement (together with $n-1$ soft-and-collinear emissions contributing as many factors of $\alpha_s L^2$), or (B) two emissions contributing a factor of order $\alpha_s L$ (together with $n-2$ soft-and-collinear emissions). In what follows, we will consider that the logarithms in this counting are of kinematic origin — i.e. arising from integrations over the phase-space of the emissions — and treat as a third category, (C), the contributions involving the running of the strong coupling. In each category, one should take into account contributions from both real and virtual emissions.

We first discuss the category (A), whose contributions are represented in Fig. 4.4a-e. Following the discussion in Sec. 2.3.1, for a contribution to be of $\mathcal{O}(\alpha_s)$ with no logarithmic enhancements, it should be kinematically confined to a region of $\mathcal{O}(1)$ in the Lund plane. This means either in the vicinity of another emission or in one of the three corners of a (primary or subsidiary) Lund plane: (i) at the top of the plane, (ii) at the collinear end of the $k_{t,\text{cut}}$ boundary, or (iii) close to the $k_{t,\text{cut}}$ boundary at an angle commensurate to a previous emission.[5] This directly yields five NNDL-like kinematic configurations compared to what was needed at NDL accuracy. These contributions involve just one emission that is located at:

- The collinear endpoint of the Lund plane (primary or subsidiary), as represented in Fig. 4.4a. This is related to the exact k_t definition and discussed in Sec. 4.3.2.1.

- The top of the primary Lund plane, see Fig. 4.4b. This is associated with fixed-order matrix-element corrections, see Sec. 4.3.2.2.

[5] As for our NDL discussion, we include in 'emissions at commensurate angles' the case of primary emissions at large angles, technically commensurate with the angle π of the initial $q\bar{q}$ (or gg) system.



(a) collinear endpoint **(b)** hard matrix-element **(c)** close-by pair **(d)** clustering

(e) large-angle,$k_{t,\text{cut}}$ **(f)** energy loss **(g)** two hard-collinear **(h)** commensurate angle to hard-collinear

(i) two large-angle **(j)** 3 commensurate angles **(k)** large-angle $\times$ $k_{t,\text{cut}}$ **(l)** two $k_{t,\text{cut}}$ boundary

(m) squared running coupling **(n)** running coupling $\times$ hard-collinear

Figure 4.4: Lund representation of the configurations that contribute to the multiplicity at NNDL. Black dots indicate soft-collinear emissions ($\propto \alpha_s L^2$), blue dots emissions which contribute a factor $\alpha_s L$, and red dots emissions which only contribute a factor α_s with no logarithmic enhancement. Running-coupling corrections ($\propto \alpha_s L$) are represented by open circles.

- The top of a subsidiary Lund plane or in the vicinity of another emission, i.e. associated with a (close-by) pair of emissions at commensurate k_t and

angles. This is shown in Fig. 4.4c and related to the soft limit of the $1 \to 3$ splitting function (or to the collinear limit of the double-soft matrix element) as discussed in Sec. 4.3.2.3.

- Close to the $k_{t,\text{cut}}$ boundary at angles commensurate to a previous emission, see Fig. 4.4d. This is associated with the details of the Cambridge clustering and discussed in Sec. 4.3.2.4.

- At large angles with $k_t \sim k_{t,\text{cut}}$ in the primary Lund plane, see Fig. 4.4e. This correction vanishes for the Lund multiplicity but is non-zero for Cambridge, as discussed in Sec. 4.3.2.5.

We now move on to the kinematic configurations, (B), where two emissions contribute a factor $\alpha_s L$. Following the discussion about NDL multiplicity, for an emission to contribute a factor $\alpha_s L$ it has to be either hard-and-collinear, or at an angle commensurate to a previous emission (including large-angle emissions in the primary Lund plane), or close to the $k_{t,\text{cut}}$ boundary. This results in the following set of configurations, cf. Fig. 4.4g-l, required at NNDL accuracy:

- Two hard-collinear emissions: this includes of course the contribution where two emissions receive NDL-like corrections from the finite splitting function in the hard-collinear limit, as shown in Fig. 4.4g and discussed in Sec. 4.3.3.2. There is however an additional effect to take into account: after a first hard-collinear splitting both daughter partons carry a finite fraction of the energy of the parent parton. This affects the phase-space available for subsequent emissions, shifting the hard-collinear boundary of their Lund planes. This contribution, dubbed *energy loss*, is represented in Fig. 4.4f, where the (red) bands indicate that after the hard-collinear (blue) emission, this phase-space is no longer accessible. The calculation is presented in Sec. 4.3.3.1.

- One hard-collinear emission and one commensurate-angle emission, as shown in Fig. 4.4h. For this, assume we have a set of emissions where one of them, k_1, is a hard-collinear splitting and one of them, k_2, occurs at an angle

commensurate with that of a previous emission. We need to consider two cases depending on whether the commensurate-angle emission happens at an angle commensurate to the hard-collinear one, i.e. $\theta_1 \approx \theta_2$, or to any other soft-collinear emission, i.e. $\theta_1 \ll \theta_2$ or $\theta_1 \gg \theta_2$. We show in Sec. 4.3.3.3 that the first case yields no NNDL corrections. For the second case, it is sufficient to realise that emissions well separated in angle are independent of one another (in particular due to our use of the Cambridge clustering). This would thus result in factorised NDL contributions from k_1 and k_2. This vanishes as well since commensurate-angle emissions have no NDL corrections (see Sec. 4.2.2).

- One hard-collinear emission and one emission close to the $k_{t,\text{cut}}$ boundary (not shown in Fig. 4.4). This vanishes since a hard-collinear emission does not change the k_t of following emissions in the Lund planes of either daughter partons.[6]

- Two emissions at commensurate angles. Here one should distinguish two cases: firstly, the case where the first emission is a primary large-angle emission, Fig. 4.4i and Sec. 4.3.3.4; secondly the case of three emissions at commensurate angles (i.e. a first soft-collinear emission followed by two commensurate-angle soft emissions), Fig. 4.4j, which actually vanishes as explained in Sec. 4.3.3.5.[7]

- One emission at an angle commensurate to that of a previous emission and one emission close to the $k_{t,\text{cut}}$ boundary. For this to have an non-zero effect, one should be in a configuration where the presence of the commensurate-angle emission leads to a difference between the physical transverse momentum (i.e. Sudakov decomposition transverse momentum, see e.g. Ref. [52]) of the second emission and its reconstructed Lund k_t, i.e. configurations where Eq. (4.2.4) has to be revisited. This is only possible when the commensurate-angle

[6] To understand this, consider a hard-and-collinear emission followed by an emission close to the $k_{t,\text{cut}}$ boundary. This soft emission would set the minimum energy in the definition of k_t, Eq. (4.1.1), regardless of whether the previous emission is hard or not.

[7] This does not cover the case where the two commensurate-angle emissions are emitted off different partons, at widely separated angles (i.e. in independent Lund planes). This contribution however vanishes as the contributions from each commensurate-angle emission would factorise into a product of two commensurate-angle NDL contributions which are themselves zero.

emission is a primary emission at large angle, cf. Fig. 4.4k. In practice, this contribution exactly cancels the one from diagram 4.4i and we show this explicitly in Sec. 4.3.3.4.

- Two emissions close to the $k_{t,\text{cut}}$ boundary, Fig. 4.4l. Due to our choice of using the Cambridge algorithm to define the Lund multiplicity, two emissions close to the $k_{t,\text{cut}}$ boundary and well-separated in angles would never cluster with one another: if they belong to the same Lund plane, the most collinear would cluster with the plane's leading parton before the larger-angle does, and two collinear emissions in different Lund planes would cluster with the leading parton of their respective plane. This choice of a Cambridge-based multiplicity definition, and the consequence that the contributions from two commensurate-k_t emissions vanish is crucial for the feasibility of the NNDL calculation. For the more standard definition based on the Durham algorithm [57], this diagram would not only be non-zero at NNDL, but it would also depend in an intricate way on the full angular structure of the event, making it extremely difficult to calculate analytically. We elaborate more on this point in App. A.1.

Finally, we discuss, (C), the contributions associated with the running of the strong coupling constant. Since the 1-loop running contributes at the NDL accuracy, one would naively expect to have two-loop corrections at NNDL. However, if we write the two-loop running coupling at a scale k_t as a function of $\alpha_s \equiv \alpha_s(Q)$ (taking $\mu_R = Q$ without loss of generality), i.e.

$$\alpha_s(k_t) = \frac{\alpha_s}{1 - 2\alpha_s\beta_0 \ln(Q/k_t)} - \frac{\alpha_s^2\beta_1}{\beta_0} \frac{\ln[1 - 2\alpha_s\beta_0 \ln(Q/k_t)]}{[1 - 2\alpha_s\beta_0 \ln(Q/k_t)]^2}, \tag{4.3.1}$$

one sees that the two-loop β_1 correction starts as $\beta_1\alpha_s^3 \ln(Q/k_t)$ which, after integration over the phase-space for emissions with $k_t > k_{t,\text{cut}}$, would bring contributions starting at order $\beta_1\alpha_s^3 \ln^3(Q/k_{t,\text{cut}})$, i.e. only arising from N^{3}DL. This means that the running coupling corrections all come from squared NDL corrections and can be split into:

Contribution	h_3	Diagrams	Section	Result
Collinear endpoint	$h_{3,\text{end}}$	4.4a	4.3.2.1	(4.3.8)
Hard matrix-element	$h_{3,\text{hme}}$	4.4b	4.3.2.2	(4.3.18)
Commensurate k_t and angle	$h_{3,\text{pair}}$	4.4c	4.3.2.3	(4.3.29)
Clustering	$h_{3,\text{clust}}$	4.4d	4.3.2.4	(4.3.36)
Large angle and $k_t \sim k_{t,\text{cut}}$	$h_{3,\text{la}\&k_t}$	4.4e	4.3.2.5	0 (Lund), (4.3.39) (Cam)
Energy loss	$h_{3,\text{eloss}}$	4.4f	4.3.3.1	(4.3.44)
(Hard-collinear)^2	h_{3,hc^2}	4.4g	4.3.3.2	(4.3.49)
Hard-coll. $\times$ comm. angles	—	4.4h	4.3.3.3	0
First emission at large angles	—	4.4i, 4.4k	4.3.3.4	0
3 commensurate angles	—	4.4j	4.3.3.5	0
β_0^2	h_{3,β_0^2}	4.4m	4.3.4.1	(4.3.65)
$\beta_0\times$hard-collinear	$h_{3,\beta_0\times\text{hc}}$	4.4n	4.3.4.2	(4.3.69)
Total	h_3	Fig. 4.4	4.3.5	(4.3.73)-(4.3.79)

Table 4.1: Relevant coefficients for the NNDL function h_3.

- Terms proportional to $[\alpha_s\beta_0 \ln(Q/k_t)]^2$ where the two β_0 factors can either come from a single emission by expanding the first term of Eq. (4.3.1) to second order in β_0, or by having two different emissions, each receiving a β_0 correction. These contributions are depicted in Fig. 4.4m and computed in Sec. 4.3.4.1.

- Terms involving one NDL running coupling correction and one NDL hard-collinear correction. In this case, the running-coupling correction can coincide with the hard-collinear emission or can appear for any other soft-collinear emission, Fig. 4.4n. These are calculated in Sec. 4.3.4.2.

Putting all the non-vanishing contributions together, we get the following expression for the NNDL function h_3:

$$h_3 = h_{3,\text{end}} + h_{3,\text{hme}} + h_{3,\text{pair}} + h_{3,\text{clust}} + h_{3,\text{eloss}} + h_{3,\text{hc}^2} + h_{3,\beta_0^2} + h_{3,\beta_0\times\text{hc}}, \quad (4.3.2)$$

where all the functions depend only on $\xi = \alpha_s L^2$. For Cambridge multiplicity, we instead find

$$h_3^{(\text{Cam})} = h_3^{(\text{Lund})} + h_{3,\text{la}\&k_t} \quad (4.3.3)$$

with $h_3^{(\text{Lund})}$ given by Eq. (4.3.2).

Most of the calculations below are more easily addressed if we consider a single hemisphere, therefore computing the $h_3^{(i)}$ function with $i = q, g$. Although the presence of large-angle contributions, $h_{3,\text{hme}}$ in particular, breaks the independent treatment of the two hemispheres, one is always entitled to write the NNDL correction to the average Lund multiplicity in $Z \to q\bar{q}$ and $H \to gg$ events as $\delta N_Z^{(\text{NNDL})} = \alpha_s h_{3,Z} = 2\alpha_s h_3^{(q)}$ and $\delta N_H^{(\text{NNDL})} = \alpha_s h_{3,H} = 2\alpha_s h_3^{(g)}$.

Tab. 4.1 summarises the physical origin of the various NNDL corrections together with the section discussing them and, when non-zero, the equation where to find the final result. Eq. (4.3.2), together with the individual contributions listed in Tab. 4.1 are the main results of this chapter, which will also prove essential in deriving the results of Chap. 5. For completeness, the full result for $h_3(\nu)$ is summarised in Sec. 4.3.5.

4.3.2 Corrections involving a pure α_s contribution

All the pure α_s contributions involve physical configurations that are new compared to the NDL result. For each of these new kinematic configurations, the α_s-factor arises through a phase-space integration that is only non-exponentially vanishing in a constant region of the Lund plane. This integration typically produces a coefficient $\frac{\alpha_s}{2\pi} D$ with a different constant D for each configuration. This constant can be extracted from a fixed-order calculation before we use it to derive the all-order behaviour by adding an arbitrary number of soft-and-collinear emissions, i.e. following a similar procedure as for the NDL calculation in Sec. 4.2.2, where the NDL kernel in Eq. (4.2.15) and in Fig. 4.3 is now an NNDL kernel.

4.3.2.1 Hard-collinear endpoint

If we consider a parton of flavour i splitting into two collinear daughter partons of flavours b and c, the contribution of the additional parton to the average multiplicity can be written as

$$\langle N_{i\to bc}^{(\text{Lund})} \rangle_{\mathcal{O}(\alpha_s)} = \bar{\alpha} \int_0^\infty \mathrm{d}\eta \int_0^1 \mathrm{d}z \frac{1}{2C_A} P_{i\to bc}(z)\, \Theta\Big(\min\left(z, 1-z\right) e^{-\eta} > e^{-L}\Big), \quad (4.3.4)$$

with $\bar{\alpha} = 2\alpha_s C_A/\pi$, and $P_{i\to bc}(z)$ the DGLAP splitting kernel (see Sec. 4.2.2.2) for the flavour channel under consideration. Say we write $P_{i\to bc}(z) = \frac{2C_i}{z}\,\delta_{cg} + p^{(\text{finite})}_{i\to bc}(z)$, separating explicitly the soft-enhanced and finite contributions. For the contribution proportional to $1/z$, an NNDL correction arises from keeping explicitly the $\min(z, 1-z)e^{-\eta}$ in the k_t constraint instead of approximating it by $ze^{-\eta}$ (which would produce the DL result, with no NDL corrections). Similarly, for the finite piece of the splitting function, $p^{(\text{finite})}_{i\to bc}(z)$, keeping explicitly the $\min(z, 1-z)e^{-\eta}$ in the k_t constraint instead of approximating it by $ze^{-\eta}$ (which would produce the hard-collinear NDL contribution) induces an additional NNDL correction. Both contributions, which come from taking into account the exact expression for the reconstructed k_t of the emission, are relevant in the $\mathcal{O}(1)$ phase-space region where z is finite and the reconstructed k_t is close to the cut $k_{t,\text{cut}}$, cf. Fig. 4.4a.

Considering the two contributions and performing the η integration, one gets an NNDL correction of the form

$$\begin{aligned}\delta N^{(\text{NNDL})}_{i\to bc} &= \bar{\alpha}\int_{1/2}^{1}\frac{\mathrm{d}z}{z}\frac{C_i}{C_A}\delta_{cg}\,\ln\!\left(\frac{1-z}{z}\right) + \bar{\alpha}\int_0^1 \mathrm{d}z\,\frac{p^{(\text{finite})}_{i\to bc}(z)}{2C_A}\,\ln(\min(z,1-z)) \\ &= \frac{\alpha_s}{2\pi}D^{i\to bc}_{\text{end}}. \end{aligned} \tag{4.3.5}$$

Inserting the explicit expressions from Eq. (4.2.20) for the splitting kernels, we get

$$D^{q\to qg}_{\text{end}} = C_F\left(3 + 3\ln 2 - \frac{\pi^2}{3}\right), \tag{4.3.6a}$$

$$D^{g\to gg}_{\text{end}} = C_A\left(\frac{137}{36} + \frac{11}{3}\ln 2 - \frac{\pi^2}{3}\right), \tag{4.3.6b}$$

$$D^{g\to q\bar{q}}_{\text{end}} = n_f T_R\left(-\frac{29}{18} - \frac{4}{3}\ln 2\right). \tag{4.3.6c}$$

We now proceed with the all-order resummation of the collinear endpoint correction. As discussed in Sec. 4.3.1, this is achieved by considering a collinear endpoint emission together with a series of DL soft-and-collinear emissions. Since an emission with $k_t \sim k_{t,\text{cut}}$ has no phase-space to further emit a soft-and-collinear gluon — as is evident from Fig. 4.4a — the collinear endpoint emission should occur as the last step in the series of (nested) DL emissions. We therefore write

$$\alpha_s h^{(i)}_{3,\text{end}} = \frac{\alpha_s}{2\pi}\int_0^L \mathrm{d}\ell\,\left[\delta(\ell)(D^{i\to ig}_{\text{end}} + \delta_{ig}D^{g\to q\bar{q}}_{\text{end}}) + \frac{C_i}{C_A}n^{(\text{DL})}_g(\ell)\left(D^{g\to gg}_{\text{end}} + D^{g\to q\bar{q}}_{\text{end}}\right)\right], \tag{4.3.7}$$

where $n_g^{(\mathrm{DL})}(\ell)$ was defined in Eq. (4.2.12). The first term in this expression, proportional to $\delta(\ell)$, includes corrections from the leading parton, i.e. from the hard-collinear endpoint of the primary Lund plane. The second term includes the contributions from the hard-collinear endpoints of all the secondary gluon emissions. Performing the integrations explicitly, we find

$$h_{3,\mathrm{end}}^{(q)} = \frac{1}{2\pi} D_{\mathrm{end}}^{q\to qg} + \frac{1}{2\pi}\left(D_{\mathrm{end}}^{g\to gg} + D_{\mathrm{end}}^{g\to q\bar{q}}\right)\frac{C_F}{C_A}(\cosh\nu - 1), \tag{4.3.8a}$$

$$h_{3,\mathrm{end}}^{(g)} = \frac{1}{2\pi}\left(D_{\mathrm{end}}^{g\to gg} + D_{\mathrm{end}}^{g\to q\bar{q}}\right)\cosh\nu, \tag{4.3.8b}$$

for quark and gluon jets, respectively.

4.3.2.2 Hard matrix-element corrections (top of the Lund plane)

We next consider the NNDL contribution, $h_{3,\mathrm{hme}}$, stemming from finite corrections to the Born-level matrix element. As shown in Fig. 4.4b, this accounts for the $\mathcal{O}(1)$ region at the top of the primary Lund plane where a first primary splitting is both hard and wide-angle.

Let us first consider the calculation at $\mathcal{O}(\alpha_s)$, for which we go back to the full expression for the Lund plane multiplicity, Eq. (4.2.1). The contribution from the leading parton (the '1' in all three terms) cancels exactly the $\sigma_0 + \sigma_1$, and, for the remaining contribution off the extra emission (the $\Theta(k_t > k_{t,\mathrm{cut}})$ term), σ_1 only contributes at higher orders. As a consequence, Eq. (4.2.2) is still valid. At order α_s we should therefore consider the exact matrix element for $Z \to q\bar{q}g$, and for $H \to ggg$ and $H \to gq\bar{q}$.

An important technical remark is in order. By definition, the exact matrix element represents the emission probability for an emission anywhere in the Lund plane. Therefore, integrating the matrix element with the $k_{t,\mathrm{cut}}$ condition includes three NNDL corrections: (i) the top of the Lund plane, (ii) the collinear endpoint (see Sec. 4.3.2.1) and (iii) the large angle, $k_t \sim k_{t,\mathrm{cut}}$ corner. The latter contribution has been shown to vanish in the previous section. To avoid double counting we thus have to subtract the contribution from the collinear endpoint from the full integration.

The exact matrix elements are best written in terms of the energy fractions $x_i = 2E_i/Q$, with $x_1 + x_2 + x_3 = 2$. For a generic decay of a boson X into three particles of momenta k_i, we therefore write the full-event result as

$$\langle N^{(\text{Lund})}_{X\to k_1k_2k_3}\rangle_{\mathcal{O}(\alpha_s)} = \int \mathrm{d}x_1\mathrm{d}x_2\mathrm{d}x_3\, \frac{|\mathcal{M}^{X\to k_1k_2k_3}|^2}{\sigma_0}\Theta(k_{t,\text{exact}} > k_{t,\text{cut}})\delta(x_1+x_2+x_3-2). \tag{4.3.9}$$

For the different processes we consider, the matrix elements (for the full event, i.e. for both hemispheres) are given by [9, 66]:

$$\frac{|\mathcal{M}^{Z\to q\bar{q}g}|^2}{\sigma_0} = \frac{\alpha_s C_F}{2\pi}\frac{x_1^2+x_2^2}{(1-x_1)(1-x_2)}, \tag{4.3.10}$$

and

$$\frac{|\mathcal{M}^{H\to ggg}|^2}{\sigma_0} = \frac{\alpha_s C_A}{6\pi}\frac{1+(1-x_1)^4+(1-x_2)^4+(1-x_3)^4}{(1-x_1)(1-x_2)(1-x_3)}, \tag{4.3.11a}$$

$$\frac{|\mathcal{M}^{H\to gq\bar{q}}|^2}{\sigma_0} = \frac{\alpha_s n_f T_R}{\pi}\frac{(1-x_2)^2+(1-x_3)^2}{1-x_1}, \tag{4.3.11b}$$

where the last line refers to the case of a $H \to gg$ splitting followed by a $g \to q\bar{q}$ branching, neglecting the situation where the Higgs boson would directly decay into a $q\bar{q}$ pair. The exact k_t in Eq. (4.3.9) depends on which pair of particles gets clustered first by the Cambridge algorithm:

$$\begin{aligned}\Theta(k_{t,\text{exact}} > k_{t,\text{cut}}) = {}& \Theta(\theta_{12}<\theta_{13},\theta_{23})\,\Theta\Big(\min(x_1,x_2)\sin(\theta_{12}) > e^{-L}\Big)\\ &+ \Theta(\theta_{13}<\theta_{12},\theta_{23})\,\Theta\Big(\min(x_1,x_3)\sin(\theta_{13}) > e^{-L}\Big)\\ &+ \Theta(\theta_{23}<\theta_{12},\theta_{13})\,\Theta\Big(\min(x_2,x_3)\sin(\theta_{23}) > e^{-L}\Big).\end{aligned} \tag{4.3.12}$$

Explicit integration of (4.3.9) gives the known DL and NDL contributions, respectively proportional to L^2 and L, negligible terms suppressed by powers of e^{-L} and a constant. This constant is the sum of the collinear endpoints and hard matrix-element NNDL contributions. Subtracting the collinear endpoint computed in Sec. 4.3.2.1, we find[8]

$$\delta N^{(\text{NNDL})}_{X\to k_1k_2k_3} = \frac{\alpha_s}{\pi} D^{k_1k_2k_3}_{\text{hme}} \tag{4.3.13}$$

[8]Note the pre-factor $1/\pi$ instead of $1/(2\pi)$ such that the coefficient D corresponds to the contribution from a single hemisphere, as done for the other NNDL coefficients.

with

$$D^{qqg}_{\text{hme}} = C_F\left(\frac{\pi^2}{6} - \frac{7}{4}\right), \quad D^{ggg}_{\text{hme}} = C_A\left(\frac{\pi^2}{6} - \frac{49}{36}\right), \quad D^{gq\bar{q}}_{\text{hme}} = n_f T_R \frac{2}{9}. \tag{4.3.14}$$

Note that these NNDL hard matrix-element coefficients are independent of the details of the observable. This simply follows from the observation that the hard matrix-element contribution comes from an $\mathcal{O}(1)$ region at the top of the Lund plane while the cut on the observable only affects the soft and/or collinear dynamics. In particular, Eq. (4.3.14) can be cross-checked using other event shapes like the JADE [67], Durham [28], or Cambridge [29] jet multiplicities, as was done in the original publication [2].

Let us now move to the all-order treatment of the hard matrix-element correction. As we have argued above, the virtual corrections, $|\mathcal{M}_V|^2$, and the NLO correction to the inclusive cross-section, σ_1, do not contribute at $\mathcal{O}(\alpha_s)$. This holds at all orders, as we prove in what follows. Since we want to compute the correction arising at the top of the Lund plane, it is sufficient to consider explicitly the emission (real or virtual) with the largest k_t. For this emission, the real and virtual contributions can be of two types: (i) associated with an infrared divergence and, (ii) finite hard matrix-element corrections. Up to a sign, the former are the same for the real and virtual terms and, dressed with additional soft-and-collinear emissions, give rise to the DL and NDL multiplicity. The latter are different for real and virtual terms. For simplicity, let us consider a single hemisphere of flavour a. For a given flavour channel, the real contribution is given by $\sigma_0 \frac{\alpha_s}{2\pi} D^{abc}$ with the D^{abc} coefficient computed above. Let us denote the corresponding virtual contribution by $\sigma_0 \frac{\alpha_s}{2\pi} D_V^{abc}$ where the actual value of D_V^{abc} is irrelevant for the following discussion. Given that these contributions arise from an $\mathcal{O}(1)$ region at the top of the primary Lund plane, they should be dressed by additional DL emissions down to the boundary scale $k_{t,\text{cut}}$. We can therefore write

$$N_a^{(\text{NNDL})}(L) = \tag{4.3.15}$$
$$\frac{\sigma_0}{\sigma_0+\sigma_1}\Big\{N_a^{(\text{NDL})}(L) + \frac{\alpha_s}{2\pi}\sum_{b,c} D^{abc}\Big[N_b^{(\text{DL})}(L) + N_c^{(\text{DL})}(L)\Big] - D_V^{abc} N_a^{(\text{DL})}(L)\Big\},$$

where, for real emissions, both products of the splitting are dressed by DL emissions, while virtual corrections only have a single series of DL emissions. Since (again considering a single hemisphere for simplicity)

$$\sigma_1 = \frac{\alpha_s}{2\pi}\sigma_0 \sum_{b,c} D^{abc} - D_V^{abc}, \tag{4.3.16}$$

Eq. (4.3.15) can be simplified to

$$N_a^{(\mathrm{NNDL})}(L) = N_a^{(\mathrm{NDL})}(L) + \frac{\alpha_s}{2\pi}\sum_{b,c} D^{abc}\Big[N_b^{(\mathrm{DL})}(L) + N_c^{(\mathrm{DL})}(L) - N_a^{(\mathrm{DL})}(L)\Big], \tag{4.3.17}$$

where the virtual contribution D_V^{abc} has disappeared as anticipated. Applying this result to the quark and gluon cases, we get

$$h_{3,\mathrm{hme}}^{(q)} = \frac{1}{2\pi} D_{\mathrm{hme}}^{qqg} \cosh\nu, \tag{4.3.18a}$$

$$h_{3,\mathrm{hme}}^{(g)} = \frac{1}{2\pi}\left[D_{\mathrm{hme}}^{ggg}\cosh\nu + D_{\mathrm{hme}}^{gq\bar{q}}\left(c_\delta \cosh\nu + 1 - c_\delta\right)\right]. \tag{4.3.18b}$$

4.3.2.3 Soft-and-collinear emissions at commensurate angles and k_t

Similarly to the NNDL contribution which appears at the top of the primary Lund plane (Sec. 4.3.2.2), we must also account for similar corrections on subsidiary planes. Concretely, we must account for contributions where a first soft-and-collinear emission is followed by another at commensurate k_t and angle, as is displayed in Fig. 4.4c, alongside its virtual corrections.

To help understanding the structure of this correction we first analyse the $\mathcal{O}(\alpha_s^2)$ contribution to the Lund plane multiplicity. We therefore consider the radiation of two partons, soft and collinear compared to the hard leg. It is helpful to decompose the matrix element for emitting two soft particles with momenta k_1 and k_2 into an uncorrelated, factorised, piece and a correlated piece [52], i.e.

$$\left|\mathcal{M}(k_1,k_2)\right|^2 = \left|\mathcal{M}(k_1)\right|^2\left|\mathcal{M}(k_2)\right|^2 + \left|\widetilde{\mathcal{M}}(k_1,k_2)\right|^2. \tag{4.3.19}$$

The uncorrelated piece does not bring any correction at NNDL since $|\mathcal{M}(k_1)|$ reduces to the soft-and-collinear DL expression in Eq. (4.2.5) and cancels against the virtual-real contribution. The full NNDL correction is therefore in $|\widetilde{\mathcal{M}}(k_1,k_2)|$.

In this case, we can assume that k_1 is emitted first — and is therefore real — and k_2 later (i.e. k_2 is a secondary emission from k_1). Accounting for both cases where k_2 is either virtual or real, the $\mathcal{O}\left(\alpha_s^2\right)$ correction to the Lund multiplicity is given by

$$\begin{aligned}\langle N_{\text{corr}}^{(\text{Lund})}\rangle_{\mathcal{O}(\alpha_s^2)} = &-\frac{1}{\sigma_0}\int[\mathrm{d}k]\left|\widetilde{\mathcal{M}}_{RV}(k)\right|^2\Theta(k_t > k_{t,\text{cut}}) \\ &+\frac{1}{\sigma_0}\int[\mathrm{d}k_1]\int[\mathrm{d}k_2]\left|\widetilde{\mathcal{M}}_{RR}(k_1,k_2)\right|^2\Big[\Theta((k_1+k_2)_t > k_{t,\text{cut}}) + \Theta(k_{t,2} > k_{t,\text{cut}})\Big],\end{aligned} \tag{4.3.20}$$

where $[\mathrm{d}k_i] \equiv \mathrm{d}^4k_i\,\delta(k_i^2)/(2\pi)^3$. The top line of Eq. (4.3.20) corresponds to the correlated piece of the 1-loop virtual correction to single-gluon emission with momentum k and transverse momentum k_t. The Θ-function in the second line of Eq. (4.3.20) makes explicit the behaviour of the Lund multiplicity algorithm, which first encounters a clustering with combined momentum k_1+k_2 and thus Lund transverse momentum $(k_1+k_2)_t$, and subsequently a clustering with momentum k_2 with Lund transverse momentum $k_{t,2}$, measured with respect to k_1. We now make use of a well-known relationship from the literature [52, 68, 69]:

$$\begin{aligned}-\int[\mathrm{d}k]\left|\widetilde{\mathcal{M}}_{RV}(k)\right|^2 + \int[\mathrm{d}k]\int[\mathrm{d}k_1][\mathrm{d}k_2]\left|\widetilde{\mathcal{M}}_{RR}(k_1,k_2)\right|^2\delta^3(k-k_1-k_2)& \\ = \int[\mathrm{d}k]\left|\mathcal{M}(k)\right|^2\alpha_s\left(-2\beta_0\ln\left(k_t/Q\right)+\frac{K}{2\pi}\right),&\end{aligned} \tag{4.3.21}$$

where the δ^3-function is over the two components of the transverse momentum and the rapidity, in analogy to Ref. [52]. In Eq. (4.3.21), K is the CMW factor [68], or equivalently the 1-loop cusp anomalous dimension, given by

$$K = \left(\frac{67}{18}-\frac{\pi^2}{6}\right)C_A - \frac{10}{9}n_fT_R. \tag{4.3.22}$$

Plugging Eq. (4.3.22) into Eq. (4.3.20), we find that only two terms survive – one associated with $|\widetilde{\mathcal{M}}_{RR}|^2\Theta(k_{t,2} > k_{t,\text{cut}})$, i.e. a correction associated with the declustering of k_2, and one associated with $(-2\beta_0\ln\left(k_t/Q\right)+K/2\pi)|\mathcal{M}|^2\Theta(k_t > k_{t,\text{cut}})$, i.e. a correction associated with the declustering of $k \equiv k_1+k_2$. In the latter, we already accounted for the $\mathcal{O}\left(\beta_0\right)$ term as the running-coupling NDL contribution (Sec. 4.2.2.1), while the K term presents a new contribution at NNDL

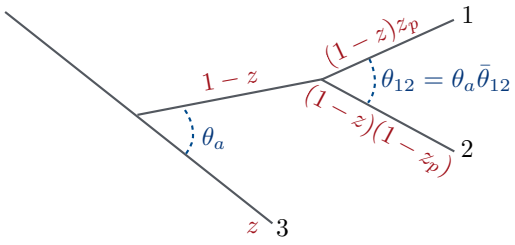


Figure 4.5: Parametrisation of an $i \to 123$ splitting. After a first $i \to 3+a$ splitting a participates in a further $a \to 12$ splitting with characteristic angle θ_{12} and energy fraction z_p. The angle θ_a is that between the parent parton a and the final-state parton 3. Note that the soft limit corresponds to $z \to 1$ while in all previous sections it was parameterised by $z \to 0$.

accuracy. After integrating over the soft-and-collinear emission k with the phase-space given by Eq. (4.2.5) we find

$$\delta N_{i,K}^{(\mathrm{NNDL})} = \left(\frac{C_i}{C_A}\frac{\bar{\alpha}L^2}{2}\right) \times \left(\frac{\alpha_s}{2\pi}K\right), \tag{4.3.23}$$

for a parent parton of flavour i.

We are now left with the computation of the term proportional to $\Theta(k_{t,2} > k_{t,\mathrm{cut}})$ in Eq. (4.3.20). In practice, $|\widetilde{\mathcal{M}}_{RR}|^2$ can be obtained from the soft limit of the $1 \to 3$ splitting function, $\hat{P}_{1\to3}$, or, equivalently, from the collinear limit of the double-soft matrix element [70, 71]. In both cases, one should make sure to remove potential uncorrelated contributions.[9] The resulting expressions are explicitly given in Appendix B of Ref. [2] for all flavour channels. In practice, it is helpful to use the integration variables depicted in Fig. 4.5, where the splitting is viewed as a first soft emission, at an angle θ_a and with a momentum fraction $1-z \ll 1$, followed by a second splitting at an angle θ_{12} with momentum fraction z_p. In the limit where $1-z \ll 1$, one has four flavour channels to consider corresponding to the leading parton, 3, being a quark or a gluon, and to the radiated partons, 1 and 2, being either two gluons or a $q\bar{q}$ pair. In all cases, the remaining part of Eq. (4.3.20), proportional to $\Theta(k_{t,2} > k_{t,\mathrm{cut}})$, then takes the form

$$\int \frac{\mathrm{d}z}{1-z}\frac{\mathrm{d}\theta_a^2}{\theta_a^2}\int \mathrm{d}z_p \frac{\mathrm{d}\bar{\theta}_{12}^2}{\bar{\theta}_{12}^2}\frac{\mathrm{d}\phi_{12}}{2\pi}\frac{z_p(1-z_p)(1-z)^2\bar{\theta}_{12}^2}{\left[1+z_p(1-z_p)\bar{\theta}_{12}^2\right]^2}\left(\frac{\alpha_s}{2\pi}\right)^2 \hat{P}_{1\to3}^{f_1f_2f_3}\Theta(k_{t,21} > k_{t,\mathrm{cut}}). \tag{4.3.24}$$

[9] E.g. for $g \to ggg$ splittings where the triple-collinear splitting function includes an uncorrelated contribution in the C_A^2 colour channel.

for final flavours $f_{1,2,3,}$ and with $k_{t,21} = \frac{Q}{2}(1-z)\min(z_p, 1-z_p)\theta_a\bar{\theta}_{12}$ the relative transverse momentum of k_2 with respect to k_1.[10] From this expression, one can extract the pure NNDL contribution from emissions at commensurate angles and k_t by simply subtracting what is obtained in the strongly-angular-ordered limit:

$$\delta N_{i,RR}^{(\mathrm{NNDL})} = \left(\frac{\alpha_s}{2\pi}\right)^2 \int \frac{\mathrm{d}z}{1-z}\frac{\mathrm{d}\theta_a^2}{\theta_a^2} \int \mathrm{d}z_p \frac{\mathrm{d}\bar{\theta}_{12}^2}{\bar{\theta}_{12}^2}\frac{\mathrm{d}\phi_{12}}{2\pi} \times \left\{ \frac{z_p(1-z_p)(1-z)^2\bar{\theta}_{12}^2}{\left[1+z_p(1-z_p)\bar{\theta}_{12}^2\right]^2} \hat{P}_{1\to 3}^{f_1 f_2 f_3} - \mathcal{P} \right\} \Theta(k_{t,21} > k_{t,\mathrm{cut}}), \tag{4.3.25}$$

where $\mathcal{P}$ is the appropriate combination of DGLAP splitting function contributing at NDL (see Appendix B of Ref. [2] for practical details). Note that since we use the exact expression for $k_{t,21}$, the subtraction also gets rid of the contribution computed in Sec. 4.3.2.1 where k_2 is at the hard-collinear endpoint. Eq. (4.3.25) follows the expected kinematic behaviour: the integrations over z_p and $\bar{\theta}_{12}$ are only non-zero in an $\mathcal{O}(1)$ region of finite z_p and $\bar{\theta}_{12} \sim 1$ ($\theta_{12} \sim \theta_a$), and the integrations over z and θ_a give a double-logarithmic factor. After integration, we get

$$\delta N_{i,RR}^{(\mathrm{NNDL})} = \left(\frac{C_i}{C_A}\frac{\bar{\alpha}L^2}{2}\right) \times \left(\frac{\alpha_s}{2\pi} D_{\mathrm{pair}}^{123}\right), \tag{4.3.26}$$

with

$$D_{\mathrm{pair}}^{q\bar{q}} \equiv D_{\mathrm{pair}}^{g\to q\bar{q}g} = D_{\mathrm{pair}}^{q\to q\bar{q}'q} = \frac{13}{9} n_f T_R, \tag{4.3.27a}$$

$$D_{\mathrm{pair}}^{gg} \equiv D_{\mathrm{pair}}^{g\to ggg} = D_{\mathrm{pair}}^{q\to ggq} = \left(\frac{\pi^2}{6} - \frac{67}{18}\right) C_A. \tag{4.3.27b}$$

Surprisingly, the contribution coming from $i \to ggi$ splittings given by Eq. (4.3.27b) exactly compensates the C_A contribution to the CMW K factor in Eq. (4.3.23). This means that the correction corresponding to Fig. 4.4c will only have an $n_f T_R$ colour factor.

[10] This assumes that the pair (k_1,k_2) of partons clusters first. Strictly speaking, this is only true in the strongly-angular-ordered limit. For commensurate angles, one could have situations where k_1 or k_2 first clusters with the leading parton, in which case $k_{t,21}$ should be replaced by $k_{t,2}$, the relative transverse momentum of k_2 with respect to the leading parton. This difference only matters in the region where $k_{t,2}$ is close to $k_{t,\mathrm{cut}}$ (cf. Fig. 4.4d). This configuration is kinematically different from the one discussed here and is computed in the next section.

To resum these effects to all orders, we follow the usual strategy of considering that the correction can appear at any point in the chain of soft-and -collinear particles. The main subtlety concerns the $i \to q\bar{q}i$ splitting that, as in previous cases, generates a miscancellation between real and virtual contributions. The resummation formula then reads

$$\alpha_s h^{(i)}_{3,\text{pair}} = \frac{C_i}{C_A}\int_0^L \mathrm{d}\ell_1 \left[\delta(\ell_1) + n_g^{(\text{DL})}(\ell_1)\right] \bar{\alpha} \int_{\ell_1}^L \mathrm{d}\ell_2 \int_0^{\ell_2-\ell_1} \mathrm{d}\eta_2 \, \frac{\alpha_s}{2\pi} \times \left[\left(D^{gg}_{\text{pair}} + K\right) N_g^{(\text{DL})}(L-\ell_2) + D^{q\bar{q}}_{\text{pair}} \left(2N_q^{(\text{DL})}(L-\ell_2) - N_g^{(\text{DL})}(L-\ell_2)\right)\right]. \tag{4.3.28}$$

Evaluating the integrals in Eq. (4.3.28), we get

$$h^{(i)}_{3,\text{pair}} = \frac{C_i}{C_A}\frac{1}{2\pi}\left[(1-c_\delta) D^{q\bar{q}}_{\text{pair}} (\cosh\nu - 1) + \left(K + D^{gg}_{\text{pair}} + c_\delta D^{q\bar{q}}_{\text{pair}}\right)\frac{\nu}{2}\sinh\nu\right]. \tag{4.3.29}$$

with c_δ given by Eq. (4.2.28).

4.3.2.4 Clustering corrections

We now discuss the kinematic configuration where we have two emissions (in any Lund plane) at commensurate angles, Fig. 4.4d. More specifically, say we have a 'parent parton', k_0 (either the leading parton or any emission spawning its own Lund plane) in colour representation C_i, accompanied by two extra gluon emissions: a first, k_1, soft-and-collinear in the bulk of the Lund plane, and a second one, k_2, much softer and with a transverse momentum of order $k_{t,\text{cut}}$.

In the angular-ordered limit we have two well-separated contributions: (i) 'primary' radiation, where k_2 is radiated off k_0. This comes with a C_i^2 colour factor, and the transverse momentum of k_2 is measured with respect to k_0, i.e. $k_{t,2} \equiv k_{t,20}$; (ii) 'secondary radiation', where k_2 is radiated off k_1. This comes with a C_iC_A colour factor, and the transverse momentum of k_2 is measured with respect to k_1, i.e. $k_{t,2} \equiv k_{t,21}$. When the emissions have commensurate angles, i.e. when $\theta_{01} \sim \theta_{02} \sim \theta_{12}$, one must take exactly into account the Cambridge clustering used to build the Lund multiplicity. One can therefore be in a situation where a primary emission k_2 is first clustered with k_1, meaning that its relative k_t would actually be $k_{t,21}$ instead of $k_{t,20}$, or in a situation where a secondary emission k_2 is

first clustered with k_0, meaning that its relative k_t would be $k_{t,20}$ instead of $k_{t,21}$. When $k_{t,2}$ is close to $k_{t,\text{cut}}$, finite differences between $k_{t,20}$ and $k_{t,21}$ can put the emission below or above the cut, introducing an NNDL correction compared to what strict angular ordering would give. We call this a *clustering* correction since it is associated with details of the Cambridge clustering.

As usual, we first compute the NNDL correction at fixed order, here $\mathcal{O}(\alpha_s^2)$. The emission of k_1 off k_0, at any angle, can be described using the soft-collinear matrix element in Eq. (4.2.5). Since the second emission is soft and at angles commensurate with θ_{01}, we instead describe it using the eikonal factor given by Eq. (4.2.13). We further can assume, up to NNDL accuracy, that all three angles θ_{01}, θ_{02} and θ_{12} are small and strongly separated from all the other angles in the event. In this case, k_2 can be emitted from any of the three dipoles formed by k_0, k_1 and the recoiling system, k_r,[11] and the sum over dipoles

$$C_A(k_2|k_0k_1) + C_A(k_2|k_1k_r) + (2C_i - C_A)(k_2|k_0k_r), \tag{4.3.30}$$

simplifies considerably. One gets to the following expression for the NNDL clustering correction:

$$\begin{aligned}
&\delta N^{(\text{NNDL})}_{i,\text{clust},\mathcal{O}(\alpha_s^2)} = \\
&\left(\frac{2\alpha_s}{\pi}\right)^2 C_i \int \frac{\mathrm{d}k_{t,1}}{k_{t,1}}\mathrm{d}\eta_1 \int \frac{\mathrm{d}E_2}{E_2}\frac{\mathrm{d}^2\theta_2}{2\pi}\Bigg\{\left[\frac{C_A}{2}\frac{1}{\theta_{12}^2} + \frac{C_A}{2}\frac{\theta_{01}^2}{\theta_{02}^2\theta_{12}^2} + \left(C_i - \frac{C_A}{2}\right)\frac{1}{\theta_{02}^2}\right] \\
&\times \left[\Theta_{\text{clust},0}\Theta(k_{t,20} > k_{t,\text{cut}}) + \Theta_{\text{clust},1}\Theta(k_{t,21} > k_{t,\text{cut}})\right] \\
&- \frac{C_i}{\theta_{02}^2}\Theta(k_{t,20} > k_{t,\text{cut}}) - \frac{C_A}{\theta_{12}^2}\Theta(\theta_{21} < \theta_{01})\Theta(k_{t,21} > k_{t,\text{cut}})\Bigg\},
\end{aligned} \tag{4.3.31}$$

where $\Theta_{\text{clust},i}$ encodes the condition for k_2 to be reconstructed as an emission from k_i:

$$\Theta_{\text{clust},1} \equiv \Theta(\theta_{12} < \theta_{01}, \theta_{02}) \quad \text{and} \quad \Theta_{\text{clust},0} = 1 - \Theta_{\text{clust},1}. \tag{4.3.32}$$

When writing Eq. (4.3.31), the NNDL clustering correction is explicitly written as the difference between the full result including the exact clustering (the first two lines) and the already-computed NDL expression with angular ordering (the last line).

[11] At our accuracy, the recoiling system can be viewed as a unique object as long as it is at much larger angles.

Treating separately the C_i^2 and C_iC_A contributions one sees that the integration over k_2 in Eq. (4.3.31) is finite. The constraints on $k_{t,20}$ or $k_{t,21}$ can be used to perform the integration over E_2 and are non-zero only in a region where $\theta_{02} \sim \theta_{12} \sim \theta_{01}$. We can then do the θ_2 integration, yielding

$$\delta N^{(\mathrm{NNDL})}_{i,\mathrm{clust},\mathcal{O}(\alpha_s^2)} = \left(\frac{2\alpha_s C_i}{\pi}\frac{L^2}{2}\right) \times \left[\frac{\alpha_s}{2\pi}\left(C_i D^{(\mathrm{prim})}_{\mathrm{clust}} + C_A D^{(\mathrm{sec})}_{\mathrm{clust}}\right)\right], \tag{4.3.33}$$

with

$$D^{(\mathrm{prim})}_{\mathrm{clust}} = -\frac{5\pi^2}{54}, \quad \text{and} \quad D^{(\mathrm{sec})}_{\mathrm{clust}} = \frac{\pi^2}{27}. \tag{4.3.34}$$

The generalisation to all orders is relatively straightforward: for each DL gluon emission k_2, emitted from a parent k_1, one should include an NNDL correction of the form of Eq. (4.3.33). One should just properly separate the case where k_2 is a primary emission, i.e. k_1 is the leading parton, for which C_i is given by the flavour of the leading parton, from all subsidiary emissions where $C_i = C_A$. We therefore write

$$\begin{aligned}&\alpha_s h^{(i)}_{3,\,\mathrm{clust}} = \\ &\frac{\alpha_s C_i}{2\pi}\left[\frac{\bar{\alpha}L^2}{2}\left(\frac{C_i}{C_A}D^{(\mathrm{prim})}_{\mathrm{clust}} + D^{(\mathrm{sec})}_{\mathrm{clust}}\right) + \int_0^L \mathrm{d}\ell\left(n_g^{(\mathrm{DL})}(\ell) - \bar{\alpha}\ell\right)\left(D^{(\mathrm{prim})}_{\mathrm{clust}} + D^{(\mathrm{sec})}_{\mathrm{clust}}\right)\right],\end{aligned} \tag{4.3.35}$$

where the first (second) term corresponds to primary (subsidiary) emissions. In particular, one recognises $\int \mathrm{d}\ell(\bar{\alpha}\ell) = \bar{\alpha}L^2/2$ as the multiplicity of primary emissions. Eq. (4.3.35) evaluates to:

$$h^{(i)}_{3,\,\mathrm{clust}} = \frac{C_i}{2\pi}\left\{\left[\cosh\nu - 1 - \left(1 - \frac{C_i}{C_A}\right)\frac{\nu^2}{2}\right] D^{(\mathrm{prim})}_{\mathrm{clust}} + (\cosh\nu - 1) D^{(\mathrm{sec})}_{\mathrm{clust}}\right\}. \tag{4.3.36}$$

4.3.2.5 A primary large-angle emission with $k_t \sim k_{t,\mathrm{cut}}$: the Cambridge multiplicity

The last pure α_s contribution that we consider is that of a first, primary, emission at large angles and with transverse momentum of order $k_{t,\mathrm{cut}}$. The precise definition of k_t plays a central role in this correction and, therefore, differences between the Lund (4.1.1) and Cambridge (4.1.2) k_t definitions are expected.

As already discussed in our NDL calculation, the definition of the Lund-plane transverse momentum k_t, Eq. (4.1.1), coincides exactly with the relative transverse

momentum of the emission with respect to the initial $q\bar{q}$ (or gg) dipole, i.e. the relation in Eq. (4.2.5) is also valid for soft emissions at large angles. Hence, this contribution vanishes for the Lund multiplicity. However, this is not the case for the Cambridge definition of k_t, which is related to the Lund one by

$$k_t^{(\mathrm{Cam})} = k_t^{(\mathrm{Lund})}\sqrt{1+e^{-2\eta}}. \tag{4.3.37}$$

The last factor in Eq. (4.3.37) results in an NNDL correction. At $\mathcal{O}(\alpha_s)$, the contribution of this large-angle, $k_t \sim k_{t,\mathrm{cut}}$ primary emission is, after subtracting the DL contribution:

$$\begin{aligned}\langle N^{(\mathrm{Cam})}_{i,\mathrm{la}\&k_t}\rangle_{\mathcal{O}(\alpha_s)} &= \bar{\alpha}\frac{C_i}{C_A}\int_0^Q \frac{\mathrm{d}k_\perp}{k_\perp}\int_0^\infty \mathrm{d}\eta\ \Theta(k_\perp\sqrt{1+e^{-2\eta}} > Qe^{-L} > k_\perp)\\ &= \frac{\alpha_s}{2\pi}C_i\frac{\pi^2}{12}.\end{aligned} \tag{4.3.38}$$

Noting that, first, a large-angle emission has to be the last clustering in the Cambridge sequence and, second, an emission with $k_t \sim k_{t,\mathrm{cut}}$ leaves no DL phase-space for subsequent emission, this result is valid to all orders. We therefore find that the difference between the Cambridge and Lund multiplicities is (see Appendix A.3 of Ref. [2] for further details)

$$h_3^{(i,\mathrm{Cam})} - h_3^{(i,\mathrm{Lund})} = h_{3,\mathrm{la}\&k_t}^{(i,\mathrm{Cam})} = \frac{C_i}{2\pi}\frac{\pi^2}{12}. \tag{4.3.39}$$

4.3.3 Corrections involving two $\alpha_s L$ factors

4.3.3.1 Energy loss

In Sec. 4.2.2.2 we accounted for the NDL correction corresponding to a single hard-and-collinear splitting. In the NDL case, once a hard-collinear splitting has happened, further emissions from both branches can be treated as if the branch was carrying the same energy as the parent parton. In other words, if $z \sim \mathcal{O}(1)$ is the momentum fraction of the hard-collinear splitting, the factors z and $1-z$ in the daughter branches can be neglected and set to 1. These factors, which we discuss in this section, can however not be neglected at NNDL accuracy. Conceptually, finite z and $1-z$ effects limit the available phase-space for further emissions, as indicated by the red region in Fig. 4.4f. Consequently we name this correction *energy loss*.

The energy loss NNDL contribution can be computed following our generic approach of describing NNDL contributions as subleading corrections dressed by an arbitrary number of double-logarithmic, nested, soft-and-collinear emissions. One therefore starts either with the leading parton or with any (DL) gluon emitted from it via nested soft-collinear radiation at a transverse momentum scale ℓ_1. This parton then undergoes a (real or virtual) hard-collinear splitting at a transverse scale ℓ_2, with a momentum fraction z. For a real splitting, the resulting "hard" and "soft" branches will then radiate DL soft-collinear emissions from (relative) transverse momentum $k_{t,\text{hard}} = (1-z)e^{-\ell_2}$ and $k_{t,\text{soft}} = ze^{-\ell_2}$, respectively, taking into account the exact energy sharing in the hard-collinear branching. One therefore writes, summing over all possible flavour configurations,

$$\begin{aligned}\langle N^{(\text{Lund})}_{i,\text{e-loss}}\rangle = &\sum_{abc}\int_0^L \mathrm{d}\ell_1\Big[\delta_{ai}\delta(\ell_1)+\delta_{ag}n_i^{(\text{DL})}(\ell_1)\Big]\int_{\ell_1}^L \mathrm{d}\ell_2\int \mathrm{d}z\frac{\alpha_s}{\pi}P_{a\to bc}(z) \\ &\Big[N_b^{(\text{DL})}(L-\ell_2+\ln(1-z))+N_c^{(\text{DL})}(L-\ell_2+\ln(z))-N_a^{(\text{DL})}(L-\ell_2)\Big].\end{aligned} \tag{4.3.40}$$

Again, it is convenient to separate the splitting function into a soft-divergent component (for gluon emissions) and a finite piece, i.e. $P_{a\to bc}(z) = \frac{2C_a}{z}\delta_{cg} + p^{(\text{finite})}_{a\to bc}(z)$. In the small-$z$ limit, only the singular part contributes. Combined with the $N_c^{(\text{DL})}(L-\ell_2+\ln(z))$ term in the second line, it gives rise to the DL behaviour. For the remaining terms, the z integral has no logarithmic enhancements. Next, one recognises the NDL contribution coming from the finite part of the splitting function, neglecting the $\ln(1-z)$ and $\ln(z)$ offsets in $N_b^{(\text{DL})}$ and $N_c^{(\text{DL})}$. These offsets however start contributing at NNDL accuracy, either from the soft part of the splitting function together with $N_b^{(\text{DL})}(L-\ell_2+\ln(1-z))$, or from the finite part of the splitting function with both N_b and N_c in the second line. Up to subleading corrections, we can use the expansion:

$$N_b^{(\text{DL})}(L-\ell_2+\ln(1-z)) \simeq N_b^{(\text{DL})}(L-\ell_2) + n_b^{(\text{DL})}(L-\ell_2)\,\ln(1-z), \tag{4.3.41a}$$

$$N_c^{(\text{DL})}(L-\ell_2+\ln(z)) \simeq N_c^{(\text{DL})}(L-\ell_2) + n_c^{(\text{DL})}(L-\ell_2)\,\ln(z), \tag{4.3.41b}$$

with NNDL corrections associated with the right-most terms. The z integration can then be carried out for each flavour yielding ($n_q^{(\mathrm{DL})} = C_F/C_A n_g^{(\mathrm{DL})}$)

$$\langle N_{i,\text{e-loss}}^{(\text{Lund})} \rangle = \frac{C_i}{C_A}\frac{\alpha_s}{2\pi}\int_0^L \mathrm{d}\ell_1 \Big[D^i_{\text{e-loss}}\delta(\ell_1) + D^g_{\text{e-loss}} n_g^{(\mathrm{DL})}(\ell_1)\Big] \int_{\ell_1}^L \mathrm{d}\ell_2\, n_g^{(\mathrm{DL})}(L-\ell_2). \tag{4.3.42}$$

with, the following NNDL coefficients

$$D^q_{\text{e-loss}} = 2\int \mathrm{d}z \Big[P_{q\to qg}(z)\ln(1-z) + \frac{C_A}{C_F} p^{(\text{finite})}_{q\to qg}(z)\ln(z)\Big] = \frac{7}{2}C_A + \left(\frac{5}{2} - \frac{2\pi^2}{3}\right) C_F, \tag{4.3.43a}$$

$$\begin{aligned} D^g_{\text{e-loss}} &= 2\int \mathrm{d}z \Big\{ P_{g\to gg}(z)\ln(1-z) + p^{(\text{finite})}_{g\to gg}(z)\ln(z) \\ &\qquad + \frac{C_F}{C_A} P_{g\to q\bar{q}}(z)[\ln(1-z)+\ln(z)]\Big\} \\ &= \left(\frac{67}{9} - \frac{2\pi^2}{3}\right) C_A - \frac{26}{9}\frac{C_F}{C_A} n_f T_R. \end{aligned} \tag{4.3.43b}$$

The remaining integrations are easily performed using the DL results to give

$$h^{(q)}_{3,\text{e-loss}} = \frac{C_F}{C_A}\frac{1}{2\pi}\left[D^g_{\text{e-loss}}\frac{1}{2}\nu\sinh\nu + (D^q_{\text{e-loss}} - D^g_{\text{e-loss}})(\cosh\nu - 1)\right], \tag{4.3.44a}$$

$$h^{(g)}_{3,\text{e-loss}} = \frac{1}{2\pi} D^g_{\text{e-loss}}\frac{1}{2}\nu\sinh\nu. \tag{4.3.44b}$$

4.3.3.2 Squared hard-collinear correction

We continue by considering the NNDL correction when two emissions in the nested chain receive a contribution from the finite part of the splitting function in the hard-collinear limit. In this case we directly perform the resummation. Since the two NDL corrections are strongly-ordered in angle (and hence in k_t as they happen at the hard-collinear edge of the Lund plane), we can even simplify Eq. (4.2.9) a bit further by inserting explicitly only the NDL correction associated with the larger angle (larger k_t) emission and rely on the (resummed) NDL expressions, Eqs. (4.2.25) and (4.2.27) to handle the second NDL correction.

We split the calculation in three parts, according to whether (i) the two NDL emissions are both flavour-diagonal, (ii) one is flavour-diagonal and the other flavour-changing, or (iii) both emissions are flavour-changing:

$$h_{3,\text{hc}^2} = h_{3,\text{fd}^2} + h_{3,\text{fd+fc}} + h_{3,\text{fc}^2}. \tag{4.3.45}$$

For the sake of brevity we give the integral form of each contribution below and write the full, integrated, result for the sum at the end of the section.

Two flavour diagonal. Here, one has a first hard-collinear splitting occurring either on the primary branch or on a subsidiary one. The next NDL correction has to happen in the secondary (gluon) branch of the first splitting for which we can recycle the NDL multiplicity results from Sec. 4.2.2.[12] We thus write

$$\alpha_s h^{(i)}_{3,\text{fd}^2} = \frac{C_i}{C_A}\int_0^L \mathrm{d}\ell_1 \left[\delta(\ell_1)B_i + n_g^{(\text{DL})}(\ell_1)B_{gg}\right]\,\bar{\alpha}\int_{\ell_1}^L \mathrm{d}\ell_2\, N^{(\text{NDL})}_{g,\text{hc-fd}}(L;\ell_2), \quad (4.3.46)$$

with $B_i = B_q$ (B_{gg}) for a quark (gluon) given by Eq.(4.2.21), and $N^{(\text{NDL})}_{g,\text{hc-fd}}(L;\ell_2) = N^{(\text{NDL})}_{g,\text{hc-fd}}(L-\ell_2)$ obtained from Eq. (4.2.25).

One flavour changing, one flavour diagonal. We move on to the case when one of the two hard-collinear emissions is a gluon splitting to a $q\bar{q}$ pair. This proceeds as for the flavour-diagonal case except for two modifications: (i) the first hard-collinear splitting can either be the hard gluon emission or the $g \to q\bar{q}$ splitting, and, (ii) after a $g \to q\bar{q}$ splitting a miscancellation between real and virtual splittings occur as we have discussed in several previous cases (cf. Sec. 4.3.2.3). This yields

$$\begin{aligned}\alpha_s h^{(i)}_{3,\text{fd-fc}} = \frac{C_i}{C_A}\Bigg\{ &\int_0^L \mathrm{d}\ell_1 \left[\delta(\ell_1)B_i + n_g^{(\text{DL})}(\ell_1)B_{gg}\right]\,\bar{\alpha}\int_{\ell_1}^L \mathrm{d}\ell_2\, N^{(\text{NDL})}_{g,\text{hc-fc}}(L;\ell_2) \quad (4.3.47)\\ &+ \int_0^L \mathrm{d}\ell_1 \left[\delta(\ell_1)\delta_{ig} + n_g^{(\text{DL})}(\ell_1)\right] B_{gq}\,\bar{\alpha}\int_{l_1}^L \mathrm{d}\ell_2 \left[2N^{(\text{NDL})}_{q,\text{hc-fd}}(L;\ell_2) - N^{(\text{NDL})}_{g,\text{hc-fd}}(L;\ell_2)\right]\Bigg\}.\end{aligned}$$

The first (resp. second) line corresponds to the flavour-diagonal (resp. flavour-changing) splitting happening first. The two terms in the square brackets under the ℓ_1 integration describe, as above, emissions from the primary branch or from any subsidiary one. Finally, the δ_{ig} factor on the last line ensures that $g \to q\bar{q}$ splitting on the primary branch are only included for gluon jets.

[12] As in the NDL case, the primary branch has no corrections as the real and virtual contributions from the first hard-collinear splitting cancel.

Two flavour changing. Finally we consider the case of two flavour-changing $g \to q\bar{q}$ splittings. Following the same logic and accounting again for the first splitting being either on the primary branch or on any subsidiary one, we get

$$\alpha_s h^{(i)}_{3,\mathrm{fc}^2} = \frac{C_i}{C_A}\int_0^L \mathrm{d}\ell_1 \left[\delta(\ell_1)\delta_{ig} + n_g^{(\mathrm{DL})}(\ell_1)\right] \times\bar{\alpha}\int_{\ell_1}^L \mathrm{d}\ell_2\, B_{gq}\left[2N^{(\mathrm{NDL})}_{q,\,\text{hc-fc}}(L;\ell_2) - N^{(\mathrm{NDL})}_{g,\,\text{hc-fc}}(L;\ell_2)\right]. \tag{4.3.48}$$

where $N^{(\mathrm{NDL})}_{g,\text{hc-fc}}(L;\ell_2) = N^{(\mathrm{NDL})}_{g,\text{hc-fc}}(L-\ell_2)$, obtained from Eq. (4.2.27).

Final result for $h^{(i)}_{3,\mathbf{hc}^2}$. The overall contribution to h_3 from two hard-collinear branchings is the sum of the above three terms, Eqs. (4.3.46)-(4.3.48). Using the explicit NDL results, the integrations are relatively straightforward and give

$$\begin{aligned} h^{(q)}_{3,\mathrm{hc}^2} = \frac{C_F}{4\pi}\Big\{&(B_{gg}+c_\delta B_{gq})^2\nu^2\cosh\nu + 8\left[2c_\delta B_{gg} - 2c_\delta B_q - (1-3c_\delta^2)B_{gq}\right]B_{gq}\cosh\nu \\ &+\left[4B_q(B_{gg}+(2c_\delta+1)B_{gq}) - (B_{gg}+c_\delta B_{gq})(B_{gg}+9c_\delta B_{gq})\right]\nu\sinh\nu \\ &+4(1-c_\delta^2)B_{gq}^2\nu^2 + 8\left[2c_\delta B_q - 2c_\delta B_{gg} + (1-3c_\delta^2)B_{gq}\right]B_{gq}\Big\} \end{aligned} \tag{4.3.49a}$$

$$\begin{aligned} h^{(g)}_{3,\mathrm{hc}^2} = \frac{C_A}{4\pi}\Big\{&(B_{gg}+c_\delta B_{gq})^2\nu^2\cosh\nu - 8(1-c_\delta^2)B_{gq}^2(\cosh\nu-1) \\ &+\left[(B_{gg}+c_\delta B_{gq})(3B_{gg}-5c_\delta B_{gq}) + 4(1+c_\delta)B_{gq}B_q\right]\nu\sinh\nu\Big\}. \end{aligned} \tag{4.3.49b}$$

4.3.3.3 A hard-collinear emission with a soft emission at commensurate angle

We investigate the case of a first hard-and-collinear emission which is followed by a soft-and-commensurate-angle emission, as depicted in Fig. 4.4h. To see that this contribution does not contribute at the NNDL accuracy, it is sufficient to show it at $\mathcal{O}(\alpha_s^2)$. We therefore consider a parton k_0 with colour factor C_i which radiates a hard-and-collinear gluon k_1 followed by a subsequent emission of a soft gluon k_2 at a commensurate angle. The arguments below can also be carried on with an initial flavour-changing splitting. The contribution of this system to

the Lund multiplicity at $\mathcal{O}(\alpha_s^2)$ is[13]

$$\langle N^{(\text{Lund})}_{i,\,\text{hc}\times\text{comm}}\rangle_{\mathcal{O}(\alpha_s^2)} = \left(\frac{\alpha_s}{\pi}\right)^2 \int_0^\infty \mathrm{d}\eta_1 \int_0^1 \mathrm{d}z_1\, P_{i\to ig}(z_1) \int \frac{\mathrm{d}E_2}{E_2}\frac{\mathrm{d}^2\theta_2}{2\pi} \times \left[\frac{C_A}{2}(k_2|k_1k_0) + \frac{C_A}{2}(k_2|k_1k_r) - \frac{C_A}{2}(k_2|k_0k_r)\right]\Theta(k_{t,21} > k_{t,\text{cut}}), \tag{4.3.50}$$

where $P_{i\to ig}(z)$ is the appropriate DGLAP splitting function, defined in Eq. (4.2.20), k_r is the recoiling system (at angles much larger than the ones between k_0, k_1 and k_2) and the eikonal functions $(k|ij)$ were defined in Eq. (4.2.13). Integrating over the azimuthal angle of k_2 one easily recovers, in the limit $\theta_{10}, \theta_{20}, \theta_{21} \ll 1$, the standard angular-ordered result, namely,

$$\langle N^{(\text{Lund})}_{i,\,\text{hc}\times\text{comm}}\rangle_{\mathcal{O}(\alpha_s^2)} = \bar{\alpha}\frac{\alpha_s}{\pi} \int_0^\infty \mathrm{d}\eta_1 \int_0^1 \mathrm{d}z_1\, P_{i\to ig}(z_1) \int_0^{z_1} \frac{\mathrm{d}x_2}{x_2} \int_0^{\eta_1} \mathrm{d}\eta_{21}\; \Theta(x_2 e^{-\eta_{21}} > e^{-L}), \tag{4.3.51}$$

where $\eta_{21} = -\ln(\theta_{21}/2)$, and $x_2 = 2E_2/Q$. Due to exact angular ordering being recovered, Eq. (4.3.51) represents precisely the NDL accurate contribution to the multiplicity described in Sec. 4.2.2.2, with no NNDL correction.

A key point in the above argument is that the θ_{21} angle in Eq. (4.3.51) is bounded by the physical angle θ_{10}, i.e. the angle between the daughter partons after the k_0k_1 branching. Technically, working in the collinear limit, one could choose to impose angular-ordering with a different definition of the angle (e.g. the angle of the emission with respect to the parent parton). In this case, the contribution discussed in this section would no longer vanish. However, such a change would also affect the definition of η in the hard-collinear endpoint, Eq. (4.3.4), reshuffling a contribution between the hard-collinear and hard-matrix-element coefficients. We have checked explicitly that this does not change the final resummed result.

4.3.3.4 A primary large-angle emission

In Sec. 4.2.2 we showed that a first soft-and-large-angle primary emission does not yield a NDL correction. We now study the effect of such a soft-and-large-angle

[13] This expression already accounts for the cancellation of the term proportional to $C_i(k_2|k_0k_r)$ in the square bracket including both real and virtual contributions for the k_1 gluon.

emission on subsequent ones. Concretely, following the discussion in Sec. 4.3.1 we investigate two possible kinematic configurations for the second emission: (i) soft and at commensurate angles to the first, Fig. 4.4i, and (ii) soft and collinear with $k_t \sim k_{t,\text{cut}}$, Fig. 4.4k. We therefore write

$$D_{\text{la}} = D_{\text{la}^2} + D_{\text{la}\times k_t}. \tag{4.3.52}$$

We show below that the contributions cancel each other exactly.

We start with the configuration in Fig. 4.4i, where an initial system $(k_0 k_r)$ emits a soft-and-large-angle parton, k_1, which then radiates a soft emission k_2 at a commensurate angle. The contribution to the Lund multiplicity is (after cancelling the real and virtual contributions for the first emission)

$$\begin{aligned}\langle N^{(\text{Lund})}_{i,\text{la}^2}\rangle_{\mathcal{O}(\alpha_s^2)} &= \left(\frac{\alpha_s}{\pi}\right)^2 \int \frac{\mathrm{d}E_1}{E_1}\frac{\mathrm{d}^2\theta_1}{2\pi}\int \frac{\mathrm{d}E_2}{E_2}\frac{\mathrm{d}^2\theta_2}{2\pi} \\ &\times C_i(k_1|k_0k_r)\left[\frac{C_A}{2}(k_2|k_1k_0)+\frac{C_A}{2}(k_2|k_1k_r)-\frac{C_A}{2}(k_2|k_0k_r)\right]\Theta(k_{t,21}>k_{t,\text{cut}}).\end{aligned} \tag{4.3.53}$$

After integrating over the solid angle of the second emission and subtracting the DL term in which the two emissions are angular-ordered, we obtain the following NNDL correction

$$\delta N^{(\text{NNDL})}_{i,\text{la}^2} = \frac{C_i}{C_A}\frac{\bar{\alpha}L^2}{2}\frac{\alpha_s}{2\pi}D_{\text{la}^2} \quad \text{with} \quad D_{\text{la}^2} = -\frac{\pi^2}{6}C_A. \tag{4.3.54}$$

Let us now move to the case where the first soft-and-large-angle emission is followed by a soft-and-collinear emission with $k_t \sim k_{t,\text{cut}}$, as in Fig. 4.4k. The Lund multiplicity at $\mathcal{O}(\alpha_s^2)$ is given by

$$\langle N^{(\text{Lund})}_{i,\text{la}\times k_t}\rangle_{\mathcal{O}(\alpha_s^2)} = \frac{4\alpha_s^2 C_i C_A}{\pi^2}\int \mathrm{d}\eta_1 \int \frac{\mathrm{d}k_{t,1}}{k_{t,1}}\int_{\eta_1}^{\infty}\mathrm{d}\eta_2\int\frac{\mathrm{d}z_2}{z_2}\Theta(k_{t,21}>k_{t,\text{cut}}), \tag{4.3.55}$$

where we have replaced the eikonal factor for the second emission by its soft-and-collinear limit. The NNDL correction stems from taking into account the exact expression for $k_{t,21}$, namely

$$k_{t,21} = E_2\sin(\theta_{21}) \approx E_2\theta_{21} \approx z_2E_1\theta_{21} \approx z_2k_{t,1}\,2\cosh\eta_1\,e^{-\eta_{21}}, \tag{4.3.56}$$

where, for the last equality, we have used the generalisation of Eq. (4.2.4) beyond the collinear limit, $E_1 = k_{t,1}\cosh\eta_1$, and $\theta_{21} \approx 2e^{-\eta_{21}}$. This expression differs

from the soft-collinear limit by a factor $2e^{-\eta_1}\cosh\eta_1 = 1 + e^{-2\eta_1}$, so that, after subtracting the DL contribution from Eq. (4.3.55), one is left with the NNDL correction (with $\ell_1 = \ln(Q/k_{t,1})$)

$$\langle N^{(\text{Lund})}_{i,\text{la}\times k_t}\rangle_{\mathcal{O}(\alpha_s^2)} = \frac{4\alpha_s^2 C_i C_A}{\pi^2}\int_0^L d\ell_1 \int_0^{L-\ell_1} d\eta_{21}\int_0^\infty \mathrm{d}\eta_1 \ln\!\left(1+e^{-2\eta_1}\right) \qquad (4.3.57)$$
$$= \frac{C_i}{C_A}\frac{\bar{\alpha}L^2}{2}\frac{\alpha_s}{2\pi}D_{\text{la}\times k_t} \qquad \text{with} \qquad D_{\text{la}\times k_t} = \frac{\pi^2}{6}C_A = -D_{\text{la}^2}.$$

The sum of (4.3.54) and (4.3.57) therefore vanishes and it is relatively straightforward to see that this relation holds to all orders.[14]

4.3.3.5 Three emissions at commensurate angles

We consider the case where a first soft-and-collinear emission k_1 is followed by two subsequent emissions, k_2 and k_3, strongly ordered in energy, $E_1 \gg E_2 \gg E_3$, and at commensurate angles, $\theta_1 \sim \theta_2 \sim \theta_3$, as depicted in Fig. 4.4j. In the NDL limit, once both real and virtual emissions are taken into account, the only left-over contribution comes from the angular-ordered DL result, $\theta_{23} < \theta_{12} < \theta_1$, proportional to $C_i C_A^2$. We show here that this is still the case at NNDL accuracy, i.e. that the contribution of Fig. 4.4j vanishes.

It is sufficient to consider this configuration at $\mathcal{O}(\alpha_s^3)$. The first gluon, k_1, is emitted off a (k_0, k_r) dipole according to the eikonal factor $(k_1|k_0, k_r)$ in Eq. (4.2.13), where for a collinear k_1 emission the specific choice of the large-angle recoiling momentum k_r is irrelevant. The second gluon k_2 can then be emitted from any of the three dipoles (k_0, k_r), (k_0, k_1) or (k_1, k_r) resulting in the combination in Eq. (4.3.30). Finally, the third emission k_3 can be emitted from any dipole in the $(k_0,\ k_1,\ k_2,\ k_r)$ system. The full matrix element for all three emissions can be deduced from the expression in Refs. [71, 72], valid for $E_3 \sim E_2$, which, after

[14] One can for example realise that both contributions shift the boundary of the secondary Lund plane spawned by the first soft-large-angle emission by an equal amount proportional to $\int_0^\infty \mathrm{d}\eta \ln\!\left(1+e^{-2\eta}\right)$. The "$\text{la}^2$" shifts the large-angle boundary of the secondary plane, reducing the phase-space, while the "$\text{la}\times k_t$" contributions shifts the lower edge, enhancing the phase-space by the same amount. This results in an overall shift which has no net effect on the NNDL multiplicity.

taking the limit $E_3 \ll E_2$ can be cast into the following form:

$$\begin{aligned} C_i\frac{C_A^2}{4}(1|0r)\Big\{&(2|10)\Big[(3|20)+(3|21)+(3|1r)-(3|0r)\Big]\\ &+(2|1r)\Big[(3|2r)+(3|21)+(3|10)-(3|0r)\Big]\\ &-(2|0r)\Big[(3|20)+(3|2r)+(3|10)+(3|1r)\Big]\Big\} \\ +C_i^2\frac{C_A}{2}(1|0r)\Big\{&(3|0r)\Big[(2|10)+(2|1r)\Big]\\ &+(2|0r)\Big[(3|20)+(3|2r)+(3|10)+(3|1r)-2(3|0r)\Big]\Big\}+C_i^3(1|0r)(2|0r)(3|0r), \end{aligned} \tag{4.3.58}$$

where for the sake of readability we used the shorthand notation $(c|ab)$ to denote the factor $(k_c|k_ak_b)$.

Besides the matrix element proportional to Eq. (4.3.58) we need to account for the fact that each of the three emissions can be either real or virtual. Summing over all possible emission configurations we find that the Lund multiplicity at $\mathcal{O}\left(\alpha_s^3\right)$ is[15]

$$\begin{aligned} \langle N_{i,3\text{comm}}^{(\text{Lund})}\rangle_{\mathcal{O}(\alpha_s^3)} = &\left(\frac{\alpha_s C_A}{2\pi}\right)^3\frac{2C_i}{C_A}\int\frac{\mathrm{d}E_1}{E_1}\frac{\mathrm{d}^2\theta_1}{2\pi}\int\frac{\mathrm{d}E_2}{E_2}\frac{\mathrm{d}^2\theta_2}{2\pi}\int\frac{\mathrm{d}E_3}{E_3}\frac{\mathrm{d}^2\theta_3}{2\pi}(k_1|k_0k_r)\\ &\times\Big\{(k_2|k_1k_0)\left[(k_3|k_2k_0)+(k_3|k_2k_1)-(k_3|k_1k_0)\right]\\ &+(k_2|k_1k_r)\left[(k_3|k_2k_r)+(k_3|k_2k_1)-(k_3|k_1k_r)\right]\\ &-(k_2|k_0k_r)\left[(k_3|k_2k_0)+(k_3|k_2k_r)-(k_3|k_0k_r)\right]\Big\}\times\Theta(k_{t,3}>k_{t,\text{cut}}). \end{aligned} \tag{4.3.59}$$

A few comments about Eq. (4.3.59) are in order. Since all emissions are above the $k_{t,\text{cut}}$, we can ignore differences in the $k_{t,3}$ definition, i.e. we can treat $k_{t,30}, k_{t,31}, k_{t,32}$ indistinctly. More interestingly, only the term proportional to $C_iC_A^2$ survives, as was already the case at DL accuracy.

At small angles, all the eikonal factors can be simplified according to $(c|ab)\approx 2\theta_{ab}^2/(\theta_{ac}^2\theta_{bc}^2)$ for $b,c\neq r$ and $(c|ar)\approx 2/\theta_{ac}^2$. After performing the (2-dimensional) integrations over θ_2 and θ_3, one finds that Eq. (4.3.59) reproduces angular-ordered result with no NNDL correction. Thus, the contribution corresponding to Fig. 4.4j vanishes to all orders.

[15]The contributions proportional to $\Theta(k_{t,2}>k_{t,\text{cut}})$ and $\Theta(k_{t,1}>k_{t,\text{cut}})$ vanish when summing the cases where the third soft emission is either real or virtual.

4.3.4 Corrections involving the running of the strong coupling

The last family of NNDL corrections we have to compute is the one involving the running of the QCD coupling. Since one-loop running is sufficient, we can follow a similar strategy as for two hard-collinear emissions (Sec. 4.3.3.2) and insert an extra subleading correction in the NDL calculation.

Naturally, such a calculation would make use of the NDL multiplicity $N_{i,\mathrm{rc}}^{(\mathrm{NDL})}(L;\ell)$ of a parton of flavour i initially created at a transverse momentum scale $e^{-\ell}Q$ down to a transverse momentum cut $e^{-L}Q$. However, since the QCD running coupling is not scale invariant, $N_{i,\mathrm{rc}}^{(\mathrm{NDL})}(L;\ell) \neq N_{i,\mathrm{rc}}^{(\mathrm{NDL})}(L-\ell)$ one cannot simply reuse Eq. (4.2.19) as we did for the hard-collinear NDL corrections. Instead, $N_{i,\mathrm{rc}}^{(\mathrm{NDL})}(L;\ell)$ has to be explicitly computed. Following the same strategy as in Sec. 4.2.2.1, we get

$$\begin{aligned} N_{i,\mathrm{rc}}^{(\mathrm{NDL})}(L;\ell) &= \frac{C_i}{C_A}\int_{\ell}^{L} \mathrm{d}\ell_1 \left[\delta(\ell_1) + n_g^{(\mathrm{DL})}(\ell_1;\ell)\right] \bar{\alpha}\int_{\ell_1}^{L} \mathrm{d}\ell_2 (2\alpha_s\beta_0\ell_2)\,(\ell_2-\ell_1)\, N_g^{(\mathrm{DL})}(L;\ell_2), \\ &= \frac{C_i}{C_A}\frac{\beta_0}{2}\sqrt{\frac{\alpha_s\pi}{2C_A}}\left[(\nu^2-\nu_0^2-1)\sinh(\nu-\nu_0) + (\nu-\nu_0)\cosh(\nu-\nu_0)\right], \end{aligned} \tag{4.3.60}$$

with $\nu_0 = \sqrt{\bar{\alpha}}\ell$.

4.3.4.1 Squared running-coupling correction

We first consider the case of NNDL corrections proportional to β_0^2. If we expand the running coupling according to

$$\alpha_s(k_t) = \frac{\alpha_s}{1-2\alpha_s\beta_0\ln\frac{Q}{k_t}} \approx \alpha_s + 2\alpha_s^2\beta_0\ln\left(Q/k_t\right) + 4\beta_0^2\alpha_s^3\ln\left(Q/k_t\right)^2 + \mathcal{O}\left(\alpha_s^4\right), \tag{4.3.61}$$

we see that we can get NNDL corrections proportional to β_0^2, h_{3,β_0^2}, either by having a single $\mathcal{O}\left([\alpha_s\beta_0\ln(Q/k_t)]^2\right)$ correction to one of the DL emissions, $h_{3,\mathcal{O}\left(\beta_0^2\right)}$, or by having $\mathcal{O}\left(\alpha_s\beta_0\ln(Q/k_t)\right)$ corrections to two emissions along the chain of nested

emissions, $h_{3,\beta_0\times\beta_0}$, Fig. 4.4m. The two cases can be written as

$$h^{(i)}_{3,\beta_0^2} = h^{(i)}_{3,\mathcal{O}(\beta_0^2)} + h^{(i)}_{3,\beta_0\times\beta_0} \tag{4.3.62}$$

$$\alpha_s h^{(i)}_{3,\mathcal{O}(\beta_0^2)} = \frac{C_i}{C_A}\int_0^L \mathrm{d}\ell_1 \left[\delta(\ell_1) + n_g^{(\mathrm{DL})}(\ell_1)\right] \bar{\alpha}\int_{\ell_1}^L \mathrm{d}\ell_2 (2\alpha_s\beta_0\ell_2)^2\,(\ell_2-\ell_1)\,N_g^{(\mathrm{DL})}(L;\ell_2), \tag{4.3.63}$$

$$\alpha_s h^{(i)}_{3,\beta_0\times\beta_0} = \frac{C_i}{C_A}\int_0^L \mathrm{d}\ell_1 \left[\delta(\ell_1) + n_g^{(\mathrm{DL})}(\ell_1)\right] \bar{\alpha}\int_{\ell_1}^L \mathrm{d}\ell_2 (2\alpha_s\beta_0\ell_2)\,(\ell_2-\ell_1)\,N_{g,\mathrm{rc}}^{(\mathrm{NDL})}(L;\ell_2). \tag{4.3.64}$$

For the first of the two contributions, a DL emission, which was created at scale $k_{t,1} = Qe^{-\ell_1}$, dresses a gluon with a β_0^2 correction down to the scale $k_{t,2} = Qe^{-\ell_2}$. For the second contribution, the β_0 correction occurs at the scale ℓ_2 and a second NDL correction happens at a lower k_t scale as encoded by $N_{g,\mathrm{rc}}^{(\mathrm{NDL})}(L;\ell_2)$, given by Eq. (4.2.18). Evaluating the integrals using the known DL and NDL multiplicities, we get

$$h^{(i)}_{3,\beta_0^2}(\nu) = \frac{C_i}{C_A}\frac{\pi\beta_0^2}{16C_A}\left[3\nu(2\nu^2-1)\sinh\nu + (\nu^4+3\nu^2)\cosh\nu\right]. \tag{4.3.65}$$

4.3.4.2 Running-coupling and hard-collinear correction

We now consider the case where one emission in the chain of nested emissions receives running coupling correction $\mathcal{O}(\beta_0)$, while also allowing one hard-and-collinear splitting. As in Sec. 4.2.2.2, we split the discussion in terms of whether the hard-collinear splitting is flavour-conserving or flavour-changing. Accordingly, we write the NNDL correction as

$$h_{3,\beta_0\times\mathrm{hc}} = h_{3,\beta_0\times\mathrm{hc,fd}} + h_{3,\beta_0\times\mathrm{hc,fc}}. \tag{4.3.66}$$

Flavour-diagonal. In the case of a flavour-diagonal hard-collinear splitting, we can write

$$\begin{aligned}\alpha_s h^{(i)}_{3,\beta_0\times\mathrm{hc,fd}} = \frac{C_i}{C_A}\Bigg[&\int_0^L \mathrm{d}\ell_1 \left[\delta(\ell_1)B_i + n_g^{(\mathrm{DL})}(\ell_1)B_{gg}\right] \bar{\alpha}\int_{\ell_1}^L \mathrm{d}\ell_2\,(2\alpha_s\beta_0\ell_2)\,N_g^{(\mathrm{DL})}(L;\ell_2)\\ &+\int_0^L \mathrm{d}\ell_1 \left[\delta(\ell_1)B_i + n_g^{(\mathrm{DL})}(\ell_1)B_{gg}\right] \bar{\alpha}\int_{\ell_1}^L \mathrm{d}\ell_2\,N_{g,\mathrm{rc}}^{(\mathrm{NDL})}(L;\ell_2)\\ &+\int_0^L \mathrm{d}\ell_1 n_{\mathrm{RC}}^{(\mathrm{NDL})}(\ell_1)\,\bar{\alpha}\int_{\ell_1}^L \mathrm{d}\ell_2 B_{gg}\,N_g^{(\mathrm{DL})}(L;\ell_2)\Bigg].\end{aligned} \tag{4.3.67}$$

where $n_{\text{RC}}^{(\text{NDL})}(\ell_1)$ is defined as the derivative of Eq. (4.2.18) for gluons with respect to L. This expression covers the three physical cases: if the hard-collinear splitting occurs at a scale ℓ_2, the running-coupling correction can happen either for the same emission (the first line), or for a later emission (the second line), or for an earlier emission (the last line). For the first two lines, the hard-collinear emission can either be from the primary branch, proportional to $\delta(\ell_1)$ with $B_i = B_q$ for a quark and $B_i = B_{gg}$ for a gluon, or from a subsequent gluon emission.

Flavour-changing. The case where the hard-collinear splitting is a $g \to q\bar{q}$ branching is computed the same way with the usual care that after a real $g \to q\bar{q}$ branching both branches behave like quarks while the virtual corrections involve gluon-initiated emissions. Modulo this detail, we still have to include three contributions for the running-coupling NDL correction happening earlier, at the same emission, or later than the $g \to q\bar{q}$ branching:

$$\begin{aligned}\alpha_s h^{(i)}_{3,\beta_0\times\text{hc,fc}} = \frac{C_i}{C_A} B_{gq} \Bigg\{ &\int_0^L \mathrm{d}\ell_1 n_{\text{rc}}^{(\text{NDL})}(\ell_1)\, \bar{\alpha} \int_{\ell_1}^L \mathrm{d}\ell_2 \left[2N_q^{(\text{DL})}(L;\ell_2) - N_g^{(\text{DL})}(L;\ell_2)\right] \\ + \int_0^L \mathrm{d}\ell_1 \left[\delta_{ig}\delta(\ell_1) + n_g^{(\text{DL})}(\ell_1)\right] &\bar{\alpha} \int_{\ell_1}^L \mathrm{d}\ell_2\, (2\alpha_s\beta_0\ell_2) \left[2N_q^{(\text{DL})}(L;\ell_2) - N_g^{(\text{DL})}(L;\ell_2)\right] \\ + \int_0^L \mathrm{d}\ell_1 \left[\delta_{ig}\delta(\ell_1) + n_g^{(\text{DL})}(\ell_1)\right] &\bar{\alpha} \int_{\ell_1}^L \mathrm{d}\ell_2\, \frac{2C_F - C_A}{C_A} N_{g,\text{rc}}^{(\text{NDL})}(L;\ell_2) \Bigg\},\end{aligned} \tag{4.3.68}$$

where we have used that $N_{q,\text{rc}}^{(\text{NDL})} = C_F N_{g,\text{rc}}^{(\text{NDL})}/C_A$ in the last line.

Integrated contribution. Evaluating the integrals in the flavour-diagonal and flavour-changing contributions, we get

$$\begin{aligned}h^{(q)}_{3,\beta_0\times\text{hc}} = \frac{C_F}{C_A}\frac{\beta_0}{4}\Big\{&(B_{gg} + c_\delta B_{gq})\nu^3 \sinh\nu + [2B_q - 2B_{gg} + (6 - 8c_\delta)B_{gq}]\,\nu\sinh\nu \\ &+ 2(B_q + B_{gg} + B_{gq})\nu^2\cosh\nu - 4(1-c_\delta)B_{gq}(2\cosh\nu - 2 + \nu^2)\Big\},\end{aligned} \tag{4.3.69a}$$

$$\begin{aligned}h^{(g)}_{3,\beta_0\times\text{hc}} = \frac{\beta_0}{4}\Big\{&(B_{gg} + c_\delta B_{gq})\nu^3 \sinh\nu + 6(1-c_\delta)B_{gq}\nu\sinh\nu \\ &+ 2\left[2B_{gg} + (1+c_\delta)B_{gq}\right]\nu^2\cosh\nu - 8B_{gq}(1-c_\delta)(\cosh\nu - 1)\Big\}.\end{aligned} \tag{4.3.69b}$$

Contribution	Coefficient
Running coupling	$\beta_0 = \frac{11C_A - 4n_f T_R}{12\pi}$
Hard-collinear correction	$B_q = -\frac{3}{4}$, $B_{gg} = -\frac{11}{12}$, $B_{gq} = \frac{n_f T_R}{3C_A}$
Collinear endpoint	$D_{\text{end}}^{q\to qg} = C_F(3 + 3\ln 2 - \frac{\pi^2}{3})$
	$D_{\text{end}}^{g\to gg} = C_A(\frac{137}{36} + \frac{11}{3}\ln 2 - \frac{\pi^2}{3})$
	$D_{\text{end}}^{g\to q\bar{q}} = n_f T_R(-\frac{29}{18} - \frac{4}{3}\ln 2)$
Hard matrix-element	$D_{\text{hme}}^{qqg} = C_F(\frac{\pi^2}{6} - \frac{7}{4})$, $D_{\text{hme}}^{ggg} = C_A(\frac{\pi^2}{6} - \frac{49}{36})$, $D_{\text{hme}}^{gq\bar{q}} = n_f T_R \frac{2}{9}$
Commensurate k_t and angle	$D_{\text{pair}}^{q\bar{q}} = \frac{13}{9} n_f T_R$, $D_{\text{pair}}^{gg} = (\frac{\pi^2}{6} - \frac{67}{18})C_A$
	$K = \left(\frac{67}{18} - \frac{\pi^2}{6}\right) C_A - \frac{10}{9} n_f T_R$
Clustering	$D_{\text{clust}}^{(\text{prim})} = -\frac{5\pi^2}{54}$, $D_{\text{clust}}^{(\text{sec})} = \frac{\pi^2}{27}$
Energy loss	$D_{\text{e-loss}}^{q} = \frac{7}{2}C_A + (\frac{5}{2} - \frac{2\pi^2}{3})C_F$
	$D_{\text{e-loss}}^{g} = (\frac{67}{9} - \frac{2\pi^2}{3})C_A - \frac{26}{9}\frac{C_F}{C_A} n_f T_R$

Table 4.2: Coefficients entering the NNDL h_3 function.

4.3.5 Final result

For completeness, we gather here the full expression for the NNDL multiplicity, as obtained from Eq. (4.3.2) with the individual contributions computed in the previous subsections (see also Tab. 4.1). We give results for both $\langle N_Z^{(\text{Lund})} \rangle$ and $\langle N_H^{(\text{Lund})} \rangle$ corresponding respectively to rest-frame $e^+e^- \to Z \to q\bar{q}$ and $e^+e^- \to H \to gg$ collisions with centre-of-mass energy Q. We define $\alpha_s = \alpha_s(Q)$, $L = \ln(Q/k_{t,\text{cut}})$, $\xi = \alpha_s L^2$, $\nu = \sqrt{2C_A \alpha_s L^2/\pi}$ and $c_\delta = (2C_F - C_A)/C_A$. The equations are written in terms of coefficients summarised in Tab. 4.2.

The generic all-order structure of the Lund multiplicity is

$$\langle N_{Z,H}^{(\text{Lund})}(L;\alpha_s) \rangle = 2\Big[h_1^{(q,g)}(\xi) + \sqrt{\alpha_s} h_2^{(q,g)}(\xi) + \alpha_s h_3^{(q,g)}(\xi)\Big]. \tag{4.3.70}$$

Using $\nu = \sqrt{2C_A\xi/\pi}$, the DL contribution is

$$h_1^{(q)} = 1 + \frac{C_F}{C_A}(\cosh\nu - 1) \tag{4.3.71a}$$

$$h_1^{(g)} = \cosh\nu, \tag{4.3.71b}$$

the NDL function h_2 is given by

$$h_2^{(q)} \equiv h_{2,\text{coll}}^{(q)} = \frac{C_F}{\sqrt{2\pi C_A}}\Big\{\frac{\pi\beta_0}{2C_A}\Big[(\nu^2-1)\sinh\nu+\nu\cosh\nu\Big]+(B_{gg}+c_\delta B_{gq})\nu\cosh\nu$$
$$+\Big[2B_q-B_{gg}+(2-3c_\delta)\,B_{gq}\Big]\sinh\nu+2(c_\delta-1)B_{gq}\nu\Big\}, \tag{4.3.72a}$$

$$h_2^{(g)} \equiv h_{2,\text{coll}}^{(q)} = \sqrt{\frac{C_A}{2\pi}}\Big\{\frac{\pi\beta_0}{2C_A}\Big[(\nu^2-1)\sinh\nu+\nu\cosh\nu\Big]$$
$$+(B_{gg}+c_\delta B_{gq})\nu\cosh\nu+\Big[B_{gg}+(2-c_\delta)B_{gq}\Big]\sinh\nu\Big\}. \tag{4.3.72b}$$

The DL (4.3.71) and NDL (4.3.72) accurate expressions also apply to any k_t-based jet multiplicity, for example Durham multiplicity [57]. We write the NDL functions in Eq. (4.3.72) with an optional collinear 'coll' subscript to facilitate the discussion in Chap. 5. The main result of this chapter, and that of Ref. [2], is the NNDL function h_3 which is found to be

$$2\pi h_3^{(q)} = 2\pi h_{3,\text{coll}}^{(q)} + 2\pi h_{3,e^+e^-,\text{la}}^{(q)} \tag{4.3.73}$$

$$2\pi h_{3,e^+e^-,\text{la}}^{(q)} = D_{\text{hme}}^{qqg}\cosh\nu \tag{4.3.74}$$

$$2\pi h_{3,\text{coll}}^{(q)} = D_{\text{end}}^{q\to qg}+\Big(D_{\text{end}}^{g\to gg}+D_{\text{end}}^{g\to q\bar q}\Big)\frac{C_F}{C_A}(\cosh\nu-1) \tag{4.3.75}$$
$$+\frac{C_F}{C_A}\Big[(1-c_\delta)D_{\text{pair}}^{q\bar q}(\cosh\nu-1)+\Big(K+D_{\text{pair}}^{gg}+c_\delta D_{\text{pair}}^{q\bar q}\Big)\frac{\nu}{2}\sinh\nu\Big]$$
$$+C_F\Big[\Big(\cosh\nu-1-\frac{1-c_\delta}{4}\nu^2\Big)D_{\text{clust}}^{(\text{prim})}+(\cosh\nu-1)D_{\text{clust}}^{(\text{sec})}\Big]$$
$$+\frac{C_F}{C_A}\Big[D_{\text{e-loss}}^{g}\frac{\nu}{2}\sinh\nu+(D_{\text{e-loss}}^{q}-D_{\text{e-loss}}^{g})\,(\cosh\nu-1)\Big]$$
$$+\frac{C_F}{2}\Big\{(B_{gg}+c_\delta B_{gq})^2\nu^2\cosh\nu+8\Big[2c_\delta B_{gg}-2c_\delta B_q-(1-3c_\delta^2)B_{gq}\Big]\,B_{gq}\cosh\nu$$
$$+[4B_q(B_{gg}+(2c_\delta+1)B_{gq})-(B_{gg}+c_\delta B_{gq})(B_{gg}+9c_\delta B_{gq})]\,\nu\sinh\nu$$
$$+4(1-c_\delta^2)B_{gq}^2\nu^2+8\Big[2c_\delta B_q-2c_\delta B_{gg}+(1-3c_\delta^2)B_{gq}\Big]\,B_{gq}\Big\}$$
$$+\frac{C_F}{C_A}\frac{\pi\beta_0}{2}\Big\{(B_{gg}+c_\delta B_{gq})\nu^3\sinh\nu+[2B_q-2B_{gg}+(6-8c_\delta)B_{gq}]\,\nu\sinh\nu$$
$$+2(B_q+B_{gg}+B_{gq})\nu^2\cosh\nu-4(1-c_\delta)B_{gq}(2\cosh\nu-2+\nu^2)\Big\}$$
$$+\frac{C_F}{C_A}\frac{\pi^2\beta_0^2}{8C_A}\Big[3\nu(2\nu^2-1)\sinh\nu+(\nu^4+3\nu^2)\cosh\nu\Big]$$

for quarks, and

$$2\pi h_3^{(g)} = 2\pi h_{3,\text{coll}}^{(g)} + 2\pi h_{3,e^+e^-,\text{la}}^{(g)} \tag{4.3.76}$$

$$2\pi h_{3,e^+e^-,\text{la}}^{(g)} = \left[D_{\text{hme}}^{ggg}\cosh\nu + D_{\text{hme}}^{gq\bar{q}}\left(c_\delta\cosh\nu + 1 - c_\delta\right)\right] \tag{4.3.77}$$

$$\begin{aligned} 2\pi h_{3,\text{coll}}^{(g)} = {} & \left(D_{\text{end}}^{g\to gg} + D_{\text{end}}^{g\to q\bar{q}}\right)\cosh\nu \\ & + \left[(1-c_\delta)D_{\text{pair}}^{q\bar{q}}(\cosh\nu - 1) + \left(K + D_{\text{pair}}^{gg} + c_\delta D_{\text{pair}}^{q\bar{q}}\right)\frac{\nu}{2}\sinh\nu\right] \\ & + C_A\left(D_{\text{clust}}^{(\text{prim})} + D_{\text{clust}}^{(\text{sec})}\right)(\cosh\nu - 1) + D_{\text{e-loss}}^{g}\frac{\nu}{2}\sinh\nu \\ & + \frac{C_A}{2}\Big\{(B_{gg} + c_\delta B_{gq})^2\nu^2\cosh\nu - 8(1-c_\delta^2)B_{gq}^2(\cosh\nu - 1) \\ & \quad + \left[(B_{gg} + c_\delta B_{gq})(3B_{gg} - 5c_\delta B_{gq}) + 4(1+c_\delta)B_{gq}B_q\right]\nu\sinh\nu\Big\} \\ & + \frac{\pi\beta_0}{2}\Big\{(B_{gg} + c_\delta B_{gq})\nu^3\sinh\nu + 6(1-c_\delta)B_{gq}\nu\sinh\nu \\ & \quad + 2\left[2B_{gg} + (1+c_\delta)B_{gq}\right]\nu^2\cosh\nu - 8B_{gq}(1-c_\delta)(\cosh\nu - 1)\Big\} \\ & + \frac{\pi^2\beta_0^2}{8C_A}\left[3\nu(2\nu^2 - 1)\sinh\nu + (\nu^4 + 3\nu^2)\cosh\nu\right] \end{aligned} \tag{4.3.78}$$

for gluons, with different contributions separated in different colours, except for those involving ingredients already present at NDL accuracy which have been gathered (in orange). We note that we have artificially split the final result with respect to whether a correction was associated with collinear physics ($h_{3,\text{coll}}^{(q,g)}$) or large-angle physics ($h_{3,e^+e^-,\text{la}}^{(q,g)}$) in order to facilitate the discussion in Chap. 5, where it will prove very useful.

At NNDL accuracy, the Cambridge multiplicity is simply obtained from Eq. (4.3.70):

$$\langle N^{(\text{Cam})}(\alpha_s, L)\rangle = \langle N^{(\text{Lund})}(\alpha_s, L)\rangle + \frac{\alpha_s C_i}{2\pi}\frac{\pi^2}{6}. \tag{4.3.79}$$

To gain insight into the relative sizes of the NNDL contributions, the top panels of Fig. 4.6 show the ratios $h_{2,3}/h_1$ as a function of $\xi = \alpha_s L^2$ for quark (left) and gluon (right) hemispheres. We note that the NDL corrections are negative at low values of ξ, driven by hard-collinear corrections, while the NNDL result remains positive for all ξ. Unless we go to large values of ξ, the NNDL function h_3 is roughly of the same magnitude as the NDL function h_2. That said, for physical values of $\alpha_s \sim 0.1$,

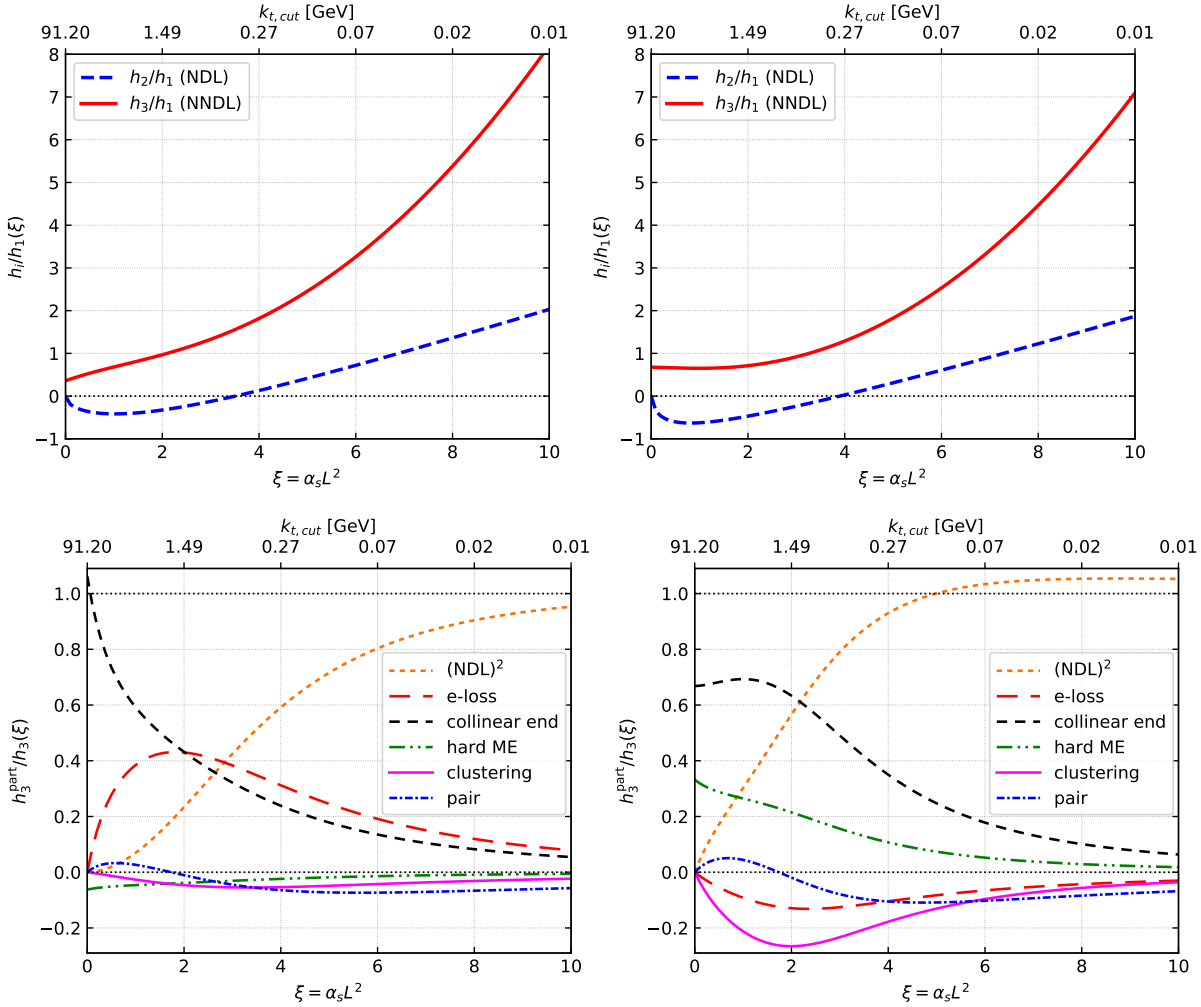


Figure 4.6: Top: Ratio of NDL (blue) and NNDL (red) resummation functions to the DL result as a function of $\alpha_s L^2$ for quark (left) and gluon hemispheres (right). Bottom: Relative weight of the NNDL contributions to h_3 for quark (left) and gluon hemispheres (right). For concreteness, the upper x-axis of each plot shows the value of $k_{t,\mathrm{cut}}$, which corresponds to a given ξ at LEP energies.

the size of the NNDL corrections, $\alpha_s h_3(\xi)$, would be commensurate to the NDL contribution $\sqrt{\alpha_s} h_2(\xi)$, motivating the study of their phenomenological impact, which we carry out in Sec. 4.4.2. Theoretically, the observed poor convergence motivates further investigations into the size of N^{3}DL corrections to the Lund multiplicity, which we leave for future work.

In the bottom row of Fig. 4.6, we investigate the relative sizes of the NNDL contributions to the total $h_3(\xi)$ for quarks (left) and gluons (right), with line colours

matching those in Eqs. (4.3.73) and (4.3.76). For conciseness, we have grouped the corrections stemming only from NDL hard-collinear or running coupling corrections into a unique $(\text{NDL})^2$ contribution, i.e. $h_{3,\text{NDL}^2} \equiv h_{3,\text{hc}^2} + h_{3,\beta_0\times\text{hc}} + h_{3,\beta_0^2}$ (Secs. 4.3.3.2 and 4.3.4). We note that there are particularly large cancellations between the $h_{3,\beta_0\times\text{hc}}$ and h_{3,β_0^2} functions, further motivating their grouping.

We observe that these $(\text{NDL})^2$ corrections become dominant when $\xi \gtrsim 3$ for both the quark and gluon cases. This can be traced to the running-coupling corrections which, relative to h_1, scale like ξ^2 (ξ for the NDL contribution). More generally, one should expect that pure running-coupling corrections would bring contributions of order ξ^{k-1} to h_k/h_1, so that for $\sqrt{\xi}(\alpha_s L) = \sqrt{\alpha_s}\xi \sim 1$, the N^kDL approach of expanding in series of $\sqrt{\alpha_s}$ at fixed $\xi = \alpha_s L^2$, Eq. (2.3.6), should be revisited so as to resum an arbitrary number of running-coupling corrections.[16] This is actually reminiscent of the LL, NLL, NNLL, ... logarithmic counting where running-coupling corrections are included already in the LL Sudakov factor [52]. It is also interesting to recall that, while the original result from Ref. [57] is strictly speaking NDL, the use of a generating functional potentially includes an arbitrary number of running-coupling corrections, partly resumming them in the above sense to all orders. In this context we have checked explicitly that parts of the h_{3,NDL^2} function are already included in the expansion of Eq. (25) from Ref. [57] to NNDL order, in particular terms which dominate at large values of ξ (i.e. the terms proportional to ξ^2, $\xi^{3/2}$ and ξ, multiplied by $\cosh\nu$ or $\sinh\nu$). Further investigation on how to include this in a perturbatively controlled way in our formalism is left for future work.

For phenomenologically-accessible values of ξ, $\xi \lesssim 5$, we observe in Fig. 4.6 that the contributions from the collinear endpoint and energy loss are in the 20-40% range[17] for the quark case. For gluons we observe a larger sensitivity, $\sim 10\%$, to other contributions, like hard matrix-element, clustering and soft pairs.

[16] In this case, mixed running-coupling and hard-collinear corrections are expected to be numerically significant.

[17] Or even more at small ξ, although this region would in practice be affected by fixed-order corrections.

The relative weight of each contribution to the NNDL multiplicity is an important piece of information to gauge the constraining power of Lund multiplicity on parton shower validation in the spirit of Sec. 3.3, as it probes the full multiple branching structure of QCD. We explicitly demonstrated this in Sec. 3.2 at full colour where the NLL PanScales family of showers were shown to successfully reproduce the NDL jet multiplicity analytic resummation, Eq. (3.2.4), among other observables. Thus, the NNDL analytic result presented in this chapter would be a key element towards testing a future generation of NNLL showers. Since, as discussed above, some of the physical contributions to h_3 can be relatively small, an excellent control of the numerical precision in the shower would be required.

4.4 Validation and phenomenology

In this section we first cross-check the fixed-order expansion of the resummed result against the `Event2` generator [73, 74]. We then discuss the phenomenological impact of the NNDL resummation at LEP energies, including matching our resummed result to exact NLO from `Event2`. We finish this section with a brief comparison to existing OPAL data, taking into account non-perturbative corrections obtained by means of Monte Carlo simulations.

4.4.1 Fixed-order validation

The `Event2` generator provides exact results for the multiplicity in $e^+e^- \to Z \to q\bar{q}$ Born-level events up to $\mathcal{O}(\alpha_s^2)$:

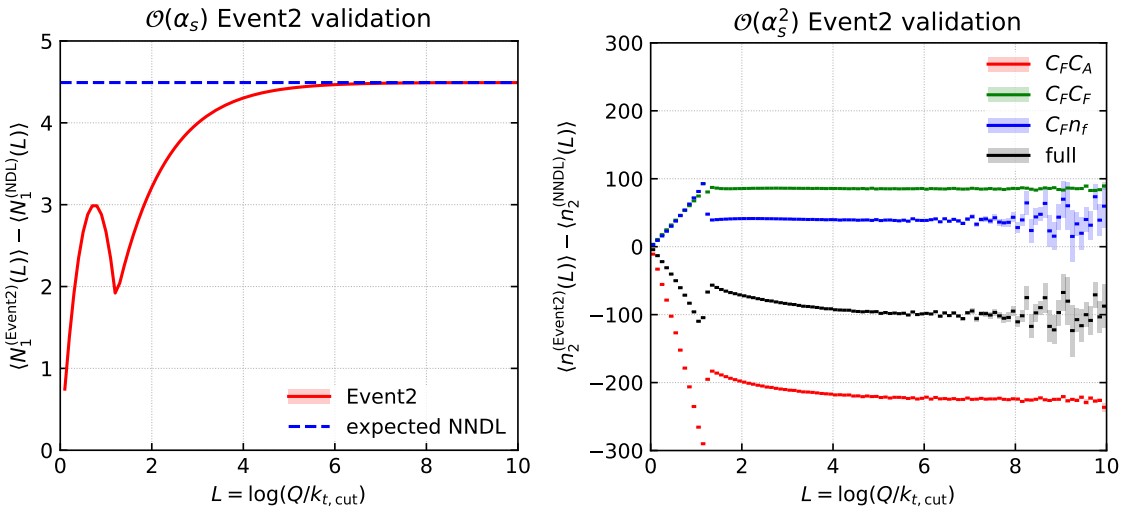
$$\langle N^{(\text{Lund})}(\alpha_s, L)\rangle = 2 + \frac{\alpha_s}{2\pi}\langle N_1^{(\text{Lund})}(L)\rangle + \left(\frac{\alpha_s}{2\pi}\right)^2 \langle N_2^{(\text{Lund})}(L)\rangle + \mathcal{O}(\alpha_s^3). \quad (4.4.1)$$

The fixed-order coefficients have the following dependence on L:

$$\frac{1}{2\pi}\langle N_1^{(\text{Lund})}(L)\rangle = h_{11}L^2 + h_{21}L + h_{31} + \mathcal{O}(e^{-L}), \quad (4.4.2a)$$

$$\frac{1}{(2\pi)^2}\langle N_2^{(\text{Lund})}(L)\rangle = h_{12}L^4 + h_{22}L^3 + h_{32}L^2 + h_{42}L + h_{52} + \mathcal{O}(e^{-L}), \quad (4.4.2b)$$

where the h_{ij} coefficients correspond to the j-th order α_s expansion of the h_i resummed expressions, e.g. h_{11} is the first-order expansion of the DL h_1 function,



(a) $\langle N\rangle$ test at $\mathcal{O}(\alpha_s)$ **(b)** $\langle n\rangle$ test at $\mathcal{O}(\alpha_s^2)$

Figure 4.7: Comparison between the NNDL calculation expanded in series of α_s and exact fixed-order results obtained numerically with `Event2`: (a) the multiplicity difference $\langle N_1^{(\texttt{Event2})}\rangle - \langle N_1^{(\text{NDL})}\rangle$ at order α_s, expected to tend to the NNDL constant represented by the dashed (blue) line, cf. Eq. (4.4.2a); (b) the differential multiplicity difference $\langle n_2^{(\texttt{Event2})}\rangle - \langle n_2^{(\text{NNDL})}\rangle$ at order α_s^2 which is expected to go to a (N^3DL) constant if the results agree at NNDL, cf. Eq. (4.4.2b).

h_{32} is the second-order expansion of the NNDL h_3 function and so on. The extraction of the α_s and $\alpha_s^2 L^2$ contributions from `Event2` therefore provides a validation of the NNDL resummed calculation. More specifically, from the results in Secs. 4.2 and 4.3, we find

$$h_{11} = \frac{2C_F}{\pi}, \qquad h_{12} = \frac{C_F C_A}{3\pi^2} \tag{4.4.3a}$$

$$h_{21} = \frac{4C_F}{\pi} B_q, \qquad h_{22} = \frac{8\beta_0 C_F}{3\pi} + \frac{4C_A C_F}{3\pi^2}\left(B_q + B_{gg} + B_{gq}\right) \tag{4.4.3b}$$

$$h_{31} = \frac{1}{\pi}\left(D^{qqg}_{\text{hme}} + D^{q\to qg}_{\text{end}}\right), \tag{4.4.3c}$$

$$\begin{aligned} h_{32} = {} & \frac{C_A}{\pi^2} D^{qqg}_{\text{hme}} + \frac{C_F}{\pi^2}\Big(D^{g\to gg}_{\text{end}} + D^{g\to q\bar{q}}_{\text{end}} + K + D^{gg}_{\text{pair}} + D^{q\bar{q}}_{\text{pair}} + D^{q}_{\text{e-loss}} \\ & + C_F D^{(\text{prim})}_{\text{clust}} + C_A D^{(\text{sec})}_{\text{clust}}\Big) + \frac{4C_F C_A}{\pi^2} B_q\left(B_{gg} + B_{gq}\right) + \frac{4C_F}{\pi} B_q \beta_0. \end{aligned} \tag{4.4.3d}$$

In order to check that these coefficients are indeed correct, we have performed two tests, shown in Fig. 4.7. First, focusing on the first order in α_s, we subtract from the `Event2` multiplicity $\langle N_1^{(\texttt{Event2})}\rangle$ the NDL expectation, $\langle N_1^{(\text{NDL})}\rangle$. This is plotted as the solid (red) line in Fig. 4.7a. Our NNDL expectation is that it should tend

asymptotically to $2\pi h_{31}$, plotted as the dashed (blue) line in Fig. 4.7a. The solid curve indeed matches the dashed one at large L as expected.

Next, focusing on the second order, $\mathcal{O}(\alpha_s^2)$, we subtract from the *differential* `Event2` multiplicity distribution, $\langle n_2^{(\texttt{Event2})} \rangle$, the NNDL expectation, $\langle n_2^{(\text{NNDL})} \rangle$, obtained through a simple derivative of our NNDL result. This is plotted in Fig. 4.7b for both the full multiplicity and for the contributions of each colour channel. The expectation is that the NNDL-subtracted result tends to a constant (associated with h_{42} in Eq. (4.4.2b)) at large L, which it does. Similar tests, reported in Appendix A.3 of Ref. [2], have been performed for the Cambridge multiplicity.

These two tests show that the NNDL calculation is correct, at least up to order α_s^2 for $e^+e^- \to Z \to q\bar{q}$ events. If the tools become available, it would be interesting to extend these tests to $e^+e^- \to H \to gg$ events, as well as one order higher in α_s. This would for example allow one to probe the NNDL contributions starting at $\mathcal{O}(\alpha_s^2)$ beyond their first non-trivial contribution, as well as probing the NNDL coefficients which start only at $\mathcal{O}(\alpha_s^3)$, such as the β_0^2 correction or the vanishing of the contribution from three emissions at commensurate angles.

4.4.2 Matching with fixed-order

In order to produce reliable phenomenological predictions of the Lund multiplicity in $e^+e^- \to Z$ events for all values of $L = \ln(Q/k_{t,\text{cut}})$, the resummed distribution obtained in Sec. 4.3, relevant at large L, needs to be matched with a fixed-order calculation, relevant at small L. For this observable, we adopt an additive matching scheme:

$$\langle N^{(\text{Lund})} \rangle_{\text{match}} = \langle N^{(\text{Lund})} \rangle_{\text{fo}} + \langle N^{(\text{Lund})} \rangle_{\text{resum}} - \langle N^{(\text{Lund})} \rangle_{\text{resum,fo}}, \tag{4.4.4}$$

where $\langle N^{(\text{Lund})} \rangle_{\text{fo}}$ is the exact fixed-order result obtained with `Event2` as described in Sec. 4.4.1, Eq. (4.4.1), taken here at NLO with respect to the $e^+e^- \to 3\,\text{jets}$ process, i.e. at order α_s^2 with respect to the $e^+e^- \to 2\,\text{jets}$ process, $\langle N^{(\text{Lund})} \rangle_{\text{resum}}$ is the NNDL-accurate resummed result, Eq. (4.3.70), and $\langle N^{(\text{Lund})} \rangle_{\text{resum,fo}}$ avoids double

counting by subtracting the $\mathcal{O}(\alpha_s^2)$ expansion of the resummed result $\langle N^{(\text{Lund})}\rangle_{\text{resum}}$

$$\langle N^{(\text{Lund})}\rangle_{\text{resum,fo}} = 2 + \alpha_s\left[h_{11}L^2 + h_{21}L + h_{31}\right] + \alpha_s^2\left[h_{12}L^4 + h_{22}L^3 + h_{32}L^2\right], \tag{4.4.5}$$

where the h_{ij} factors were defined in Eq. (4.4.3). At our accuracy, the fixed-order distribution can be normalised to the NLO inclusive cross-section, $\sigma_0 + \sigma_1 = \sigma_0(1 + \alpha_s/\pi)$. The scale uncertainty is probed by varying the renormalisation scale and the resummation scale. For this, we introduce two dimensionless parameters, x_R and x_L. The renormalisation scale is taken as $\mu_R = x_R Q$, both in the resummation and in the fixed-order results, and the resummation scale is varied by redefining L as $\ln(x_L Q/k_t)$. When varying x_R and x_L, one must introduce counter-terms to preserve the perturbative accuracy, both at fixed order and for the resummed result. For the resummed result, we get

$$\begin{aligned}\langle N^{(\text{Lund})}\rangle_{\text{resum}} = {} & h_1(\xi) + \sqrt{\alpha_s}\Big[h_2(\xi) - 2\ln x_L\sqrt{\xi}\,h_1'(\xi)\Big] \\ & + \alpha_s\Big[h_3(\xi) + (2\beta_0\ln x_R\,\xi + \ln^2 x_L)h_1'(\xi) \\ & \quad + 2\ln^2 x_L\,\xi\,h_1''(\xi) - 2\ln x_L\sqrt{\xi}\,h_2'(\xi)\Big],\end{aligned} \tag{4.4.6}$$

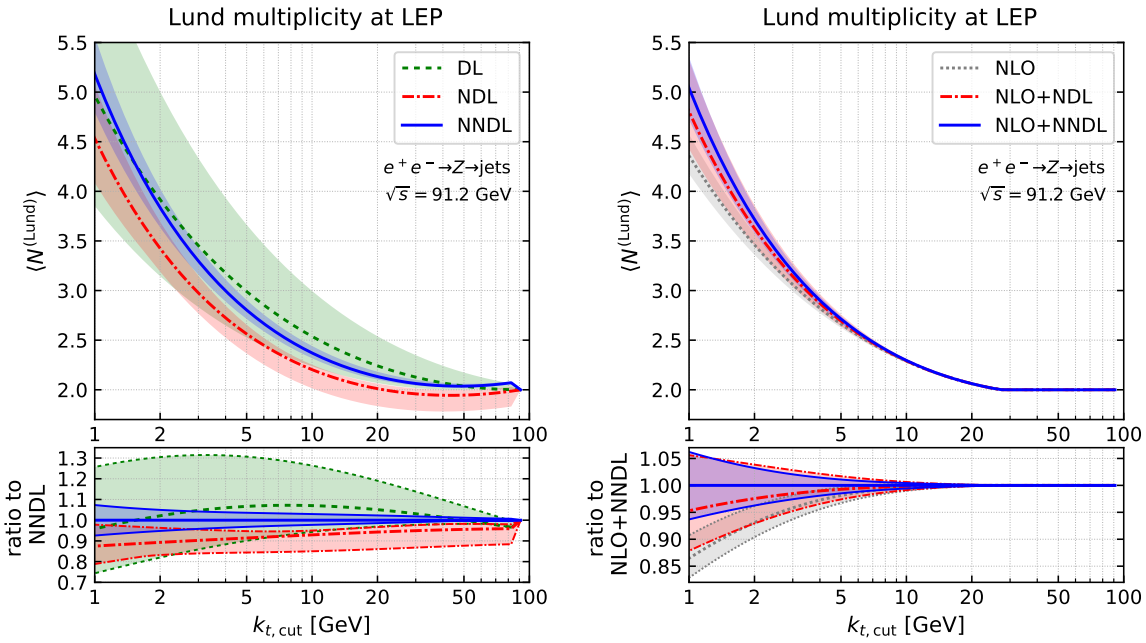
with h_i defined in Sec. 4.3.5, $\alpha_s \equiv \alpha_s(\mu_R = x_R Q)$, $\xi = \alpha_s L^2 = \alpha_s \ln^2(x_L Q/k_t)$, and h_i', h_i'' the first and second derivatives of h_i with respect to ξ. In practice, we estimate the scale uncertainty by separately varying either x_L or x_R between 1/2 and 2, taking the envelopes of the variations, and summing in quadrature the renormalisation and resummation uncertainties.

Finally, to account for the fact that the endpoints of the resummed and fixed-order distributions do not coincide, we redefine the L in the argument of $\langle N^{(\text{Lund})}\rangle_{\text{resum}}$ according to [34]

$$L = \ln\frac{Q}{k_{t,\text{cut}}} \to L = \ln\left(\frac{x_L Q}{k_{t,\text{cut}}} - \frac{x_L Q}{k_{t,\text{max}}} + 1\right), \tag{4.4.7}$$

with $k_{t,\text{max}}$ the smallest k_t value at which the fixed-order distribution is equal to its Born-level value, i.e. 2.[18] At large L, this replacement only generates power corrections in $k_{t,\text{cut}}$ and so does not spoil the logarithmic accuracy.

[18] At $\mathcal{O}(\alpha_s)$, we find $k_{t,\text{max}}^2 = \frac{5\sqrt{5}-11}{2}Q^2 \approx 0.0902\,Q^2$ ($\ln Q/k_{t,\text{max}} \approx 1.203$). At $\mathcal{O}(\alpha_s^2)$ we determine $k_{t,\text{max}}$ numerically from the `Event2` distribution, finding $k_{t,\text{max}}^2 \approx 0.1062\,Q^2$, i.e. $\ln Q/k_{t,\text{max}} \approx 1.121$.



(a) **(b)**

Figure 4.8: Left: Resummed Lund multiplicity at DL (dashed, green), NDL (dash-dotted, red) and NNDL (solid, blue) as a function of $k_{t,\mathrm{cut}}$ for LEP kinematics. Right: Lund multiplicity after matching with NLO. The pure NLO result is shown in dotted (grey) for reference, together with matched NLO+NDL (dash-dotted, red) and NLO+NNDL (solid, blue). The bottom panels display the ratio to the most accurate result (NNDL on the left and NLO+NNDL on the right).

Fig. 4.8 shows the Lund multiplicity, together with its uncertainty, as a function of $k_{t,\mathrm{cut}}$ for LEP $e^+e^- \to Z$ events at $\sqrt{s} = 91.2$ GeV. A common feature to all curves is that the Lund multiplicity increases significantly when $k_{t,\mathrm{cut}}$ decreases. In Fig. 4.8a, we focus on the resummed results at different degrees of logarithmic accuracy. We find that while NDL corrections reduce the multiplicity, NNDL corrections cause a non-negligible increase, as one would expect from Fig. 4.6. Furthermore, increasing the logarithmic accuracy significantly reduces the perturbative uncertainty. Working for example at $k_{t,\mathrm{cut}} = 5$ GeV, The DL uncertainty of $\sim 20\%$ is reduced to 5.6% at NDL and to $\sim 3.4\%$ at NNDL. For $k_{t,\mathrm{cut}} = 1$ GeV, these numbers are around 27%, 11% and 7%, showing a similar reduction from NDL (the current state-of-the-art) to NNDL. The NNDL uncertainty band is also more symmetric than the NDL one. It is also interesting to notice that the NDL and NNDL uncertainty bands only barely overlap.

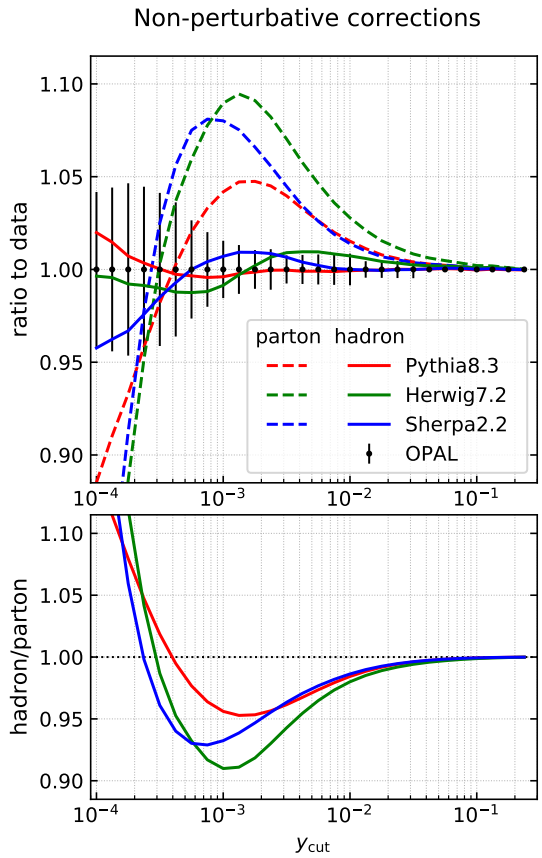
Fig. 4.8b shows the effect of matching with NLO ($\mathcal{O}(\alpha_s^2)$) fixed-order results. We first see that the effect of the resummation is to increase the average Lund multiplicity, even further so with NNDL matching than with NDL matching, showing the necessity for the resummation at small $k_{t,\text{cut}}$. Besides the sheer increase in multiplicity, NLO+NNDL matched results also bring a significant reduction in scale uncertainty compared to what is observed at NLO+NDL. This reduction is of about 50% at almost all $k_{t,\text{cut}}$ values, e.g. going from $\sim 9\%$ (2%) to $\sim 6\%$ (1.3%) at $k_{t,\text{cut}} = 1$ GeV (5 GeV).

4.4.3 Comparison to LEP data

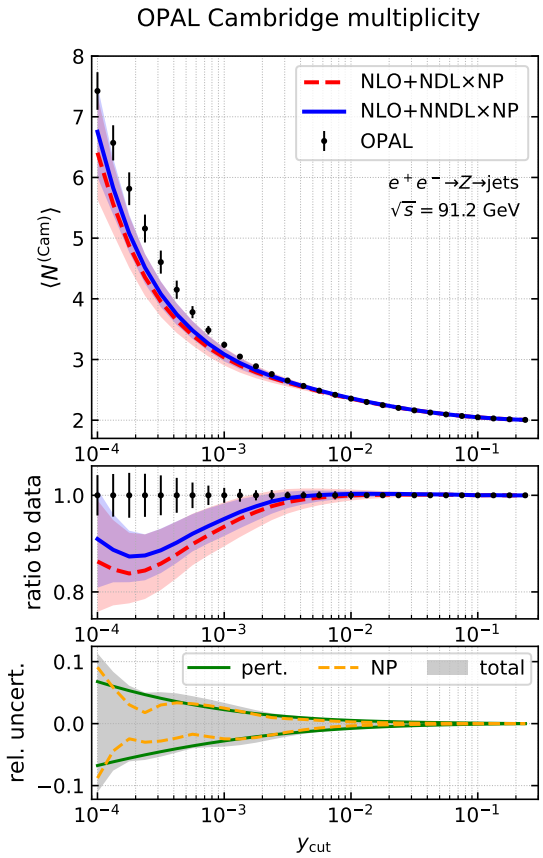
We conclude this section with a short comparison between our analytic results and the existing measurement [75] by the OPAL collaboration at LEP. Here, we focus solely on the results for $\sqrt{s} = 91.2$ GeV.

From the viewpoint of perturbative QCD, the same approach we just discussed for the Lund multiplicity can be applied to the Cambridge multiplicity: the NNDL resummed result, Eq. (4.3.79), can be matched to `Event2` exact NLO multiplicities using additive matching, Eq. (4.4.4). For a phenomenological comparison to the LEP data, we need to supplement the perturbative result by non-perturbative corrections. For this brief study, we extract these from standard general-purpose Monte Carlo generators. Namely, we run Pythia(v8.306) [76], Herwig(v7.2.0) [77, 78], and Sherpa(v2.2.11) [42, 79] each at parton level and hadron level separately. This is plotted on the top panel of Fig. 4.9a showing that hadron-level predictions for the three generators do reproduce the data, although their respective parton-level distributions are quite different. Hadronisation corrections (and uncertainties) are then taken as the average (and envelope) of the three ratios of hadron- to parton-level distributions, cf. the lower panel of Fig. 4.9a.

The non-perturbative corrections are applied as a multiplicative factor to the matched perturbative results. The uncertainty is obtained by adding the perturbative and non-perturbative uncertainties in quadrature. The resulting distributions are shown in Fig. 4.9b for the NDL and NNDL resummations. Globally



(a) Comparison of the data to standard Monte Carlo generators at parton (dashed) and hadron (solid) levels.



(b) Comparison of the data to NDL (red) and NNDL (blue) resummed results matched to NLO and corrected for non-perturbative effects.

Figure 4.9: Comparison of Monte Carlo (left) and analytic (right) results to the existing average Cambridge jet multiplicity measurement [75] from the OPAL collaboration at LEP.

speaking, we see a decent degree of agreement with the OPAL data, although the predictions are systematically below the data for $y_{\text{cut}} \lesssim 10^{-3}$, i.e. for $k_{t,\text{cut}} \lesssim 3$ GeV. Including the NNDL corrections shows both an increase in multiplicity, bringing the predictions closer to the data, and a reduction in uncertainty. This agrees with the observations made in the previous subsection. We note as well that for the matched NNDL results, the perturbative and non-perturbative uncertainties are of the same order for $y_{\text{cut}} \lesssim 0.002$ with the perturbative uncertainties marginally dominating at larger values.

From a phenomenological viewpoint, the significant reduction of the perturbative uncertainties at NNDL compared to NDL, seen both in this section and in the

previous one, is the most important phenomenological result of this chapter. It suggests that it would be interesting to perform a more extensive comparison to the OPAL data. Such a study could include matching to exact NNLO results, as well as an improved resummation of the running-coupling corrections (see the discussion at the end of Sec. 4.3.5). These would hopefully further reduce the perturbative uncertainty and produce a better agreement with the data at low values of $k_{t,\mathrm{cut}}$. This could then potentially serve as a way to make an additional extraction of the strong coupling constant α_s. It would also be of interest to measure the average Lund multiplicity as a function of $k_{t,\mathrm{cut}}$ — or the difference between the Lund and Cambridge multiplicities —, especially in the context of the renewed interest in the community for the analysis of archived ALEPH data to study new observables (see e.g. [80]) or phenomena (see e.g. [81]). From a theoretical viewpoint, one could expect that higher-order running-coupling corrections would also increase the multiplicity at small y_{cut}, reemphasising the interest already stated in Sec. 4.3.5.

5

Lund multiplicity in *pp* collisions

Having computed the average Lund multiplicity in e^+e^- collisions, we now move on to the case of *pp* collisions. Extending this definition to *pp* colliders adds to the rich Lund-plane-based phenomenology at the LHC [33, 82–85] by introducing an observable capable of probing the full Lund diagram. In a more generic context, experimental measurements of the number of charged particles within a jet [86, 87] and of the number of subjets inside groomed jets [88] have revealed sizeable discrepancies between Monte Carlo event generators. A high-precision calculation of a multiplicity-based observable can therefore help clarifying this situation. Resolving these discrepancies can then result in a better determination of the jet energy scale [89], a key quantity in any jet analysis at the LHC. Therefore, besides their intrinsic theoretical interest, the results presented in this chapter have the potential to serve as benchmarks to test and develop parton shower event generators.

In this chapter, we first extend the Lund multiplicity procedure established in Sec. 4.1 to the context of high-energy jets produced in *pp* collisions and then proceed with its resummation. This computation will bring three types of complications with respect to the e^+e^- case, which we will need to account for: 1) due to the finite radius of jets in *pp* collisions, large-angle soft effects will need to be recomputed, 2) while the centre-of-mass energy of the collision system is fixed in e^+e^- collisions, jets produced in *pp* collisions follow a $p_\perp$ spectrum associated with the underlying

hard process, and, 3) jets are initiated via an admixture of hard quarks q or gluons g which have differing multiplicities.

This chapter is organised as follows. In Sec. 5.1 we define the Lund multiplicity algorithm for high-energy jets. Then, we compute its resummation up to NNDL accuracy in Sec. 5.2. We supplement the resummed calculation with a matching to the exact $\mathcal{O}(\alpha_s^2)$ result and a study of its sensitivity to non-perturbative corrections in Sec. 5.3. The final phenomenological predictions for LHC energies can be found in Sec. 5.3.2.

5.1 Lund multiplicity algorithm in pp collisions

We generalise the Lund-multiplicity definition from Sec. 4.1 so as to count the number of subjets inside high-energy jets. As with any other Lund-plane-based observable, the procedure begins with reclustering a jet of interest at a high-energy collider with the Cambridge/Aachen algorithm [29, 30].[1] Then, its Lund multiplicity is defined as follows:

1. Set $N^{(\text{Lund})} = 1$.
2. Undo the last clustering step to get two subjets j_1 and j_2, with j_1 the harder branch, i.e. $p_{\perp 1} > p_{\perp 2}$.
3. Calculate the relative transverse momentum of the splitting as

$$k_t \equiv \min(p_{\perp 1}, p_{\perp 2})\Delta_{12} \qquad \text{where} \qquad \Delta_{12}^2 = (y_1 - y_2)^2 + (\phi_1 - \phi_2)^2, \quad (5.1.1)$$

   with $y_{1,2}$ ($\phi_{1,2}$) the rapidities (azimuthal angles) of the subjets with respect to the beam.
4. If $k_t \geq k_{t,\text{cut}}$ the splitting contributes to the Lund multiplicity, i.e. $N^{(\text{Lund})}$ is incremented by one, and we go back to step 2 for *each* of the two subjets.
5. Otherwise, if $k_t < k_{t,\text{cut}}$, repeat from step 2 following only the harder subjet j_1.

[1] We note that using a different recombination scheme from the E-scheme, see Sec. 2.2.1, for the Cambridge/Aachen reclustering procedure, such as the winner-takes-all [62] recombination scheme, again only brings differences beyond our target NNDL accuracy as discussed in App. A.2.

The procedure terminates when there is nothing left to decluster. The result of the above algorithm is one plus the total number of emissions in both the primary Lund plane and subsidiary Lund leaves whose transverse momentum is above $k_{t,\text{cut}}$. Naturally, the average Lund multiplicity in a high-energy jet follows the resummation structure of Eq. (2.3.6). The main complication compared to the earlier calculation of the Lund multiplicity in e^+e^- events comes from a richer structure of large-angle gluon radiation. In this context, the treatment of gluon radiation at large angles is known to be prohibitively complex if one wants to retain full-colour accuracy. Going forward we will thus target full-colour accuracy for the first large-angle emission but limit ourselves to a leading-colour prescription for subsequent large-angle emissions.

5.2 Calculation of the average Lund multiplicity in jets

In this section, we derive the main result of this chapter, namely we extend the calculation of the Lund multiplicity to the case of the subjet multiplicity within a high-energy jet. To avoid confusion, we will throughout use the subscript '$\perp$' for transverse momenta defined with respect to the beam, and 't' for relative Lund declustering momenta.

We therefore start with a jet of transverse momentum $p_\perp$, and rapidity y_jet, assuming that it has been reconstructed using the anti-k_t jet algorithm [31] with a jet radius R, as introduced in Sec. 2.2.1.4. The average Lund multiplicity $\langle N_\text{jet}^{(\text{Lund})}(\alpha_s; L)\rangle$ above a relative transverse momentum cut, $k_{t,\text{cut}}$, follows the logarithmic expansion of Eq. (2.3.6) with the logarithm L defined as $L \equiv L_\text{jet} = \ln(p_\perp R/k_{t,\text{cut}})$. In practical applications, the transverse momentum and rapidity of the jet will not be fixed but integrated over a fiducial phase space. We discuss how to translate our results for a fixed jet $p_\perp$ and y_jet to a realistic scenario in Sec. 5.2.5.

A large fraction of the calculation can simply be recycled from the e^+e^- results presented in Chap. 4 with $L = L_\text{jet}$. Indeed, due to the great overlap between the e^+e^-- and pp-Lund multiplicity procedures in the collinear limit, all the contributions involving only collinear physics (including running-coupling corrections) can be

reused as a consequence of the universality of the collinear limit of QCD, Sec. 2.1.3. We are therefore left with the computation of the contributions depending on emissions at large angles (commensurate with the jet radius). In general, these corrections depend on the overall structure of the hard process. In practice, we will consider jets in either Z+jet or inclusive jet samples. However, we will keep the discussion below as generic as possible so as to facilitate possible future extensions to other processes.

The e^+e^- results in Sec. 4.3.5 have been presented separately for quark and gluon hemispheres. In a pp context, jets can also be considered as quark- or gluon-initiated (as given by the Born-level hard process) as long as we are only interested in the contributions involving either soft gluon emissions and/or collinear branchings. More concretely, these contributions include the collinear contributions recycled from our e^+e^- results, as well as new large-angle contributions which only depend on soft-gluon emissions. For these contributions we can consider that we work with a jet of a given flavour, and ultimately get the total multiplicity by weighting the quark- and gluon-initiated jet multiplicities by the corresponding Born-level fractions. Up to our target NNDL accuracy, the only contribution where the quark/gluon separation is not obvious is the case of hard matrix-element corrections, sensitive to emissions which are both hard and large-angle. We address this case in Sec. 5.2.3.1.

As in Chap. 4, we start with the DL expressions and then proceed with the calculation of the NDL and NNDL corrections.

5.2.1 DL accuracy

Since the DL Lund multiplicity only involves soft-and-collinear emissions, the results for $h_1^{(q,g)}$ for quark and gluon jets can be taken directly from the corresponding results in e^+e^- events, i.e. Eq. (4.2.10). The DL average Lund multiplicity for a given hard process is thus given by

$$h_1(\xi) = f_q h_1^{(q)}(\xi) + f_g h_1^{(g)}(\xi), \tag{5.2.1}$$

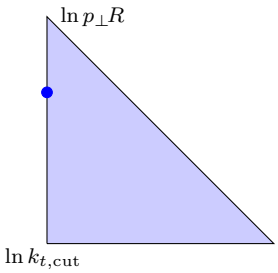


Figure 5.1: Lund representation of the only new NDL contribution for high-energy jets: a large-angle emission.

with

$$f_i = \frac{\sigma_i}{\sigma_q + \sigma_g}, \quad \text{and} \quad \xi = \alpha_s L^2, \tag{5.2.2}$$

where the quark/gluon fractions $f_{q,g}$ are computed from the Born-level cross-sections $\sigma_{q,g}$.

5.2.2 NDL accuracy

NDL corrections arise from a series of branchings where a single emission gives a single-logarithmic contribution (proportional to $\alpha_s L$) and all other emissions are soft-and-collinear (proportional to $\alpha_s L^2$). The two contributions which appear in the e^+e^- case, namely the running coupling (cf. Fig. 4.2a) and hard-collinear (cf. Fig. 4.2b) correction are unchanged in the case of the Lund multiplicity in a jet. The only potential new source of NDL corrections is the case of an emission at large angles, close to the jet boundary as depicted in Fig. 5.1. Including the proper relative weight of quark- and gluon-initiated jets, we therefore write

$$h_2(\xi) = f_q h^{(q)}_{2,\mathrm{coll}}(\xi) + f_g h^{(g)}_{2,\mathrm{coll}}(\xi) + h_{2,\mathrm{la}}(\xi), \tag{5.2.3}$$

where the $h^{(q,g)}_{2,\mathrm{coll}}$ functions were defined in Eq. (4.3.72). While $h_{2,\mathrm{la}}$ vanished in e^+e^- collisions (see Sec. 4.2.2), that is no longer the case for high-energy jets and we compute this contribution below.

Generically, the radiation of a large-angle gluon depends on the overall structure of the Born event. Since the gluon is soft, it is however still possible to separate the contribution from quark- and gluon- initiated jets based on the underlying Born

hard process. We thus write $h_{2,\text{la}} = f_q h^{(q)}_{2,\text{la}} + f_g h^{(g)}_{2,\text{la}}$. These contributions would nevertheless be hard-process-dependent, i.e. a "gluon" jet in a Z+jet event would be different from a "gluon" jet in an inclusive jet sample. We proceed by writing the Born hard process as a sum over different partonic flavour channels:

$$\sigma^{(i)} = \sum_{\substack{\mathcal{C}\in\text{flavour}\\ \text{channels}}} \sigma^{(i)}_{\mathcal{C}}, \tag{5.2.4}$$

where the (optional) flavour superscript, i, limits the sum to channels contributing to a specific jet flavour.

We start by considering the $\mathcal{O}(\alpha_s)$ contribution to the Lund multiplicity where a single soft gluon is emitted. For a given channel, the matrix element describing such an emission can be further decomposed into a sum over coloured dipoles (ab), similar to that of Eq. (2.1.14), with a and b two (incoming or outgoing) partons in the Born process:

$$\sum_{a,b\in\text{legs}} \frac{\alpha_s}{2\pi}\omega^{\mathcal{C}}_{ab} \int k_\perp \mathrm{d}k_\perp \int \mathrm{d}y \int \frac{\mathrm{d}\phi}{2\pi}(k|ab), \quad \text{with} \quad (k|ab) = \frac{(p_a\cdot p_b)}{(p_a\cdot k)(k\cdot p_b)}, \tag{5.2.5}$$

and $\omega^{\mathcal{C}}_{ab}$ is a kinematic weight which, in general, depends on the kinematics of the full hard event. Therefore, the NDL correction to the Lund multiplicity associated with the radiation of a soft large-angle gluon takes the form

$$\delta N^{(\text{NDL},i)}_{\text{la}} = \sqrt{\alpha_s} h^{(i)}_{2,\text{la}}(\xi) = \sum_{\substack{\mathcal{C}\in\text{flavour}\\ \text{channels}}} \frac{\sigma^{(i)}_{\mathcal{C}}}{\sigma^{(i)}} \sum_{(ab)\in\text{event}} \delta N^{(\text{NDL})}_{\mathcal{C},(ab)}, \tag{5.2.6}$$

where $\delta N^{(\text{NDL})}_{\mathcal{C},(ab)}$ is the correction to the multiplicity due to a soft gluon emitted close to the jet boundary from a dipole (ab). At the first non-trivial order in α_s, it is given by

$$\delta N^{(\text{NDL})}_{\mathcal{C},(ab),\mathcal{O}(\alpha_s)} = \frac{\alpha_s}{\pi}\omega^{\mathcal{C}}_{ab} \int_0^{p_\perp} \frac{\mathrm{d}k_\perp}{k_\perp} \mathrm{d}y \frac{\mathrm{d}\phi}{2\pi} \left[\frac{k_\perp^2}{2}(k|ab) - \frac{1}{\Delta_k^2}\delta_{a \text{ or } b=\text{jet}}\right] \times \Theta(k_t > k_{t,\text{cut}})\,\Theta(\Delta_k < R). \tag{5.2.7}$$

In this expression, the second term in the square bracket subtracts the collinear (DL) contribution and the "δ" selects the cases where one of the two dipole legs corresponds to the jet under consideration. This is done so as to isolate the NDL correction.

Also, $\Delta_k^2 = (y - y_{\text{jet}})^2 + (\phi - \phi_{\text{jet}})^2$ is the (squared) distance between the jet axis and the emission. To evaluate (5.2.7), we first make a change of variable from $k_\perp$ to $k_t = k_\perp \Delta_k$. Including the constraint that k_t has to be above $k_{t,\text{cut}}$ we can then write

$$\int_{k_{t,\text{cut}}}^{p_\perp \Delta_k} \frac{\mathrm{d}k_t}{k_t} = L + \mathcal{O}(\text{NNDL}), \tag{5.2.8}$$

where only the logarithmically-enhanced term contributes at NDL. This is allowed because the angular integration does not contain any collinearly-enhanced contribution so that Δ_k is of order R up to a constant factor, which would not generate a logarithmic enhancement. We are then left with the integration over the geometric variables y and ϕ so that the NDL correction takes the form

$$\delta N^{(\text{NDL})}_{\mathcal{C},(ab),\mathcal{O}(\alpha_s)} = \frac{\alpha_s}{\pi} L\, \omega^{\mathcal{C}}_{ab} D^{\text{la}}_{ab}. \tag{5.2.9}$$

We now compute the coefficients D^{la}_{ab} for a generic $2 \to 2$ process. Let us denote the four-momenta of the incoming partons as p_1 and p_2, and those of the outgoing jet (for which one measures the multiplicity) and recoiling parton as p_j and p_r.[2] Without loss of generality, we can parametrise the momenta of the hard legs and the radiated gluon, k, as follows (using a (E, p_x, p_y, p_z) convention):

$$p_1 \equiv p_\perp \cosh\hat{y}\,(1,0,0,1), \tag{5.2.10a}$$

$$p_2 \equiv p_\perp \cosh\hat{y}\,(1,0,0,-1), \tag{5.2.10b}$$

$$p_j \equiv p_\perp\,(\cosh\hat{y},1,0,\sinh\hat{y}), \tag{5.2.10c}$$

$$p_r \equiv p_\perp\,(\cosh\hat{y},-1,0,-\sinh\hat{y}), \tag{5.2.10d}$$

$$k \equiv k_\perp\,(\cosh y,\cos\phi,\sin\phi,\sinh y), \tag{5.2.10e}$$

where $p_\perp$ is the transverse momentum of the jet, $\hat{y}$ is the rapidity of the jet in the partonic centre-of-mass frame,[3] $k_\perp \ll p_\perp$, and we have picked the jet azimuthal angle to be zero. The soft gluon can be emitted from any of the 6 possible colour dipoles: (p_1,p_2), (p_1,p_j), (p_2,p_j), (p_1,p_r), (p_2,p_r) and (p_j,p_r). Except for the (12)

[2] In the case of Z+jet events the recoiling object is the colour singlet Z so that p_r does not contribute to the coloured dipoles.

[3] In the lab frame, $y_{\text{jet}} = \hat{y} + \frac{1}{2}\ln\frac{x_1}{x_2}$ with $x_{1,2}$ the longitudinal momentum fractions of the incoming partons.

dipole, the integrals in Eq. (5.2.7) cannot be computed exactly analytically. We thus make a series expansion in the jet radius R and find [83]

$$D_{12}^{\text{la}} = \frac{R^2}{2}, \tag{5.2.11a}$$

$$D_{1j}^{\text{la}} = \frac{R^2}{8} + \frac{R^4}{576} + \mathcal{O}(R^8), \tag{5.2.11b}$$

$$D_{jr}^{\text{la}} = \frac{\tanh^2 \hat{y}}{8} R^2 + \frac{(\cosh^2 \hat{y} - 3)^2}{576 \cosh^4 \hat{y}} R^4 + \frac{\tanh^2 \hat{y}}{384} R^6 + \mathcal{O}(R^8), \tag{5.2.11c}$$

$$D_{1r}^{\text{la}} = \frac{e^{2\hat{y}}}{8 \cosh^2 \hat{y}} R^2 + \frac{1}{64 \cosh^4 \hat{y}} R^4 + \frac{\tanh^2 \hat{y}}{384 \cosh^4 \hat{y}} R^6 + \mathcal{O}(R^8). \tag{5.2.11d}$$

Then, $D_{2j}^{\text{la}} = D_{1j}^{\text{la}}$ and D_{2r}^{la} is obtained from D_{1r}^{la} taking $\hat{y} \to -\hat{y}$. One notices that the $(1r)$ dipole tends to the (12) dipole when $\hat{y} \to \infty$ and to 0 when $\hat{y} \to -\infty$. Similarly, the (jr) dipole is symmetric under $\hat{y} \to -\hat{y}$ and converges to the $(1j)$ dipole at large $\hat{y}$. Dipoles involving the recoiling parton depend on the kinematics of the $2 \to 2$ process via $\hat{y}$. This will have to be taken into account when considering jets within a rapidity range (see Sec. 5.2.5). In practice, it has been checked numerically that the small-R expansion used in Eq. (5.2.11) reproduces the exact result to well within 1% up to $R = 1$, and up to deviations of at most 0.3% for $R = 0.8$ which we use as a default below [3].

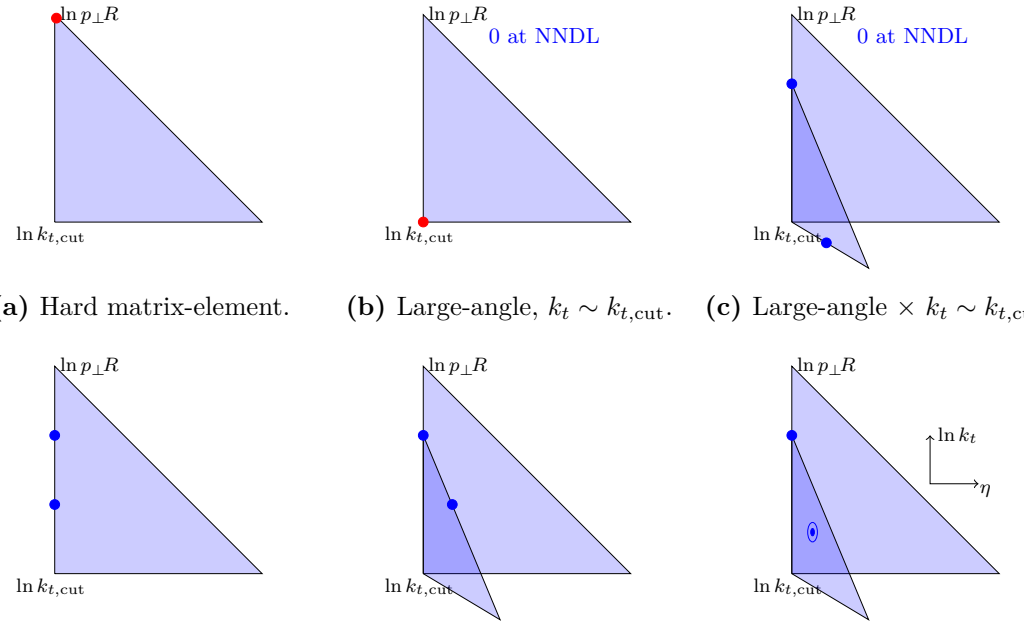
At all orders, one should include the extra contribution to the multiplicity due to subsequent soft-and-collinear radiation from the large-angle gluon. Using Eq. (4.2.15), we find that ($\nu = \sqrt{\bar{\alpha} L^2}$)

$$\delta N_{\mathcal{C},(ab)}^{(\text{NDL})} = \frac{\alpha_s}{\pi} \omega_{ab}^{\mathcal{C}} D_{ab}^{\text{la}} \int_0^L d\ell \, N_g^{(\text{DL})}(L - \ell) = \sqrt{\frac{\alpha_s}{2 C_A \pi}} \, \omega_{ab}^{\mathcal{C}} D_{ab}^{\text{la}} \sinh \nu. \tag{5.2.12}$$

To compute the NDL multiplicity for a given hard process, one should also specify its corresponding weights $\omega_{ab}^{\mathcal{C}}$. In the case of Z+jet events there are only two partonic channels, one corresponding to quark jets and the other to gluon jets. Since there are only three coloured partons (two incoming and one outgoing), the colour algebra for each channel is straightforward and the $\omega_{ab}^{\mathcal{C}}$ weights are listed in Tab. 5.1. The situation is more involved for dijet events due to both the increased number of partonic channels and the more intricate colour structure of the four-leg process. The corresponding $\omega_{ab}^{\mathcal{C}}$ weights can be extracted from Ref. [90] and are given in appendix A of the original publication [3].

Channel	ω_{12}	ω_{1j}	ω_{2j}
$q\bar{q} \to Zg$	$2C_F - C_A$	C_A	C_A
$qg \to Zq$	C_A	C_A	$2C_F - C_A$

Table 5.1: Kinematic weights $\omega_{ab}^{\mathcal{C}} \equiv (-2\mathbf{T}_a \cdot \mathbf{T}_b)$ for different flavour channels in Z+jet events.



(a) Hard matrix-element. **(b)** Large-angle, $k_t \sim k_{t,\text{cut}}$. **(c)** Large-angle $\times$ $k_t \sim k_{t,\text{cut}}$.

(d) Two large-angle. **(e)** Large-angle $\times$ hard-collinear. **(f)** Large-angle $\times$ running α_s.

Figure 5.2: Lund representation of the new configurations with respect to e^+e^- collisions that contribute to the multiplicity at NNDL.

5.2.3 NNDL accuracy

At NNDL accuracy, we again have to include two broad families of contributions: collinear contributions which can be obtained from the corresponding calculation in e^+e^-, namely $h_{3,\text{coll}}$ given by Eq. (4.3.75) and Eq. (4.3.78), as well as extra corrections involving large-angle emissions. The latter are depicted in Fig. 5.2 and we briefly discuss them here before proceeding with their explicit calculation in the following sections.

Following the discussion in Sec. 4.3.1, NNDL corrections can be obtained in two ways: either from one "NNDL-like" emission contributing a factor α_s (with no logarithmic enhancement) accompanied by any number of soft-and-collinear

emissions, or from two "NDL-like" emissions, each contributing a factor $\alpha_s L$, plus any number of soft-and-collinear emissions. In the first case, contributions at large angles can arise from two kinematic configurations:

- an emission at the top of the Lund plane, Fig. 5.2a, corresponding to a hard matrix-element correction, discussed in Sec. 5.2.3.1,
- or an emission at the bottom-left corner of the Lund plane, Fig. 5.2b, corresponding to an emission at large angle and close to the $k_{t,\text{cut}}$ kinematic limit. We have structured the calculation so that this contribution is zero, as discussed in Sec. 5.2.3.2.

In the second case, the first NDL-like emission must happen at large angle, and the second one can correspond to any NDL correction. The second emission can therefore be

- a collinear emission close the kinematic $k_{t,\text{cut}}$, Fig. 5.2c, which also yields a vanishing contribution as discussed in Sec. 5.2.3.2,
- another large-angle emission, Fig. 5.2d, discussed in Sec. 5.2.3.3,
- a hard-collinear branching, Fig. 5.2e, discussed in Sec. 5.2.3.4,
- or a running-coupling correction, Fig. 5.2f, discussed in Sec. 5.2.3.5.

Altogether, the NNDL function $h_3(\xi)$ for the Lund multiplicity in high-energy jets is written as[4]

$$h_3(\xi) = f_q h^{(g)}_{3,\text{coll}}(\xi) + f_g h^{(q)}_{3,\text{coll}}(\xi) + h_{3,\text{hme}}(\xi) + h_{3,\text{la}^2}(\xi) + h_{3,\text{la}\times\text{hc}}(\xi) + h_{3,\text{la}\times\text{rc}}(\xi), \tag{5.2.13}$$

where the collinear $h^{(i)}_{3,\text{coll}}(\xi)$ were defined in Eqs. (4.3.75), (4.3.78), and we discuss the calculation of the final four pieces in the following sections.

5.2.3.1 Hard matrix-element correction (top of the Lund plane)

We first consider the NNDL correction to the Lund multiplicity of a hard, wide-angle emission that arises due to the fact that the soft eikonal approximation

[4] In this expression, the quark and gluon fractions are taken from the Born-level process as in the DL and NDL sections. At NNDL accuracy, NLO corrections to the Born-level cross-sections have to be taken into account and we include them in $h_{3,\text{hme}}(\xi)$ as detailed in Sec. 5.2.3.1.

is no longer valid and the exact matrix element has to be used instead. Our starting point is the exact expression for the Lund multiplicity at NLO, i.e. $\mathcal{O}(\alpha_s)$ relative to the Born-level process

$$\langle N^{(\text{Lund})}\rangle_{\mathcal{O}(\alpha_s)} = \frac{1}{\sigma_0+\sigma_1}\left(\sigma_0 + \int \mathrm{d}\Phi|\mathcal{M}_R|^2[1+\Theta(k_t > k_{t,\text{cut}})] + \int \mathrm{d}\Phi|\mathcal{M}_V|^2\right), \tag{5.2.14}$$

where σ_0 and σ_1 are respectively the Born-level cross section and its NLO correction, and $|\mathcal{M}_{R,(V)}|$ is the real (virtual) NLO matrix-element for the process being studied. For the real contribution, we have assumed that the two partons are inside the jet under consideration. The generalisation to the case where only one parton is inside the jet is straightforward and discussed below.

The extension of Eq. (5.2.14) to all orders requires further dressing of each term with towers of DL emissions. Since this depends on the partonic flavour, one has to separate each term in (5.2.14) into flavour channels. Let us therefore assume that one can associate a suitably-defined flavour index a with the virtual contribution, and two flavour indices b and c with the two partons in the real contribution, corresponding to an $a \to bc$ splitting. For the sake of the argument, let us further assume that we can separate the real and virtual contributions into a "hard" and a "soft" piece:

$$|\mathcal{M}_R^{(bc)}|^2 = |\mathcal{M}_R^{(bc)}|^2_{\text{hard}} + |\mathcal{M}_R^{(bc)}|^2_{\text{soft}}, \tag{5.2.15}$$

$$|\mathcal{M}_V^{(a)}|^2 = |\mathcal{M}_V^{(a)}|^2_{\text{hard}} + |\mathcal{M}_V^{(a)}|^2_{\text{soft}}. \tag{5.2.16}$$

For the real contribution, one can define $|\mathcal{M}_R^{(bc)}|^2_{\text{soft}}$ so that it contains the soft and/or collinear divergences, which reproduce the contributions to the multiplicity not associated with hard-wide-angle physics. This includes the DL and NDL contributions, the NNDL collinear-endpoint correction (which can be recycled from the e^+e^- result and corresponds to the terms involving the $D^{a\to bc}_{\text{end}}$ coefficients in Eqs. (4.3.75) and (4.3.78)) and potential NNDL soft-large-angle corrections (discussed in Sec. 5.2.3.2). This leaves only a non-zero $|\mathcal{M}_R^{(bc)}|^2_{\text{hard}}$ contribution at the top of the Lund plane. Such a separation is less obvious for the virtual correction, but, due to infrared safety and the KLN theorem, one can take $|\mathcal{M}_V^{(a)}|^2_{\text{soft}} = -\int \mathrm{d}\Phi_1 |\mathcal{M}_R^{(bc)}|^2_{\text{soft}}$ for an $a \to bc$ splitting, where $\mathrm{d}\Phi_1$ represent the inclusive integral

over the real-emission phase space, see Eq. (2.1.11). In practice, the NNDL hard matrix-element contribution to the multiplicity only requires the integrated cross-sections $\sigma_{R(V),\text{hard(soft)}} = \int d\Phi |\mathcal{M}_{R(V)}|^2_{\text{hard(soft)}}$.

The all-orders average multiplicity including all hard matrix-element effects can then be written as

$$\langle N^{(\text{Lund})} \rangle = \frac{1}{\sigma_0 + \sigma_1} \left\{ \sum_a \sigma_0^{(a)} N_a(L) + \sum_{bc} \sigma_{R,\text{hard}}^{(bc)} [N_b(L) + N_c(L)] + \sum_{bc} \sigma_{R,\text{soft}}^{(bc)} \delta_{a=b+c} N_a(L) + \sum_a \sigma_V^{(a)} N_a(L) \right\}. \tag{5.2.17}$$

In writing this expression, we have taken into account the fact that for the DL dressing of the real "soft" contribution, one has to define the flavour sum $a = b + c$ as a proxy for the flavour of the parent parton corresponding to the (bc) flavour pair. The exact procedure for the reconstruction the flavour of a from the daughter partons is irrelevant as long as it is correct in the soft limit.

Adding and subtracting $\sigma_{R,\text{hard}}^{(bc)} \delta_{a=b+c} N_a(L)$ to Eq. (5.2.17) we obtain

$$\langle N^{(\text{Lund})} \rangle = \frac{1}{\sigma_0 + \sigma_1} \left\{ \sum_a \sigma_0^{(a)} N_a(L) + \sum_{bc} \sigma_{R,\text{hard}}^{(bc)} [N_b(L) + N_c(L) - N_a(L)] + \sum_a \left[\sum_{bc} \sigma_R^{(bc)} \delta_{a=b+c} + \sigma_V^{(a)} \right] N_a(L) \right\}, \tag{5.2.18}$$

where each term can be determined by means of fixed-order Monte Carlo simulations which provide access to the flavours of the partons. The first term is obtained from the quark and gluon contributions to the Born-level cross section. As we have already mentioned, the second term is calculated from the real NLO correction to the cross-section. To isolate the "hard" component, we run with a small $k_{t,\text{cut}}$ and subtract the $\mathcal{O}(\alpha_s)$ contributions not associated with hard-wide-angle physics, i.e. the DL and NDL contributions as well as the collinear endpoint NNDL contribution, Fig. 4.4a. The DL-dressing factor $N_b(L) + N_c(L) - N_a(L)$ can be interpreted as if a hard parton of flavour a — which would have been dressed with a DL multiplicity $N_a(L)$ — is replaced by two hard partons b and c, dressed with DL multiplicities $N_b(L)$ and $N_c(L)$ respectively. Finally, the third term in Eq. (5.2.18) can simply be interpreted as the change in quark and gluon fractions at NLO, including both

real and virtual corrections. While the individual contributions from the second and third terms depend on the precise recipe to define the combined flavour of a flavour pair (bc), their sum is well-defined.

Let us briefly return to the question of what happens if in a $2 \to 3$ real event each of the three partons are in separate jets. In this case, the second term in Eq. (5.2.18) disappears (imagine b is in the jet, we have $a = b$ and the square bracket becomes $N_b - N_a = 0$). The last term would then just have one of b or c in the jet which corresponds to the NLO correction to the jet cross-section.

We conclude this discussion by summarising the recipe for obtaining the NNDL hard matrix-element corrections to the Lund multiplicity.

1. Our prescription to define the jet flavour is as follows. If the jet has a single parton, the jet flavour is taken as the flavour of that parton. If instead the jet has 2 partons of flavour indices b, c, the sum $b + c$ is defined as follows: for 2 gluons the sum is a gluon, for a quark and a gluon the sum is a quark, for a same-flavour $q\bar{q}$ pair the sum is a gluon, and for all the other cases the sum is taken as a quark.
2. The Born-level cross-sections $\sigma_0^{(a)}$ for quark and gluon flavours can be obtained from a Monte Carlo simulation including all the required fiducial cuts.
3. With the above flavour prescription, the NLO corrections $\sigma_1^{(a)}$ for quark and gluon jets can be obtained, including fiducial cuts, from any Monte Carlo generator providing information about the flavour of the final-state partons. This defines
$$\frac{\alpha_s}{2\pi} D^{(a)}_{\text{hme,NLO}} = \frac{\sigma_1^{(a)}}{\sigma_0^{(a)}}. \tag{5.2.19}$$
4. We compute the second term in (5.2.18) from a simulation of the real NLO corrections to the cross-section. We select jets with two partons (of flavour b and c) and study the cumulative distribution of their relative $\ln k_t$. For each flavour channel, after subtracting the known DL and NDL contributions, the cumulative distribution tends to a constant at small $\ln k_t$. Further subtracting

the NNDL contribution from the collinear endpoint from this constant gives $\sigma^{(bc)}_{R,\text{hard}}$. We then define

$$\frac{\alpha_s}{2\pi} D^{(bc)}_{\text{hme},R} = \frac{\sigma^{(bc)}_{R,\text{hard}}}{\sigma_0^{(b+c)}}. \tag{5.2.20}$$

A practical example of the extraction of $D^{(bc)}_{\text{hme},R}$ from Monte Carlo simulations is given in appendix B of Ref. [3].

The last hard matrix-element correction that has to be taken into account arises by expanding the normalisation in (5.2.18) as $\frac{1}{\sigma_0+\sigma_1} \sim \frac{1}{\sigma_0}\left(1 - \frac{\sigma_1}{\sigma_0}\right)$. The NNDL hard matrix-element correction to the Lund multiplicity thus takes the form

$$\begin{aligned}\delta N^{(\text{NNDL})}_{\text{hme}} = &\sum_a \left(\frac{\alpha_s}{2\pi} D^{(a)}_{\text{hme,NLO}} - \frac{\sigma_1}{\sigma_0}\right) f_a N^{(\text{DL})}_a(L) \\ &+ \sum_{bc} f_{b+c} \frac{\alpha_s}{2\pi} D^{(bc)}_{\text{hme},R} [N^{(\text{DL})}_b(L) + N^{(\text{DL})}_c(L) - N^{(\text{DL})}_a(L)],\end{aligned} \tag{5.2.21}$$

with $f_a = \frac{\sigma_0^{(a)}}{\sigma_0}$ the Born-level partonic fractions. One can gather the quark and gluon contributions and write

$$\alpha_s h_{3,\text{hme}}(\xi) = \delta N^{(\text{NNDL})}_{\text{hme}} = \frac{\alpha_s}{2\pi}\left[D^q_{\text{hme}} N^{(\text{DL})}_q(L) + D^g_{\text{hme}} N^{(\text{DL})}_g(L)\right], \tag{5.2.22}$$

with

$$D^q_{\text{hme}} = \left(D^{(q)}_{\text{hme,NLO}} + D^{(qg)}_{\text{hme},R} + D^{(qq)}_{\text{hme},R} - \frac{2\pi\sigma_1}{\alpha_s\sigma_0}\right) f_q + 2D^{(q\bar{q})}_{\text{hme},R} f_g, \tag{5.2.23a}$$

$$D^g_{\text{hme}} = \left(D^{(g)}_{\text{hme,NLO}} + D^{(gg)}_{\text{hme},R} - D^{(q\bar{q})}_{\text{hme},R} - \frac{2\pi\sigma_1}{\alpha_s\sigma_0}\right) f_g. \tag{5.2.23b}$$

5.2.3.2 Interplay between the top and bottom of the Lund plane

Let us now focus on the contribution associated with diagram 5.2b, corresponding to an endpoint contribution for the radiation of a soft gluon at large angles. Going back to the derivation of the NDL large-angle contribution from Sec. 5.2.2, we note that, after we changed variable from $k_\perp$ to $k_t = k_\perp\Delta$, the integration over k_t gave both the NDL contribution and an NNDL correction. More precisely, Eq. (5.2.8) can be rewritten as

$$\int_{k_{t,\text{cut}}}^{p_\perp\Delta_k} \frac{\mathrm{d}k_t}{k_t} = \int_{k_{t,\text{cut}}}^{p_\perp R} \frac{\mathrm{d}k_t}{k_t} - \int_{p_\perp\Delta_k}^{p_\perp R} \frac{\mathrm{d}k_t}{k_t} = L + (\text{NNDL}_{\text{top}}), \tag{5.2.24}$$

where we see that the NNDL correction ($\text{NNDL}_{\text{top}} \equiv \ln(\Delta_k/R)$) is, by construction, associated with the hard k_t scale. Because this is equivalent to being associated with the top of the Lund plane, it can absorbed into the hard matrix-element correction computed in the previous section. As a corollary, the contribution at the bottom of the Lund plane, diagram 5.2b, vanishes.

The argument can be extended to the case of diagram 5.2c, where a first large-angle correction would be followed by a secondary emission close to the $k_{t,\text{cut}}$ threshold. For this, we consider the all-order expression obtained by adding a tower of soft-collinear gluons to a first large-angle emission as given by Eq. (5.2.7) (assuming for simplicity that the (ab) dipole does not involve the jet leading parton):

$$\begin{aligned}\delta N_{\mathcal{C},(ab),\mathcal{O}(\alpha_s)} =& \frac{\alpha_s}{2\pi}\omega_{ab}^{\mathcal{C}} \int_0^{p_\perp} \frac{\mathrm{d}k_\perp}{k_\perp} \int_{\Delta_k<R} \mathrm{d}y \, \frac{\mathrm{d}\phi}{2\pi} \times \\ & k_\perp^2 (k|ab)\Theta(k_t > k_{t,\text{cut}}) N^{(\text{DL})}\Big(L; \ln \frac{p_\perp R}{k_\perp \Delta_k}\Big),\end{aligned} \tag{5.2.25}$$

where the last factor includes soft-collinear gluon radiation from the k_t scale of the first emission, $k_\perp \Delta_k$, down to the cut-off scale $k_{t,\text{cut}}$. Changing variables from $k_\perp$ to $k_t = k_\perp \Delta_k$, one recovers the same picture as above, namely the NDL contribution plus an NNDL correction when the first emission is at the top of the Lund plane (the second term in Eq. (5.2.24)) dressed with DL soft-collinear radiation. In particular, written in terms of k_t, the dressing factor $N^{(\text{DL})}\Big(L; \ln \frac{p_\perp R}{k_\perp \Delta_k}\Big)$ is simply $N^{(\text{DL})}\Big(L; \ln \frac{p_\perp R}{k_t}\Big)$, i.e. the DL result with no NDL corrections. This means that the contribution from diagram 5.2c also vanishes.

This vanishing of diagrams 5.2b and 5.2c carries some degree of arbitrariness and indicates a freedom in the calculation to reshuffle contributions across different corrections. More concretely, a fraction of the contribution associated with the top of the Lund plane can be redistributed into a contribution at the bottom of the Lund plane (starting at $\mathcal{O}(\alpha_s)$) and a contribution associated with diagram 5.2c (starting at $\mathcal{O}(\alpha_s^2)$). This reorganisation is done without changing the all-order NNDL final result, similar to what we encountered in Sec. 4.3.3.3. To illustrate this, let us take a different approach where we instead change variable from $k_\perp$

to, e.g., $\tilde{k}_\perp = k_\perp R$. In this case, the integration with a single large-angle gluon, i.e. the analogue of Eq. (5.2.24), would give

$$\int_0^{p_\perp R} \frac{\mathrm{d}\tilde{k}_\perp}{\tilde{k}_\perp}\Theta(k_t > k_{t,\mathrm{cut}}) = \int_{k_{t,\mathrm{cut}}\frac{\Delta_k}{R}}^{p_\perp R} \frac{\mathrm{d}k_t}{k_t} = \int_{k_{t,\mathrm{cut}}}^{p_\perp R} \frac{\mathrm{d}k_t}{k_t} + \int_{k_{t,\mathrm{cut}}\Delta_k/R}^{k_{t,\mathrm{cut}}} \frac{\mathrm{d}k_t}{k_t}$$
$$= L + (\mathrm{NNDL}_{\tilde{k}_\perp,\mathrm{bottom}}), \tag{5.2.26}$$

with

$$(\mathrm{NNDL}_{\tilde{k}_\perp,\mathrm{bottom}}) = (\mathrm{NNDL}_{\mathrm{top}}) = \ln\frac{\Delta_k}{R}, \tag{5.2.27}$$

with $(\mathrm{NNDL}_{\mathrm{top}})$ the contribution from the top of the Lund plane from Eq. (5.2.24). After integrating over Δ_k, this would give a constant. At order α_s, this is simply equivalent to reshuffling an NNDL correction from the top to the bottom of the Lund plane. At all orders, the contributions from the top and bottom of the Lund plane are dressed with different DL contributions. In practice, one can show that since the contribution from diagram 5.2c is also non-zero, the all-order result remains the same independently of the use of $\tilde{k}_\perp$ or $k_\perp$, as expected.

5.2.3.3 Two large-angle emissions

We now investigate the case in which a Born-level configuration ($p_1p_2 \to p_jp_r$) emits a soft-and-large-angle gluon, k_1, which then radiates a soft emission k_2 at a commensurate angle, $\Delta_{k_1k_2} \sim \Delta_{jk_1}$. Due to the purely soft nature of this correction, we can again split it in a quark- and a gluon-jet contribution

$$h_{3,\mathrm{la}^2}(\xi) = f_q h^{(q)}_{3,\mathrm{la}^2}(\xi) + f_g h^{(g)}_{3,\mathrm{la}^2}(\xi) \quad \text{with} \quad \alpha_s h^{(i)}_{3,\mathrm{la}^2}(\xi) = \sum_{\mathcal{C}} \frac{\sigma^{(i)}_{\mathcal{C}}}{\sigma^{(i)}} \sum_{(ab)\in\mathrm{event}} \delta N^{(\mathrm{NNDL})}_{\mathcal{C},(ab),\mathrm{la}^2}, \tag{5.2.28}$$

where we decomposed the hard Born-level process into a sum over partonic channels, $\mathcal{C}$, and coloured dipoles (ab), as in Sec. 5.2.2. While the methods in Sec. 5.2.2 allow us to account for the primary emission at full colour, we here adopt a simplified approach and describe the second emission in the large-N_c limit. If the gluon k_1 is radiated from dipole (ab), we thus only have to consider, for a real k_1, the radiation of

gluon k_2 from either the (ak_1) or the (k_1b) dipole and, for a virtual k_1, the radiation of k_2 from the (ab) dipole. At $\mathcal{O}(\alpha_s^2)$, the Lund multiplicity is thus given by

$$\begin{aligned}\delta N_{\mathcal{C},(ab),\mathrm{la}^2,\mathcal{O}(\alpha_s^2)} = \left(\frac{\alpha_s}{2\pi}\right)^2 \omega_{ab}^{\mathcal{C}} N_c \int_0^{p_\perp} \frac{\mathrm{d}k_{\perp 1}}{k_{\perp 1}} \int_0^{k_{\perp 1}} \frac{\mathrm{d}k_{\perp 2}}{k_{\perp 2}} \int \mathrm{d}y_1 \mathrm{d}y_2 \frac{\mathrm{d}\phi_1}{2\pi} \frac{\mathrm{d}\phi_2}{2\pi} \\ \times k_{\perp 1}^2 (k_1|ab)\, k_{\perp 2}^2 [(k_2|ak_1) + (k_2|bk_1) - (k_2|ab)] \\ \times \Theta(\Delta_2 < R)\Theta(k_{t2} > k_{t,\mathrm{cut}}),\end{aligned} \tag{5.2.29}$$

with Δ_i the distance between gluon k_i and the jet axis. Here, the eikonal factors were defined in Eq. (5.2.5), $\Theta(\Delta_2 < R)$ ensures that k_2 is emitted inside of the jet, and we made explicit the use of the large-N_c approximation for the second emission. Note that the gluon k_1 can be emitted either inside or outside of the jet. In writing Eq. (5.2.29), we have implicitly assumed that the jet had been clustered with the anti-k_t algorithm, allowing us to write the condition that the second emission is in the jet as $\Theta(\Delta_2 < R)$. For a different jet algorithm, this would have to be adapted, hence potentially yielding a different result at NNDL accuracy.

In order to isolate the NNDL terms in Eq. (5.2.29), we first subtract the DL and NDL contributions. For dipoles not involving the jet ((12), $(1r)$ and $(2r)$), $(k_1|ab)$ has no collinear singularity when $\Delta_1 \to 0$. The only contribution up to NDL is thus that of k_1 being emitted inside the jet at large angles with k_2 being a DL soft-and-collinear dressing. One therefore has the following subtracted integrand:

$$I_{ab} = k_{\perp 1}^2 (k_1|ab) \left\{ k_{\perp 2}^2 [(k_2|ak_1) + (k_2|k_1b) - (k_2|ab)]\Theta(\Delta_2 < R) - \frac{4}{\Delta_{12}^2}\Theta(\Delta_1, \Delta_{12} < R) \right\}. \tag{5.2.30}$$

For dipoles involving the jet ($(1j)$, $(2j)$ and (rj)), there are two contributions to subtract: a DL one where both gluons are soft and collinear with the second radiated as a secondary emission from the first one, and a NDL one where k_1 occurs at large angles and k_2 is a DL soft-and-collinear dressing. This gives

$$\begin{aligned} I_{aj} = k_{\perp 1}^2 (k_1|1j) k_{\perp 2}^2 [(k_2|ak_1) + (k_2|jk_1) - (k_2|aj)]\Theta(\Delta_2 < R) \\ - \frac{2}{\Delta_1^2}\frac{4}{\Delta_{12}^2}\Theta(\Delta_{12} < \Delta_1 < R) - \left[k_{\perp 1}^2 (k_1|aj) - \frac{2}{\Delta_1^2}\right]\frac{4}{\Delta_{12}^2}\Theta(\Delta_1, \Delta_{12} < R). \end{aligned} \tag{5.2.31}$$

In writing the subtraction terms, we have split the radiation of the first soft gluon into a collinear contribution $2/\Delta_1^2$ and a large-angle contribution $k_{\perp 1}^2 (k_1|aj) - 2/\Delta_1^2$.

After performing these subtractions, the angular integrations are finite and do not show any collinear enhancement. At $\mathcal{O}(\alpha_s^2)$ we can thus trivially perform the $k_\perp$ integrals by replacing $k_{t2} \to k_{\perp 2} R$ (see Eq. (5.2.8)), which simply gives a factor $L^2/2$. The NNDL correction to the multiplicity is then

$$\delta N^{(\mathrm{NNDL})}_{\mathcal{C},(ab),\mathrm{la}^2,\mathcal{O}(\alpha_s^2)} = \left(\frac{\alpha_s}{2\pi}\right)^2 \omega^{\mathcal{C}}_{ab} N_c \frac{L^2}{2} D^{\mathrm{la}^2}_{ab}, \tag{5.2.32}$$

with

$$D^{\mathrm{la}^2}_{ab} = \int_{-\infty}^{\infty} \mathrm{d}y_1 \int_{-\infty}^{\infty} \mathrm{d}y_2 \int_{-\pi}^{\pi} \frac{\mathrm{d}\phi_1}{2\pi} \int_{-\pi}^{\pi} \frac{\mathrm{d}\phi_2}{2\pi}\, I_{ab}. \tag{5.2.33}$$

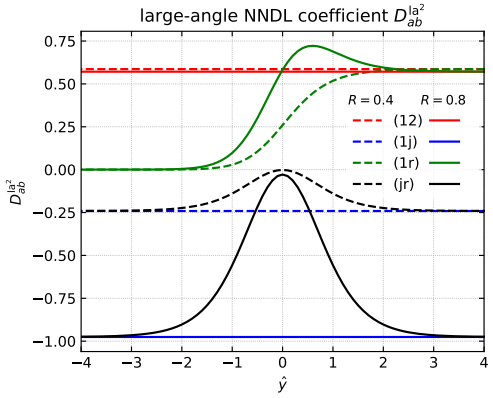
We could not find analytic expressions for the integrals in Eq. (5.2.33) so we evaluated them numerically.[5] As for the NDL D^{la}_{ab} coefficients, the $D^{\mathrm{la}^2}_{ab}$ coefficients involving the recoiling jet depend on the rapidity difference between the jet and the recoiling jet, $2\hat{y}$ in the notations of Sec. 5.2.2. For reproducibility purposes, we show the coefficients $D^{\mathrm{la}^2}_{ab}$ in Fig. 5.3 together with the numerical values obtained for $\hat{y} = 0$ for two different jet radii. Furthermore, $D^{\mathrm{la}^2}_{2j} = D^{\mathrm{la}^2}_{1j}$ and $D^{\mathrm{la}^2}_{2r}$ is obtained from $D^{\mathrm{la}^2}_{1r}$ taking $\hat{y} \to -\hat{y}$. As expected, $D^{\mathrm{la}^2}_{1r}$ goes to 0 at large negative $\hat{y}$ and to $D^{\mathrm{la}^2}_{12}$ at large positive $\hat{y}$. Similarly, $D^{\mathrm{la}^2}_{jr}$ tends to $D^{\mathrm{la}^2}_{1j}$ at large $|\hat{y}|$.

At all orders, since this correction affects just the first two emissions, we only need to account for subsidiary DL radiation from the second gluon. That is, the NNDL correction when k_1 is emitted from the (ab) dipole is

$$\delta N^{(\mathrm{NNDL})}_{\mathcal{C},(ab),\mathrm{la}^2} = \left(\frac{\alpha_s}{2\pi}\right)^2 \omega^{\mathcal{C}}_{ab} N_c D^{\mathrm{la}^2}_{ab} \int_0^L \mathrm{d}\ell_1 \int_{\ell_1}^L \mathrm{d}\ell_2\, N_g^{(\mathrm{DL})}(L-\ell_2) = \frac{\alpha_s}{2\pi} \omega^{\mathcal{C}}_{ab}\, D^{\mathrm{la}^2}_{ab}\, \frac{1}{4}(\cosh\nu - 1). \tag{5.2.34}$$

The total result is obtained after summing over all possible coloured dipoles and partonic channels as written in Eq. (5.2.28), where the kinematic weights $\omega^{\mathcal{C}}_{ab}$ for inclusive jet (Z+jet) events are given in appendix A of Ref. [3] (Tab. 5.1).

[5] We could tentatively do an expansion in the jet radius R as in Sec. 5.2.2 but the coefficients of this expansion would also have to be evaluated numerically so we preferred the fully numerical solution. We note however that, at small R, the $D^{\mathrm{la}^2}_{ab}$ coefficients behave like $R^2 \ln R^2$. This behaviour comes from configurations where the first emission is outside the jet but very close to the jet boundary with the second emission inside the jet and also close to the jet boundary so that the $\ln R^2$ enhancement is of collinear origin. See e.g. Refs. [91, 92] for additional discussions.



Values for $\hat{y} = 0$

R	0.4	0.8
$D_{12}^{\mathrm{la}^2}$	0.5864261(12)	0.5712475(12)
$D_{1j}^{\mathrm{la}^2} = D_{2j}^{\mathrm{la}^2}$	-0.24098(15)	-0.97564(17)
$D_{1r}^{\mathrm{la}^2} = D_{2r}^{\mathrm{la}^2}$	0.259460(11)	0.582097(13)
$D_{jr}^{\mathrm{la}^2}$	-0.0017776(17)	-0.0285608(17)

Figure 5.3: NNDL coefficients $D_{ab}^{\mathrm{la}^2}$ for each dipole coming from two emissions at large angles. The results are provided for both $R = 0.4$ and $R = 0.8$ jets. The table on the right gives numerical values for $\hat{y} = 0$.

5.2.3.4 A large-angle emission and a hard-collinear emission

This corresponds to the case of a soft-and-large-angle gluon emission together with a subsidiary hard-collinear emission (either a $g \to gg$ or a $g \to q\bar{q}$ splitting) as displayed in Fig. 5.2e. As in the above section we split the contribution with respect to the jet flavour

$$h_{3,\mathrm{la}\times\mathrm{hc}}(\xi) = f_q h^{(q)}_{3,\mathrm{la}\times\mathrm{hc}}(\xi) + f_g h^{(g)}_{3,\mathrm{la}\times\mathrm{hc}}(\xi) \quad \text{with} \tag{5.2.35}$$
$$\alpha_s h^{(i)}_{3,\mathrm{la}\times\mathrm{hc}}(\xi) = \sum_{\mathcal{C}} \frac{\sigma^{(i)}_{\mathcal{C}}}{\sigma^{(i)}} \sum_{(ab)\in\mathrm{event}} \delta N^{(\mathrm{NNDL})}_{\mathcal{C},(ab),\mathrm{la}\times\mathrm{hc}}.$$

The starting point for computing $\delta N^{(\mathrm{NNDL})}_{\mathcal{C},(ab),\mathrm{la}\times\mathrm{hc}}$ is the result of Sec. 5.2.2, where we calculated the correction to the Lund multiplicity due to a primary, large-angle emission. Instead of dressing this soft, large-angle, gluon with a tower of DL emissions, we now have to account for a single hard-collinear correction anywhere in this chain of gluons. For this, we can recycle the NDL hard-collinear correction to the multiplicity, $\delta N^{(\mathrm{NDL})}_{g,\mathrm{hc}}(L;\ell)$, computed between the relative transverse momentum scale $e^{-\ell} p_\perp R$ at which the first large-angle gluon is emitted and the cut-off scale $k_{t,\mathrm{cut}} = e^{-L} p_\perp R$. This is captured by the sum of Eq. (4.2.25), and Eq. (4.2.27), multiplied by $\sqrt{\alpha_s}$ and evaluated for $L - \ell$. We therefore have

$$\begin{aligned}\delta N^{(\mathrm{NNDL})}_{\mathcal{C},(ab),\mathrm{la}\times\mathrm{hc}} &= \frac{\alpha_s}{\pi} \omega^{\mathcal{C}}_{ab} D^{\mathrm{la}}_{ab} \int_0^L d\ell\, \delta N^{(\mathrm{NDL})}_{g,\mathrm{hc}}(L;\ell) \\ &= \frac{\alpha_s}{2\pi} \omega^{\mathcal{C}}_{ab} D^{\mathrm{la}}_{ab} \left[(B_{gg} + c_\delta B_{gq}) \nu \sinh\nu + 2B_{gq}(1 - c_\delta)(\cosh\nu - 1) \right],\end{aligned} \tag{5.2.36}$$

where $c_\delta = (2C_F - C_A)/C_A$. The total result is obtained after summing over all possible coloured dipoles and partonic channels as written in Eq. (5.2.35). Again, the kinematic weights $\omega^{\mathcal{C}}_{ab}$ can be found in Tab. 5.1 for Z+jet events and in appendix A of Ref. [3] for an inclusive jet sample.

5.2.3.5 A large-angle emission and a running-coupling correction

The structure of this correction is similar to that in the previous section with the main difference being that the running-coupling correction can affect either the soft large-angle emission itself, or any subsidiary soft-and-collinear emission. We therefore write

$$\begin{aligned}\delta N^{(\mathrm{NNDL})}_{\mathcal{C},(ab),\mathrm{la}\times\mathrm{rc}} &= \frac{\alpha_s}{\pi}\omega^{\mathcal{C}}_{ab} D^{\mathrm{la}}_{ab}\int_0^L d\ell\left[2\alpha_s\beta_0\ell N^{(\mathrm{DL})}_g(L-\ell) + \delta N^{(\mathrm{NDL})}_{g,\mathrm{rc}}(L;\ell)\right] \\ &= \frac{\alpha_s}{2C_A}\omega^{\mathcal{C}}_{ab} D^{\mathrm{la}}_{ab}\frac{\beta_0}{2}\nu\left[\nu\cosh\nu + \sinh\nu\right],\end{aligned} \tag{5.2.37}$$

where $\delta N^{(\mathrm{NDL})}_{g,\mathrm{rc}}(L;\ell)$ is the NDL resummed running-coupling correction of a gluon radiating from scale $k_t = p_\perp R e^{-\ell}$ to $k_{t,\mathrm{cut}}$, given in Eq. (4.3.60). The first (second) term in the integrand corresponds to dressing the large-angle emission (any subsidiary emission) with a running-coupling correction, respectively. As before, the full NNDL correction $h_{3,\mathrm{la}\times\mathrm{rc}}(\xi)$ is obtained by summing the contributions in Eq. (5.2.37) for each dipole and partonic channel, as in Eq. (5.2.35).

5.2.4 Final result

For completeness, we summarise here the necessary expressions needed to compute the average Lund multiplicity within a high-energy anti-k_t jet with transverse momentum $p_\perp$ up to NNDL accuracy, i.e. up to h_3 in Eq. (2.3.6). We define $\alpha_s \equiv \alpha_s(p_\perp R), L \equiv \ln(p_\perp R/k_{t,\mathrm{cut}}), \xi \equiv \alpha_s L^2, \nu \equiv \sqrt{2C_A\xi/\pi}, c_\delta \equiv (2C_F - C_A)/C_A$ and $f_{q,g} \equiv \sigma_{q,g}/(\sigma_q + \sigma_g)$ the Born-level fractions of quark and gluon jets. The DL function is

$$h_1(\xi) = f_q h^{(q)}_{1,\mathrm{coll}}(\xi) + f_g h^{(g)}_{1,\mathrm{coll}}(\xi) \qquad \text{with} \qquad h^{(i)}_{1,\mathrm{coll}}(\xi) = 1 + \frac{C_i}{C_A}\left(\cosh\nu - 1\right). \tag{5.2.38}$$

The NDL function is

$$h_2(\xi) = f_q h^{(q)}_{2,\text{coll}}(\xi) + f_g h^{(g)}_{2,\text{coll}}(\xi) + \frac{1}{\sqrt{2\pi C_A}} \sum_{i\in(q,g)} \sum_{\substack{\mathcal{C}\in\text{flavour}\\ \text{channels}}} \frac{\sigma^{(i)}_{\mathcal{C}}}{\sigma^{(i)}} \sum_{(ab)\in\text{event}} \omega^{\mathcal{C}}_{ab} D^{\text{la}}_{ab} \sinh\nu, \tag{5.2.39}$$

and the NNDL function is

$$\begin{aligned} 2\pi h_3(\xi) = {} & 2\pi[f_q h^{(q)}_{3,\text{coll}}(\xi) + f_g h^{(g)}_{3,\text{coll}}(\xi)] + D^q_{\text{hme}}\left[\frac{C_F}{C_A}(\cosh\nu - 1) + 1\right] + D^g_{\text{hme}}\cosh\nu \\ & + \sum_{i\in(q,g)} \sum_{\substack{\mathcal{C}\in\text{flavour}\\ \text{channels}}} \frac{\sigma^{(i)}_{\mathcal{C}}}{\sigma^{(i)}} \sum_{(ab)\in\text{event}} \omega^{\mathcal{C}}_{ab}\Bigg\{ D^{\text{la}^2}_{ab}\ \frac{1}{4}(\cosh\nu - 1) \\ & \qquad + D^{\text{la}}_{ab}\frac{\pi\beta_0}{2C_A}\,\nu[\nu\cosh\nu + \sinh\nu] \\ & \qquad + D^{\text{la}}_{ab}[(B_{gg} + c_\delta B_{gq})\nu\sinh\nu + 2B_{qg}(1 - c_\delta)(\cosh\nu - 1)]\Bigg\}. \end{aligned} \tag{5.2.40}$$

In the above expressions, we have recycled the collinear pieces of the e^+e^- results, i.e. $h^{(i)}_{2,\text{coll}}(\xi)$ is defined Eq. (4.3.72), and $h^{(q)}_{3,\text{coll}}(\xi)$ and $h^{(g)}_{3,\text{coll}}(\xi)$ are defined in Eq. (4.3.75) and (4.3.78), respectively.

5.2.5 From fixed kinematics to fiducial cuts

So far, we have considered contributions to the average Lund multiplicity stemming from jets with a fixed transverse momentum and rapidity. In order to provide realistic predictions for a collider environment, we have to relax that assumption and average our analytic result with the cross-section for producing jets within a given acceptance, i.e.

$$\langle\overline{N^{(\text{Lund})}}\rangle(\alpha_s; \ln(p_{\perp,\min}R/k_{t,\text{cut}})) = \frac{1}{\sigma}\int_{p_{\perp,\min}} \frac{\mathrm{d}^2\sigma}{\mathrm{d}p_\perp \mathrm{d}y}\,\langle N^{(\text{Lund})}(\alpha_s; L_{\text{jet}})\rangle\,\mathrm{d}p_\perp \mathrm{d}y, \tag{5.2.41}$$

where $p_{\perp,\min}$ is the minimum jet transverse momentum selected, $\mathrm{d}^2\sigma/\mathrm{d}p_\perp\mathrm{d}y$ is the double-differential distribution in both the transverse momentum $p_\perp$ and rapidity y of the jet. Finally, σ is the total jet cross-section, meaning that we are effectively computing the average multiplicity per jet passing the cuts. At NNDL accuracy, our expressions for the multiplicity already include, through the contribution from

the top of the Lund plane derived in Sec. 5.2.3.1, the non-trivial NLO corrections from the hard matrix element. The convolution in Eq. (5.2.41) should therefore be performed using the Born-level cross-section.

In practice, one could compute the average multiplicity in jets as a function of $p_\perp$ and y, and perform the integration in Eq. (5.2.41) explicitly. However, this integration can be simplified by realising that, due to the steeply falling nature of the jet spectrum, $p_\perp$ and $p_{\perp,\min}$ are commensurate. One can thus replace L_{jet} by $L \equiv L_{\min} = \ln(p_{\perp,\min}R/k_{t,\text{cut}})$ as the resummation scale in Eq. (2.3.6). Since $L_{\text{jet}} - L \equiv \delta_L = \ln(p_\perp/p_{\perp,\min})$ does not bring new large logarithms, one can expand the right hand side of Eq. (5.2.41), up to NNDL accuracy, as

$$\begin{aligned}\langle N^{(\text{Lund})}(\alpha_s; L_{\text{jet}})\rangle = h_1(\xi) + \sqrt{\alpha_s}\Big[h_2(\xi) + 2\delta_L\sqrt{\xi}\,h_1'(\xi)\Big] \\ + \alpha_s\Big[h_3(\xi) + (\delta_L^2 - 2\beta_0\delta_L\,\xi)h_1'(\xi) + 2\delta_L^2\,\xi\,h_1''(\xi) + 2\delta_L\sqrt{\xi}\,h_2'(\xi)\Big],\end{aligned} \tag{5.2.42}$$

with $\xi = \alpha_s L^2$, $\alpha_s = \alpha_s(p_{\perp,\min}R)$ and $h_i'(\xi)$ ($h_i''(\xi)$) the first (second) derivative of $h_i(\xi)$ with respect to ξ. The main advantage of this approach is that the resummation functions $h_i(\xi)$, given by Eqs. (5.2.38)-(5.2.40) are independent of the jet $p_\perp$ and y. The integration over the jet spectrum in Eq. (5.2.41) thus reduces to computing a few specific quantities such as

$$\bar{\delta}_L = \frac{1}{\sigma}\int \frac{\mathrm{d}^2\sigma}{\mathrm{d}p_\perp \mathrm{d}y}\ln\frac{p_\perp}{p_{\perp,\min}}\,\mathrm{d}p_\perp\mathrm{d}y, \tag{5.2.43a}$$

$$\bar{\delta}_L^2 = \frac{1}{\sigma}\int \frac{\mathrm{d}^2\sigma}{\mathrm{d}p_\perp \mathrm{d}y}\ln^2\frac{p_\perp}{p_{\perp,\min}}\,\mathrm{d}p_\perp\mathrm{d}y, \tag{5.2.43b}$$

as well as quantities related to the radiation of soft gluons at large angles entering at NDL and NNDL, i.e.[6]

$$\overline{\omega D_i^{\text{la}}} = \sum_{\mathcal{C}\in\text{flavour channels}}\frac{1}{\sigma^{(i)}}\int\frac{\mathrm{d}^2\sigma_{\mathcal{C}}^{(i)}}{\mathrm{d}p_\perp\mathrm{d}y}\sum_{(ab)\in\text{event}}\omega_{ab}^{\mathcal{C}}D_{ab}^{\text{la}}\,\mathrm{d}p_\perp\mathrm{d}y, \tag{5.2.44a}$$

$$\overline{\omega D_i^{\text{la}^2}} = \sum_{\mathcal{C}\in\text{flavour channels}}\frac{1}{\sigma^{(i)}}\int\frac{\mathrm{d}^2\sigma_{\mathcal{C}}^{(i)}}{\mathrm{d}p_\perp\mathrm{d}y}\sum_{(ab)\in\text{event}}\omega_{ab}^{\mathcal{C}}D_{ab}^{\text{la}^2}\,\mathrm{d}p_\perp\mathrm{d}y. \tag{5.2.44b}$$

[6] In practice, one needs to integrate over the full kinematics of the $2\to 2$ Born event since the $\omega_{ab}^{\mathcal{C}}D_{ab}^{\text{la}}$ and $\omega_{ab}^{\mathcal{C}}D_{ab}^{\text{la}^2}$ coefficients depend on the relative $\hat{y}$ between the measured jet and the recoiling Born-level parton.

In Eqs. (5.2.43) and (5.2.44), we can again perform the integration using the Born-level matrix element. All the coefficients entering Eq. (5.2.42) depend on the underlying hard process as well as the imposed fiducial cuts.

5.3 Numerical results

In this section we discuss some phenomenological considerations for the average Lund jet multiplicity, including the matching of our resummed predictions to exact fixed-order results, as well as non-perturbative corrections. For definiteness, we specialise our discussion to the case of Z+jet events and an inclusive jet sample in proton-proton collisions at a centre-of-mass energy $\sqrt{s} = 13.6$ TeV. In the Z+jet case we impose that $p_{\perp Z} > p_{\perp,\min} = 500$ GeV and $|y_Z| < 2.5$ (for simplicity, we disregard the Z decay in the fixed-order simulations). If the event passes these cuts, we then calculate the Lund multiplicity within the leading $R = 0.8$ anti-k_t jet, as obtained from FastJet [93], with $p_{\perp,\text{jet}} > p_{\perp Z}/2$ and $|y_{\text{jet}}| < 1.7$. In the inclusive jet sample, we select all $R = 0.8$ anti-k_t jets with $p_{\perp,\text{jet}} > p_{\perp,\min} = 750$ GeV and $|y_{\text{jet}}| < 1.7$.

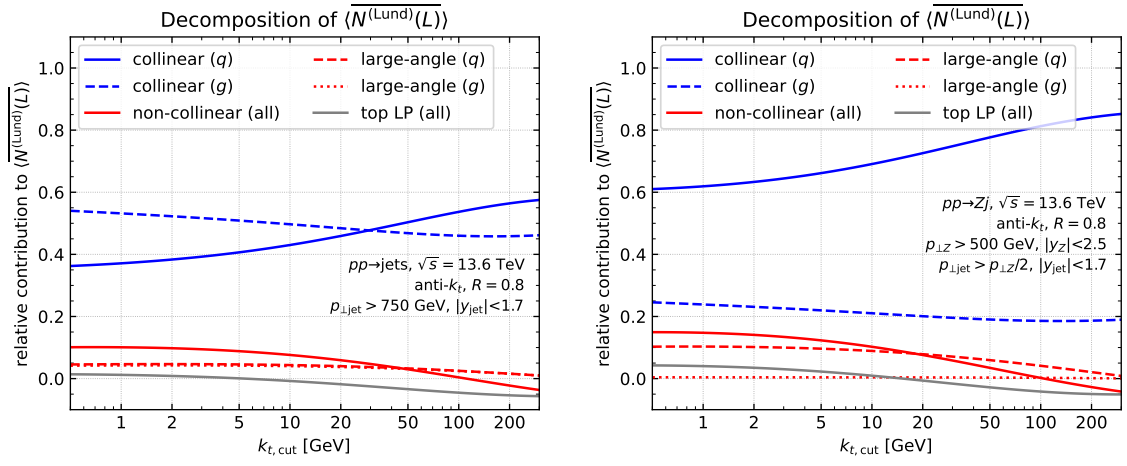
As discussed in Sec. 5.2.5, the NNDL-accurate resummed predictions involve a series of coefficients which depend on the underlying Born-level process. We obtain the Z+jet ones from `MadGraph` [94] and the inclusive jet ones from a version of `NLOJet++` [95] augmented so as to provide parton flavour information [96]. All the results reported here use the central PDF of the PDF4LHC21 set [97]. We set the central renormalisation scale to $p_{\perp,\min}R$ and the central factorisation scale to $\hat{H}_T$, the scalar sum of the transverse momentum of the final-state partons. The values for the resummation coefficients with this set of choices are listed in Tab. 5.2.

5.3.1 Resummation

Throughout this chapter, we have organised the calculation of the average Lund multiplicity as the sum of a collinear piece, identical to the e^+e^- result, and a large-angle piece. The collinear contribution is universal in the sense that it is process-independent and only depends on the Born-level jet flavour. Conversely, the large-angle contribution depends on the full structure of the hard process.

	Coefficient	
	Incl. jets	Z+jet
kinematic cuts	$p_{\perp,\text{jet}} > 750$ GeV	$p_{\perp Z} > 500$ GeV,$p_{\perp,\text{jet}} > \frac{1}{2}p_{\perp Z}$
	$(p_{\perp,\min} = 750$ GeV$)$	$(p_{\perp,\min} = 500$ GeV$)$
	$\lvert y_{\text{jet}}\rvert < 1.7$	$\lvert y_Z\rvert < 2.5$, $\lvert y_{\text{jet}}\rvert < 1.7$
strong coupling	$\alpha_s(Rp_{\perp,\min}) = 0.091$	$\alpha_s(Rp_{\perp,\min}) = 0.097$
quark, gluon jet fractions	$f_q = 0.553$	$f_q = 0.818$
	$f_g = 0.447$	$f_g = 0.182$
spectrum convolutions	$\bar{\delta}_L = -0.166$	$\bar{\delta}_L = -0.195$
	$\bar{\delta}_L^2 = 0.052$	$\bar{\delta}_L^2 = 0.071$
hard matrix-element	$D^q_{\text{hme}} = -9.331$	$D^q_{\text{hme}} = -11.545$
	$D^g_{\text{hme}} = 5.508$	$D^g_{\text{hme}} = 8.285$
two large-angle emissions	$\overline{\omega D_q^{\text{la}^2}} = 0.030$	$\overline{\omega D_q^{\text{la}^2}} = -0.074$
	$\overline{\omega D_g^{\text{la}^2}} = -0.246$	$\overline{\omega D_g^{\text{la}^2}} = -0.504$

Table 5.2: Coefficients entering the NDL h_2 and NNDL h_3 functions for our two jet samples, inclusive jets and Z+jet events with $R = 0.8$ in both cases.



(a) **(b)**

Figure 5.4: Relative weight of each term to the total Lund multiplicity at NNDL accuracy for an inclusive sample of jets (left) and Z+jet events (right). We distinguish universal, collinear terms (blue) from those contributions which depend on the event structure, i.e. wide-angle radiation (red) and hard matrix-element corrections (grey).

Up to NNDL accuracy, it can be further split into a contribution associated with soft emissions (close to the edge of the jet), and genuine fixed-order corrections associated with an emission at the top of the Lund plane. The former is still associated with the Born-level jet flavour, but for the latter the breakdown into a quark and a gluon contribution is ambiguous.

To gain insight into the relative sizes of each of these contributions we plot in Fig. 5.4 the relative weights of the different contributions for both the inclusive jet sample and Z+jet events. Both the soft and the collinear contributions have explicitly been split according to flavour, and the contribution labelled as "non-collinear" includes both the contributions from soft-large-angle radiation as well as the contributions from the top of the Lund plane. For both hard processes, almost 90% of the Lund multiplicity is dominated by contributions of collinear origin. Focusing on the large-angle corrections, one sees that the contribution from hard emissions, i.e. at the top of the Lund plane, is further suppressed (roughly by a factor 2) compared to the soft-and-wide-angle contributions. The hard contribution is however larger for the Z+jet case than for inclusive jets, and, in both cases, changes sign as a function of $k_{t,\text{cut}}$. Globally speaking, this picture is in agreement with the fact that collinear effect start at DL accuracy, soft wide-angle effects start at NDL and top-of-the-Lund-plane corrections only contribute at NNDL. The fact that the number of emissions inside a jet is dominated by universal collinear physics depending only on the Born-level flavour of the jet is in quantitative agreement with the study of the dependence of quark and gluon jets on the topology of the hard process from Ref. [98].

Regarding the flavour decomposition of the result, the relative sizes of quark and gluon contributions differ considerably between the inclusive and the Z+jet sample. As expected, we find a larger relative contribution of quark-initiated jets in Z+jet events than in the inclusive sample. In the latter, the slightly higher initial fraction of quark-initiated jets (see Tab. 5.2) is compensated by Casimir scaling for small values of $k_{t,\text{cut}}$, i.e. gluons give a larger multiplicity than quarks at small $k_{t,\text{cut}}$. However, quark jets dominate down to $k_{t,\text{cut}} \sim 30$ GeV.

5.3.2 Phenomenological predictions

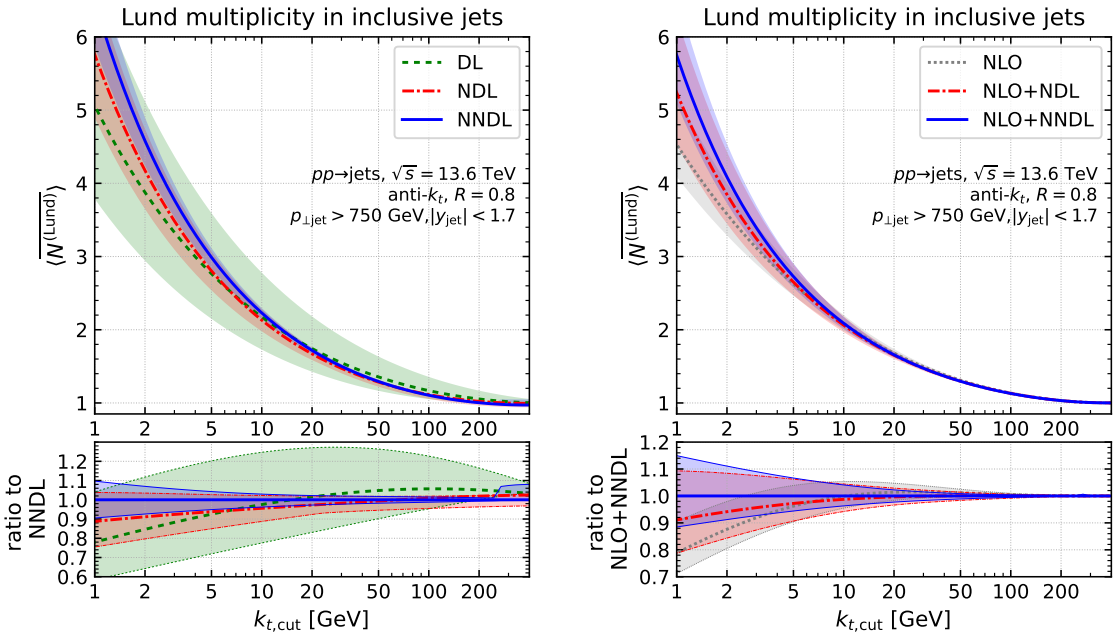
To produce realistic predictions for phenomenological applications at the LHC we match our resummed calculation, computed in Sec. 5.2, to the exact fixed-order result at NLO, i.e. $\mathcal{O}(\alpha_s^2)$ compared to the underlying $2 \to 2$ hard process.[7] We further account for theoretical uncertainties and include non-perturbative corrections. We perform these three steps in this section, focusing only on our inclusive jet sample for simplicity.

Theoretical uncertainties. We evaluate the uncertainties associated with missing higher orders by varying the renormalisation ($p_{\perp,\min}R$), factorisation ($\hat{H}_T$) and resummation scales ($p_{\perp,\min}R/k_{t,\text{cut}}$). To this end we multiply each of the scales by a dimensionless parameter, x_R, x_F and x_L respectively. Variations of x_F only affect quantities that depend on the averaging over the Born-level jet spectrum, i.e. quantities listed in Tab. 5.2. Conversely, when varying x_R and x_L one introduces spurious terms that spoil the perturbative accuracy of the resummation. To maintain NNDL accuracy, we introduce counter-terms so that our resummed expression becomes

$$\begin{aligned}\langle\overline{N^{(\text{Lund})}}\rangle_{\text{resum}} &= \bar{h}_1(\xi) + \sqrt{\alpha_s}\Big[h_2(\xi) + 2(\bar{\delta}_L - \ln x_L)\sqrt{\xi}\,\bar{h}_1'(\xi)\Big] \\ &+ \alpha_s\Big\{\bar{h}_3(\xi) + \Big[2\beta_0(\ln x_R - \bar{\delta}_L)\,\xi + \ln^2 x_L - 2\ln x_L\bar{\delta}_L + \bar{\delta}_L^2\Big]\,\bar{h}_1'(\xi) \\ &+ 2(\ln^2 x_L - 2\ln x_L\bar{\delta}_L + \bar{\delta}_L^2)\xi\,\bar{h}_1''(\xi) + 2\sqrt{\xi}\Big[\overline{\delta_L h_2'(\xi)} - \ln x_L\,\bar{h}_2'(\xi)\Big]\Big\},\end{aligned} \tag{5.3.1}$$

where the bar indicates an average over the jet spectrum as explained in Sec. 5.2.5. Note that, in the last term, we have used the short-hand notation $\overline{\delta_L h_2'(\xi)}$ to emphasise that, in the large-angle NDL contribution, one has to compute explicitly the overall $\overline{\delta_L \omega_{\mathcal{C}} D_i^{\text{la}}}$ coefficient averaged over Born-level events. All the other, collinear, NDL terms simply involve $\bar{\delta}_L$. In practice, we vary separately x_R, x_F and x_L between 0.5 and 2. Our total perturbative uncertainty is obtained by taking

[7] The first non-trivial order for the Lund multiplicity requires at least one emission on top of the underlying $2 \to 2$ process. This means that the LO and NLO fixed-order multiplicities we refer to in this section correspond respectively to a relative $\mathcal{O}(\alpha_s)$ and $\mathcal{O}(\alpha_s^2)$ compared to the hard $2 \to 2$ process.



(a) **(b)**

Figure 5.5: Left: Resummed Lund average multiplicity at DL (dashed, green), NDL (dash-dotted, red) and NNDL (solid, blue) as a function of $k_{t,\text{cut}}$ for LHC kinematics. Right: Average Lund multiplicity after matching with NLO. The pure NLO result is shown in dotted (grey) for reference, together with matched NLO+NDL (dash-dotted, red) and NLO+NNDL (solid, blue). The bottom panels display the ratio to the most accurate result (NNDL on the left and NLO+NNDL on the right).

the envelope of the 7-point scale variations [99] in $x_{R,F}$, and adding in quadrature the resummation uncertainty by varying x_L.

The numerical evaluation of Eq. (5.3.1) is displayed in Fig. 5.5a at DL, NDL and NNDL accuracy. Let us first focus on the central values. We observe that the NDL correction enhances the Lund multiplicity with respect to the DL result when $k_{t,\text{cut}} \lesssim 6$ GeV. We note that this was not the case in the e^+e^- result, where the NDL correction reduced the multiplicity for all $k_{t,\text{cut}}$ values. This increase in the multiplicity of high-energy jets is solely due to the large-angle emission correction calculated in Sec. 5.2.2. The NNDL corrections further increase the Lund multiplicity for $k_{t,\text{cut}} \lesssim 15$ GeV, and have only moderate impact for all larger values of $k_{t,\text{cut}}$. Turning to the uncertainty band, we find that it is remarkably reduced beyond DL accuracy. For example, at $k_{t,\text{cut}} = 5$ GeV (10 GeV), the error band shrinks from a $\sim 28\%$ ($\sim 24\%$) at DL to $\sim 10\%$ ($\sim 7\%$) at NDL accuracy

and further to $\sim 5\%$ ($\sim 3.4\%$) at NNDL accuracy, i.e. an additional reduction around 50%. We note that these small relative uncertainties at NNDL accuracy, even for very small $k_{t,\text{cut}}$, can be traced back to the fact that we are computing the cumulative distribution of the average Lund multiplicity. In other words, while the differential distribution would see relatively large uncertainties at small $k_{t,\text{cut}}$, e.g. 10% (7.5%) at $k_{t,\text{cut}} = 5$ GeV (10 GeV), those get smeared out in the cumulative distribution. For $k_{t,\text{cut}} \gtrsim p_{\perp,\min}R/2 = 300$ GeV, well beyond the regime of validity of the resummed result, we note the asymmetric and irregular shapes of the uncertainties associated with the NDL and NNDL accurate results respectively. This unphysical behaviour disappears after matching as we discuss next.

Matching. We use an additive scheme for the Lund multiplicity:

$$\begin{aligned}\langle\overline{N^{(\text{Lund})}}\rangle_{\text{match}} &= \langle\overline{N^{(\text{Lund})}}\rangle_{\text{fo}} \\ &+ \Big(\langle\overline{N^{(\text{Lund})}}\rangle_{\text{resum}} - \langle\overline{N^{(\text{Lund})}}\rangle_{\text{resum,fo}}\Big)\Big(1 - \frac{2k_{t,\text{cut}}}{p_{\perp,\min}R}\Big)\Theta\Big(k_{t,\text{cut}} < \frac{p_{\perp,\min}R}{2}\Big),\end{aligned} \tag{5.3.2}$$

where $\langle\overline{N^{(\text{Lund})}}\rangle_{\text{fo}}$ is the exact fixed-order result obtained from `NLOJet++` taken here at NLO, i.e. at $\mathcal{O}(\alpha_s^2)$ relative to the Born-level event, $\langle\overline{N^{(\text{Lund})}}\rangle_{\text{resum}}$ is the NNDL-accurate resummed result, Eq. (5.2.41), and we subtract $\langle\overline{N^{(\text{Lund})}}\rangle_{\text{resum,fo}}$, the $\mathcal{O}(\alpha_s^2)$ expansion of the resummed result, to avoid double counting. We also introduce a damping factor to interpolate between the resummed and fixed-order results that switches off the resummation at $k_{t,\text{cut}}^{\max} = p_{\perp,\min}R/2$ where it should not be trusted regardless. This ensures that the matched results reduce to the fixed-order at large values of $k_{t,\text{cut}}$, while not spoiling the NNDL accuracy at small $k_{t,\text{cut}}$ values.[8] We note that scale uncertainties are obtained using Eq. (5.3.1) for the resummed part. A similar expression is used for the fixed-order expansion $\langle\overline{N^{(\text{Lund})}}\rangle_{\text{resum,fo}}$ where the $h_i(\xi)$ functions and their derivatives are expanded in α_s. In the exact fixed-order results we use the x_R, x_F scale variations as provided by `NLOJet++`.

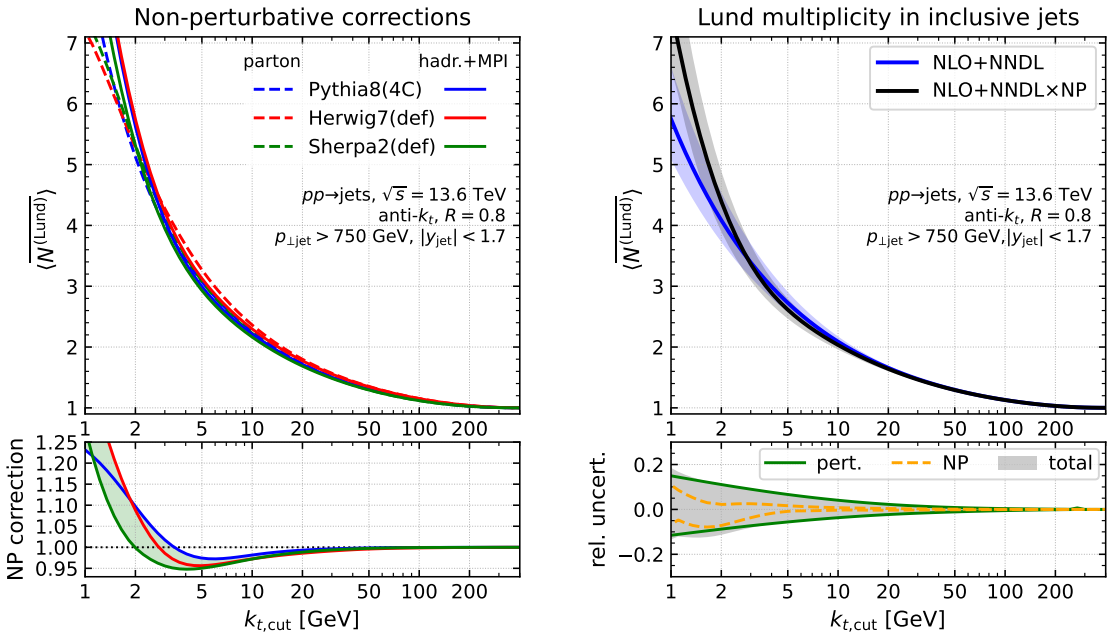
[8] One could alternatively have redefined L so that $L \to \ln(p_{\perp,\min}R/k_t)$ at small k_t and $L \to 0$ when k_t is large. Note also that, compared to our earlier e^+e^- study, Sec. 4.4.2 and Eq. (4.4.7), the k_t spectrum no longer has a well-defined fixed-order endpoint but has instead a tail extending far beyond $p_{\perp,\min}R$.

We show in Fig. 5.5b the effect of matching our NDL and NNDL accurate resummed result with the exact NLO result, as described in Eq. (5.3.2). We observe that the resummation slightly increases the value of the Lund multiplicity with an effect more pronounced as $k_{t,\text{cut}}$ decreases. As an example, taking the central value of Lund multiplicity curves at $k_{t,\text{cut}} = 5$ GeV we find that $\langle \overline{N^{(\text{Lund})}} \rangle$ is ≈ 2.6 at NLO and 2.7 at NLO+NNDL. The uncertainty band after matching increases due to the impact of x_R and x_F variations on the fixed-order result. Nevertheless, the error band on the NLO+NNDL result remains small, with a value of $\sim 6\%$ at 5 GeV and below 15% down to 1 GeV, as observed in the bottom panel of Fig. 5.5b. We also note that the matching procedure indeed washes out the unphysical behaviour observed at large $k_{t,\text{cut}}$ values for the resummed predictions in Fig. 5.5a.

Non-perturbative corrections. The last ingredient that we incorporate into our theoretical prediction alongside matching and scale variations is non-perturbative corrections due to hadronisation and multi-parton interactions (MPI). To estimate these we run the Pythia8.3 [76] (with `Monash13` [100], `4C` [101], and `Atlas14` [102] tunes), Herwig7.20 [78] and Sherpa2.2.11 [42] event generators at parton level and at hadron level with MPI turned on.

In Fig. 5.6a we show the average Lund multiplicity distributions obtained from our Monte Carlo simulations as well as the ratio between the hadron-level (including MPI) and parton-level results. For readability purposes, we only show the Pythia8 results for the `4C` tune, which typically drives the upper edge of the non-perturbative corrections (with the other two Pythia8 tunes showing intermediate non-perturbative corrections). Overall the non-perturbative corrections are small, staying within $\sim 5\%$ down to $k_{t,\text{cut}} \sim 3$ GeV.

Below $k_{t,\text{cut}} \sim 2$ GeV the non-perturbative corrections start to become significant. However, as noted earlier in Sec. 4.3.5, our resummation becomes questionable for values of L of order $1/(\beta_0 \alpha_s)$. This can again be traced to the fact that running-coupling corrections dominate the resummation functions $h_k(\xi)$ at large ξ with contributions proportional to $\xi^{k-1} h_1(\xi)$. In this regime, which corresponds to



(a) (b)

Figure 5.6: Left: Lund multiplicity distributions obtained from Monte Carlo simulations (upper panel) together with the hadron+MPI/parton ratio (lower panel) used as our estimate of the non-perturbative corrections. Results are shown for Pythia8 (with the `4C` tune), Sherpa2 and Herwig7 (with their default tune). The (green) shaded area in the bottom panel corresponds to the envelope of the individual non-perturbative corrections. Right: prediction for the average Lund multiplicity in LHC high-energy jets. The matched NNDL +NLO perturbative results are showed both with (black) and without (blue) non-perturbative corrections. The bottom panel displays the breakdown of uncertainties in their perturbative and non-perturbative contributions.

$k_{t,\text{cut}} \lesssim 4$ GeV with our kinematic cuts, one should also consider resumming these running-coupling corrections beyond their expansion to NNDL.

In practice we implement the average of the hadron/parton ratios from the five Monte Carlo setups as a multiplicative factor into the perturbative results. The envelope of these five hadron/parton ratios (the shaded region in the bottom panel of Fig. 5.6a) is used as an estimate of the uncertainties associated to non-perturbative effects. When applying non-perturbative corrections to our resummed (or NLO-matched) results, the non-perturbative uncertainties are added in quadrature with the perturbative uncertainties.

The main phenomenological result of this chapter is displayed in Fig. 5.6b where we show the average Lund multiplicity for our inclusive jet sample. We

present results at NNDL accuracy matched to NLO with (black) and without (blue) non-perturbative corrections. As expected from Fig. 5.6a, the effect of the non-perturbative corrections starts being clearly visible for $k_{t,\mathrm{cut}}$ values of a few GeV and below. The theoretical uncertainties are displayed in the lower panel of Fig. 5.6b. They are dominated by the perturbative uncertainties across the full $k_{t,\mathrm{cut}}$ range, with non-perturbative corrections being negligible for $k_{t,\mathrm{cut}} \gtrsim 4$ GeV. This suggests that there is room for further theoretical developments on the perturbative part of the calculation. This includes subleading all-order contributions ($\mathrm{N}^{k\geq 3}\mathrm{DL}$), subleading fixed-order results ($\mathrm{N}^{k\geq 2}\mathrm{LO}$) [103, 104] or multiple running-coupling correction effects discussed above and relevant for $k_{t,\mathrm{cut}} \lesssim 4$ GeV.

6
Conclusions

Today the theoretical and experimental communities are rigorously stress-testing the Standard Model in what has widely been called the precision LHC era. As experimental measurements approach, or sometimes even surpass percent-level accuracy, theoretical analytic and numerical predictions must follow suit. In this thesis we have explored both of these aspects in the context of jet substructure phenomenology. More particularly, we have first addressed the accuracy, testing and improvements to QCD parton showers, which simulate the fragmentation of partons in colliders. Finally, we have developed and resummed precision collider observables for jet substructure which provide robust tests of our understanding of QCD over a large range of scales and which can be used to further test and improve parton shower accuracy.

In Chap. 3 we have quantified the role that sub-leading colour corrections play in terms of a parton shower's accuracy. The criteria underpinning parton shower accuracy [36, 37] assert that parton showers should be able to i) correctly describe the QCD matrix element in appropriate strong-ordered limits, and ii) correctly reproduce known resummed results of collider observables in the literature. While most parton showers in the literature are formulated in an approximation of a large number of colours, $N_{\mathrm{C}} \to \infty$, residual sub-leading colour effects remain

important for parton shower accuracy as they can be commensurate with sub-leading logarithmic contributions.

In Sec. 3.2 we have focused on testing the accuracy of parton showers equipped with two new algorithms and one commonly implemented algorithm for reintroducing colour information into parton showers. We have demonstrated that the two new schemes allow NLL-large-N_c accurate parton showers to achieve NLL accuracy at full colour. Conversely, we have demonstrated the opposite for the traditional colour scheme, which leaves a $\sim$10% deviation from known fixed-order matrix elements, Fig. 3.2, and $\sim$3% deviation even at DL level when testing all-order observables, Fig. 3.3. Our discussion hinges on the availability of known resummed results in the literature, for example the NDL-resummed average subjet multiplicity, Eq. (3.2.4). As parton shower accuracy is already being explored both in e^+e^- and pp collisions at and beyond NLL accuracy [58–60], we have spent the remainder of this thesis developing and resumming sub-jet multiplicity observables.

In Chap. 4 we have presented the first theoretical determination of subjet multiplicity for angular-ordered based clustering algorithms at NNDL accuracy in e^+e^- collisions. In particular, have we explored two definitions of subjet multiplicity: (i) a novel procedure based on Lund declustering as explained in Sec. 4.1 and (ii) the more standard average jet multiplicity obtained when running the Cambridge algorithm [29] with $y_{\rm cut} = k^2_{t,\rm cut}/Q^2$. We have found that these two definitions are identical at NNDL up to a term related to the precise definition of k_t for large-angle emissions (see Eqs. (4.3.73), (4.3.76) and (4.3.79)). Our calculation thus achieves an order higher in logarithmic accuracy than the previous state-of-the-art [57].

A key aspect allowing for this improvement is the use of an angular-ordered clustering sequence instead of the typical Durham clustering algorithm. Another cornerstone of this work is the use of a novel resummation approach which does not rely on generating functionals. Instead, it is based on the observation that subleading contributions can be obtained from configurations where the subleading part is associated with only a handful of emissions — a single one giving a contribution proportional to $\alpha_s L$ at NDL, one or two giving a contribution proportional either to

α_s or to $(\alpha_s L)$ at NNDL— dressed with an arbitrary number of soft-and-collinear emissions. Once these subleading contributions have been systematically enumerated and computed (at fixed order), their all-order treatment largely recycles results from lower orders and is therefore straightforward (see e.g. Fig. 4.3). This approach can be extended, at least in principle, to higher resummation orders.

The final NNDL formula for quark ($e^+e^- \to Z \to q\bar{q}$) and gluon ($e^+e^- \to H \to gg$) hemispheres, the main results of Chap. 4, can be found in Sec. 4.3.5. Besides its intrinsic interest, this compact formula could be useful to test the logarithmic accuracy of the next-generation of NNLL parton showers. We have performed an exploratory study of the Lund multiplicity at LEP energies. To that end, the resummed predictions were additively matched to the NLO result obtained via `Event2`. We have shown that the inclusion of NNDL corrections leads to a strong reduction of the theoretical uncertainty of about 50% for almost all $k_{t,\text{cut}}$ values. Our work thus provides a precise pQCD benchmark for eventual theory-to-data comparisons. We have also shown that, after a simple inclusion of non-perturbative corrections, we obtained a decent description of the measurements of the average Cambridge multiplicity from the OPAL collaboration [75, 105].

In Chap. 5 we extended the definition and calculation of the average Lund multiplicity to the case of high-energy jets at hadron colliders by counting the mean number of subjets per anti-k_t jet with relative k_t above $k_{t,\text{cut}}$. There are two main motivations behind this. First, it provides a multiplicity-based observable that is perturbatively well-defined in QCD, and can benefit from the large energy range accessible at the LHC. Indeed, for a jet of transverse momentum $p_\perp$ and radius R, the Lund multiplicity probes energy scales from $k_{t,\text{cut}}$ values around 1 GeV up to $p_\perp R$ values of several hundreds of GeV. Second, this result is invaluable for validating the next generation of NNLL-accurate hadron-hadron parton showers.

From a theoretical standpoint, the main achievement of Chap. 5 is the all-order computation of the average Lund multiplicity in pp collisions up to NNDL accuracy, which is particularly relevant given the large range of transverse momenta probed by this observable. There are two main differences with respect to the e^+e^- event-wide

result: the notion of a jet radius, which impacts the large-angle components of the resummation starting at NDL accuracy (see Sec. 5.2.2 and 5.2.3), and the presence of experimental fiducial cuts used for the jet analysis in a collider environment (see Sec. 5.2.5). For a jet of fixed $p_\perp$ and rapidity, NNDL accuracy is reached by recycling universal contributions sensitive to collinear emissions and running coupling corrections from the results in e^+e^- collisions, and supplementing these with jet-radius effects specific to the case of high-energy jets in pp collisions. The resulting NNDL distribution for a generic $2 \to 2$ hard process, Eqs. (5.2.38)-(5.2.40), is the main theoretical result of this chapter. Reaching NNDL accuracy for a realistic situation with fiducial cuts is achieved via a simple procedure (detailed in Sec. 5.2.5).

We have performed phenomenological studies specialising our discussion to Z+jet and inclusive jet samples at the LHC. We presented (Sec. 5.3.2) predictions for the average Lund multiplicity of high-energy inclusive jets at the LHC. In order to cover the full range of $k_{t,\text{cut}}$ values, we have matched our NNDL calculation to exact NLO fixed-order results. Non-perturbative corrections have been included via a multiplicative factor extracted from general-purpose Monte Carlo event generators. The result of this procedure is shown in Fig. 5.6, which together with its e^+e^- counterpart, Fig. 4.9, forms the main phenomenological result of this thesis. Theoretical uncertainties remain below 15% down to $k_{t,\text{cut}}$ values of 1 GeV and are dominated by their perturbative component. In particular, non-perturbative uncertainties are remarkably small ($< 3\%$) for $k_{t,\text{cut}} \gtrsim 4$ GeV, with the overall uncertainty remaining under $\sim 7\%$. This leaves some margin for further theoretical improvements like the inclusion of higher-order effects such as $\mathcal{O}(\alpha_s^3)$ matching, N^{3}DL resummation, or joint resummations of running-coupling effects at small $k_{t,\text{cut}}$.

Appendices

A

Additional consideration for Lund multiplicity

A.1 Angular ordered vs k_t-based clustering algorithms

As pointed out in Sec. 4.3.1, the main difference at NNDL between k_t-based [28] and angular-ordered [29] clustering algorithms comes from configurations with multiple emissions with $k_t \sim k_{t,\text{cut}}$, Fig. 4.4l. We briefly discuss here how the presence of such a contribution drastically complicates the calculation for k_t-based algorithms.

To illustrate this, consider the case of three primary emissions off a leading quark, all with identical azimuthal angle relative to it. Take their angles such that $\theta_{3q} \gg \theta_{1q} \gg \theta_{2q}$ and assume that $k_{t,1q} \gg k_{t,\text{cut}}$ is in the double-logarithmic region, while emissions 2 and 3 are just below $k_{t,\text{cut}}$ such that $k_{t,\text{cut}}/2 < k_{t,3q} < k_{t,2q} < k_{t,\text{cut}}$. If we compute the multiplicity using a k_t-based algorithm, e.g. the Durham algorithm [28], emission 3 is first clustered with 1 and does not contribute to the multiplicity as $k_{t,3q} < k_{t,\text{cut}}$; emission 2 is then clustered with the leading parton and thus does not contribute to the multiplicity either. If we instead consider the same situation in which emission 1 is absent (e.g. virtual), emissions 2 and 3 would be clustered together resulting in a k_t of the pair above the $k_{t,\text{cut}}$. This mismatch creates a logarithmic contribution of order $(\alpha_s L^2)_1(\alpha_s L)_2(\alpha_s L)_3 = \alpha_s^3 L^4$,

i.e. NNDL. Conversely, with Cambridge clustering, emissions 2 and 3 would be clustered with the leading parton in both cases, leaving only an effect beyond NNDL accuracy when the emissions further satisfy $\theta_{23} \sim \theta_{2q}$. More generally, computing the average multiplicity for k_t-based algorithms would require knowledge of the full fragmentation process for a pair of emissions with $k_t \sim k_{t,\text{cut}}$ accompanied by an arbitrary number of soft-collinear emissions. This is a very complex task which depends in a non-trivial way on the geometry of all the emissions and could most likely only be achieved (semi-)numerically. We note that this is a more generic issue of the k_t-based algorithms, as similar considerations must be made when resumming the Durham three-jet resolution at NLL accuracy [106].

A.2 Recombination scheme independence

We comment on why the choice of recombination scheme for the initial Cambridge (e^+e^-) clustering or Cambridge/Aachen re-clustering (pp) affects the average Lund multiplicity beyond NNDL accuracy.

As a case study, we contrast the usual E-scheme, adopted in the main text, where one simply adds the 4-momenta of the two pseudo-jets, to the winner-takes-all (WTA) recombination scheme [62, 107], where the transverse momenta $p_\perp$ of the two pseudo-jets are added linearly, but the direction of the recombined jet is determined by the direction of the higher $p_\perp$ pseudo-jet. As a case study, let us consider the case of two emissions. When one emission is much softer than the other, their possible recombination would yield the same result with E-scheme and WTA recombination, up to power corrections in their relative energy fractions. This would only generate effects beyond our accuracy, including, for example, for the clustering correction of Sec. 4.3.2.4. When the emissions are strongly ordered in angles, the difference between the recombination schemes would then be power-suppressed by the ratio of the angles. This only leaves a potential effect when the two emissions have both commensurate angles and energies, i.e. the "pair" contribution from Sec. 4.3.2.3. In this case, the relative difference between the two recombination schemes would be of order 1. This would only be relevant for $k_t \sim k_{t,\text{cut}}$ which would

therefore contribute only at the N^{3}DL. To sum up, the E-scheme and WTA Lund multiplicities are the same at NNDL accuracy. The above argument would hold for any infrared-and-collinear-safe recombination scheme which would reproduce the E-scheme up to power corrections in either the soft or collinear limit.

A.3 The Cambridge jet multiplicity

In this appendix, we discuss a specific aspect which allows us to relate the Lund and Cambridge multiplicities. Specifically, we argue that if we take the full clustering tree obtained by running the Cambridge algorithm with $y_{\rm cut} = 1$, the total number of clusterings for which k_t, defined in the Lund sense, Eq. (4.1.1), is above $k_{t,\rm cut}$ is equal to the Lund multiplicity.

The only possible situation which could result in these two multiplicities to differ is one where the Lund declustering procedure hits a declustering $i \to j + k$ ($E_j > E_k$) with $k_t < k_{t,\rm cut}$ such that one of the clusterings that led to the softer branch, k, had a relative k_t above $k_{t,\rm cut}$. Indeed, in such a situation, this last clustering would be counted as part of the Cambridge multiplicity, but missed in the Lund declustering procedure as the latter would not recurse into subjet k. Since the energy can only grow throughout clustering, this situation can only happen if the clustering angles are reduced. We argue below that, even if the angles can decrease, it never creates a situation where the Lund multiplicity would miss a Cambridge clustering above $k_{t,\rm cut}$.

We start by considering a simple situation with 3 particles, p_1, p_2, p_3, at small angles (with a fourth one recoiling against this system for energy-momentum conservation). For definiteness, let us assume that p_1 and p_2 cluster first, followed by p_3 clustering with the $p_1 + p_2$ combination. We are interested in a configuration when $k_{t,12} > k_{t,\rm cut}$, but $k_{t3,1+2} < k_{t,\rm cut}$. Still without loss of generality, we can parameterise the energies as $E_1 = (1-z)z_pE$, $E_2 = (1-z)(1-z_p)E$, $E_3 = zE$ with $E = Q/2$, and assume that the angle between particles 1 and 2 is $\theta_{12} = \Delta$. The Lund procedure would first obtain the $k_{t3,1+2}$ associated with the last clustering. Next, if $z \leq 1/2$, $k_{t,12}$ would be reconstructed by following the hard branch. However,

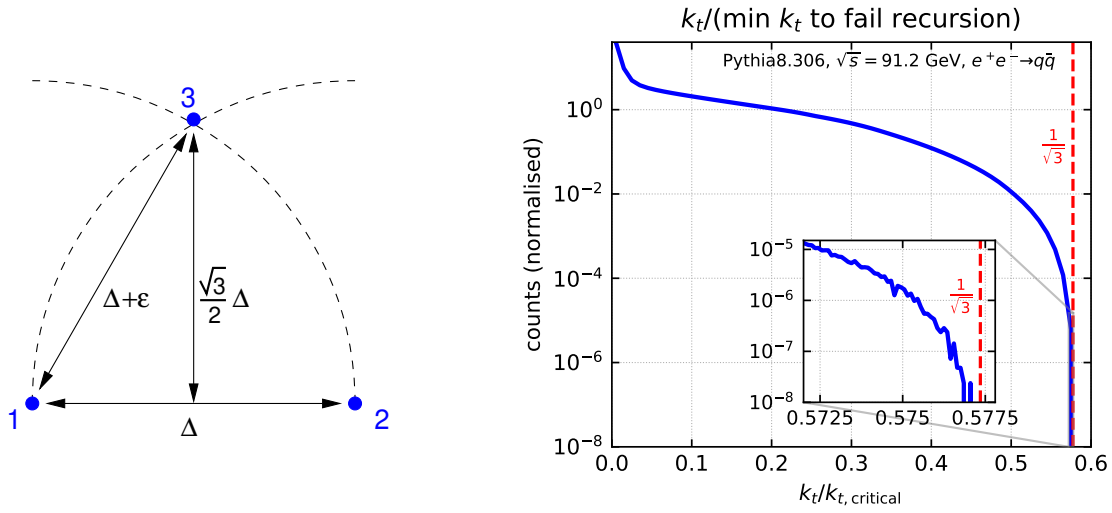


Figure A.1: Left: Sketch of a 3 particle system where angles between particles become smaller after clustering. Right: Number of events as a function of the ratio between the k_t of each declustering and the critical k_t as defined in the text. Since the number of events drops at $k_t/k_{t,\text{critical}} = 1/\sqrt{3} < 1$, this plot illustrates that the Lund multiplicity is equivalent to counting the Cambridge clusterings with a k_t above a given $k_{t,\text{cut}}$.

since $k_{t3,1+2} < k_{t,\text{cut}}$, if $z > 1/2$, the $p_1 + p_2$ clustering would be ignored. Hence, we want to show that we can never have $k_{t,12} > k_{t3,1+2}$ if $z > 1/2$, i.e. if the $p_1 + p_2$ system is on the soft branch of the final clustering.

Geometrically, the smallest possible $k_{t3,1+2}$ requires the smallest possible angular distance $\Delta_{3,1+2}$, which is achieved when p_3 is at a distance $\Delta + \varepsilon$ (with $\varepsilon \ll \Delta$) from both p_1 and p_2, as depicted in Fig. A.1. It is easy to show that, in such a configuration,

$$\frac{k_{t,21}}{k_{t3,1+2}} = \frac{z_p}{\sqrt{\frac{3}{4} + \left(\frac{1}{2} - z_p\right)^2}} \leq \frac{1}{\sqrt{3}}, \tag{A.3.1}$$

where the maximum value is reached for $z_p = 1/2$. Since this maximal value is below 1, we never face a situation where a soft branch can hide a clustering with a k_t larger than the parent one. With a bit of an effort, the above argument can be shown to hold beyond the small-angle limit, with the small-angle case still giving the extremal value [2].

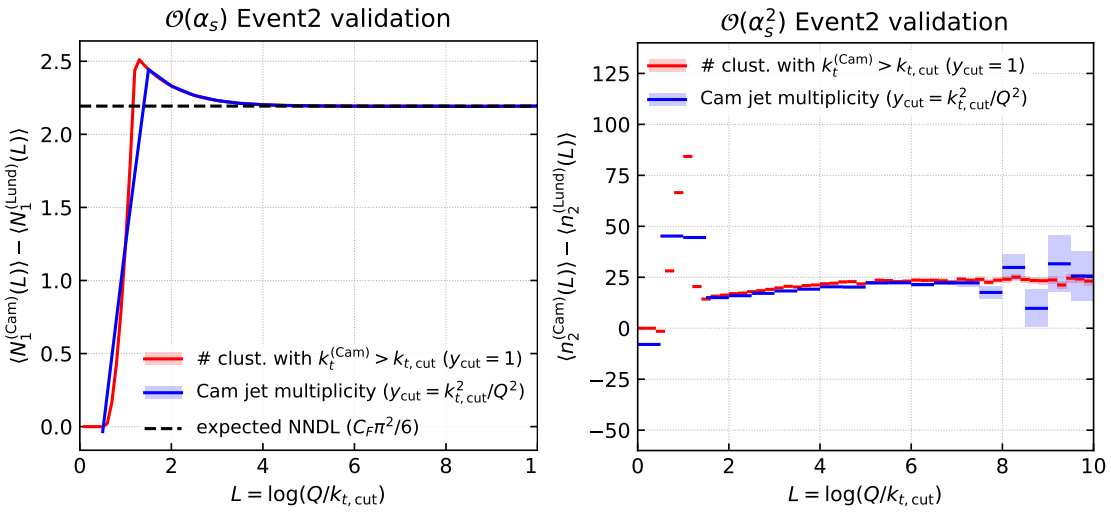
It is difficult to prove analytically that the upper bound derived in Eq. (A.3.1) is still valid for an arbitrary number of particles. Instead, we approach the problem

numerically. We run a Pythia [41] simulation of $e^+e^- \to Z \to q\bar{q}$ events at $\sqrt{s} = 91.2$ GeV and for each event reconstruct the Cambridge clustering tree. For each branching, $\mathcal{B}$, associated with a relative transverse momentum k_t, we look at all the earlier Lund declusterings for which reaching $\mathcal{B}$ would, at some point, require following a soft branch. Of these declusterings, we define $k_{t,\text{critical}}$ as the one with the smallest k_t. Seeing a value of $k_t/k_{t,\text{critical}}$ above 1 would mean that for a value of $k_{t,\text{cut}}$ between k_t and $k_{t,\text{critical}}$, the branching $\mathcal{B}$ would be counted as part of the Cambridge multiplicity but not as part of the Lund multiplicity. The distribution of $k_t/k_{t,\text{critical}}$ is plotted in Fig. A.1 and clearly shows that the upper bound in Eq. (A.3.1), derived for 3 particles, is still valid in general and that, in particular, the ratio never exceeds 1.

The above discussion shows that, if an event is clustered with the Cambridge algorithm with $y_{\text{cut}} = 1$, counting Lund declusterings with a k_t (defined as in Eq. (4.1.1)) above $k_{t,\text{cut}}$, i.e. following the algorithm defined in Sec. 4.1, is equivalent to counting declusterings satisfying the same condition in the full clustering tree. In practice, one could instead consider the Cambridge jet multiplicity, obtained by running the Cambridge algorithm with $y_{\text{cut}} = k_{t,\text{cut}}^2/Q^2$ and counting the number of resulting jets. Procedurally this is very similar to the Lund multiplicity, however it differs from it in two ways, which we can account for within the Lund multiplicity algorithm. First, we modify the definition of the relative transverse momentum to use $k_t^{(\text{Cam})}$, Eq. (4.1.2), and, second, we run the initial Cambridge clustering sequence with the recombination scheme

$$\text{recombine}\,(p_i, p_j) = \begin{cases} p_i + p_j, & \text{if } k_t < k_{t,\text{cut}} \\ \max(p_i, p_j), & \text{if } k_t > k_{t,\text{cut}} \end{cases}, \tag{A.3.2}$$

where $\max(p_i, p_j)$ is the most energetic of p_i and p_j. This describes the feature of the Cambridge algorithm that each newly resolved jet is removed from the list of particles [29], see also Sec. 2.2.1.2. We have already discussed in the main text that trading the Lund definition of k_t for $k_t^{(\text{Cam})}$ does impact the average multiplicity starting from NNDL accuracy, with the result in Eq. (4.3.39). Furthermore, the effect of the recombination scheme in Eq. (A.3.2) is beyond our targeted NNDL



(a) $\langle N\rangle$ test at $\mathcal{O}(\alpha_s)$ **(b)** $\langle n\rangle$ test at $\mathcal{O}(\alpha_s^2)$

Figure A.2: Comparison between the Lund and Cambridge multiplicities at fixed-order with the `Event2` program: (a) the (cumulative) multiplicity difference $\langle N_1^{(\mathrm{Cam})}\rangle - \langle N_1^{(\mathrm{Lund})}\rangle$ at order α_s, compared to the NNDL analytic expectation; (b) the differential multiplicity difference $\langle n_2^{(\mathrm{Cam})}\rangle - \langle n_2^{(\mathrm{Lund})}\rangle$ at order α_s^2, which is expected to go to a ($\mathrm{N^3DL}$) constant if the results agree at NNDL.

accuracy.[1] To see this, we need to consider a situation where the second line of Eq. (A.3.2) is used and see its impact on subsequent clusterings. For this to impact the counting (compared to an E-scheme approach), one should be in a situation where p_i and p_j have commensurate energies, i.e. in the case of a hard-collinear branching (with $k_t \geq k_{t,\mathrm{cut}}$). For the difference between p_i (assuming $E_i > E_j$) and $p_i + p_j$ to have an impact on the $k_{t,\mathrm{cut}}$ condition for a subsequent clustering, this new clustering must have a k_t commensurate to $k_{t,\mathrm{cut}}$ with p_i on its soft branch. This kinematic configuration is clearly beyond NNDL accuracy.

To further check the relation between the Lund and Cambridge multiplicities, we run some fixed-order tests with the `Event2` program, similarly to what was done in Sec. 4.4.1. We study the difference between the Lund multiplicity and one of the following two Cambridge-based definitions: (i) running the Cambridge algorithm with $y_{\mathrm{cut}} = 1$ and counting the clusterings with $k_t^{(\mathrm{Cam})} > k_{t,\mathrm{cut}}$, i.e. using the Cambridge definition of k_t instead of the Lund definition, and (ii) using

[1] Note that the recombination scheme in Eq. (A.3.2) does not satisfy the criteria discussed at the end of App. A.2.

the Cambridge jet multiplicity with $y_{\text{cut}} = k_{t,\text{cut}}^2/Q^2$. Our results are shown in Fig. A.2. In Fig. A.2a, we plot differences between the multiplicities at order α_s. We see that the Lund and Cambridge multiplicities indeed differ by a constant which corresponds to the NNDL expectation of $C_F\pi^2/6$ for the full event, cf. Sec. 4.3.2.5, Eq. (4.3.39). At $\mathcal{O}\left(\alpha_s^2\right)$, Fig. A.2b, we instead consider the difference in the differential multiplicity (as done in Fig. 4.7b, Sec. 4.4.1). The fact that the differences tend to a constant at large L indicates that the two distributions agree at NNDL accuracy, as expected from our analytic calculations.

References

[1] Keith Hamilton et al. "Colour and logarithmic accuracy in final-state parton showers". In: *JHEP* 03.041 (2021), p. 041. arXiv: 2011.10054 [hep-ph].

[2] Rok Medves, Alba Soto-Ontoso, and Gregory Soyez. "Lund and Cambridge multiplicities for precision physics". In: *JHEP* 10 (2022), p. 156. arXiv: 2205.02861 [hep-ph].

[3] Rok Medves, Alba Soto-Ontoso, and Gregory Soyez. "Lund multiplicity in QCD jets". In: *JHEP* 04 (2023), p. 104. arXiv: 2212.05076 [hep-ph].

[4] P. Azzi et al. "Report from Working Group 1". In: *CERN Yellow Rep. Monogr.* 7 (2019), pp. 1–220. arXiv: 1902.04070 [hep-ph].

[5] M. Cepeda et al. "Report from Working Group 2". In: *CERN Yellow Rep. Monogr.* 7 (2019), pp. 221–584. arXiv: 1902.00134 [hep-ph].

[6] Xabier Cid Vidal et al. "Report from Working Group 3". In: *CERN Yellow Rep. Monogr.* 7 (2019), pp. 585–865. arXiv: 1812.07831 [hep-ph].

[7] Roman Kogler et al. "Jet Substructure at the Large Hadron Collider: Experimental Review". In: *Rev. Mod. Phys.* 91.4 (2019), p. 045003. arXiv: 1803.06991 [hep-ex].

[8] Simone Marzani, Gregory Soyez, and Michael Spannowsky. *Looking inside jets: an introduction to jet substructure and boosted-object phenomenology*. Vol. 958. Springer, 2019. arXiv: 1901.10342 [hep-ph].

[9] R. K. Ellis, W. J. Stirling, and B. R. Webber. *QCD and Collider Physics*. Cambridge Monographs on Particle Physics, Nuclear Physics and Cosmology. Cambridge University Press, 1996.

[10] P.A. Baikov, K.G. Chetyrkin, and J.H. Kühn. "Five-Loop Running of the QCD coupling constant". In: *Phys. Rev. Lett.* 118.8 (2017), p. 082002. arXiv: 1606.08659 [hep-ph].

[11] Thomas Luthe et al. "Towards the five-loop Beta function for a general gauge group". In: *JHEP* 07 (2016), p. 127. arXiv: 1606.08662 [hep-ph].

[12] Thomas Luthe et al. "The five-loop Beta function for a general gauge group and anomalous dimensions beyond Feynman gauge". In: *JHEP* 10 (2017), p. 166. arXiv: 1709.07718 [hep-ph].

[13] F. Herzog et al. "The five-loop beta function of Yang-Mills theory with fermions". In: *JHEP* 02 (2017), p. 090. arXiv: 1701.01404 [hep-ph].

[14] K. G. Chetyrkin et al. "Five-loop renormalisation of QCD in covariant gauges". In: *JHEP* 10 (2017). [Addendum: JHEP 12, 006 (2017)], p. 179. arXiv: 1709.08541 [hep-ph].

[15] D. d'Enterria et al. "The strong coupling constant: State of the art and the decade ahead". In: (Mar. 2022). arXiv: 2203.08271 [hep-ph].

[16] R. L. Workman et al. "Review of Particle Physics". In: *PTEP* 2022 (2022), p. 083C01.

[17] T. Kinoshita. "Mass singularities of Feynman amplitudes". In: *J. Math. Phys.* 3 (1962), pp. 650–677.

[18] T. D. Lee and M. Nauenberg. "Degenerate Systems and Mass Singularities". In: *Phys. Rev.* 133 (1964). Ed. by G. Feinberg, B1549–B1562.

[19] Victor S. Fadin. "DOUBLE LOGARITHMIC ASYMPTOTICS OF THE CROSS-SECTIONS OF E+ E- ANNIHILATION INTO QUARKS AND GLUONS. (IN RUSSIAN)". In: *Yad. Fiz.* 37 (1983), pp. 408–423.

[20] B. I. Ermolaev and Victor S. Fadin. "Log - Log Asymptotic Form of Exclusive Cross-Sections in Quantum Chromodynamics". In: *JETP Lett.* 33 (1981), pp. 269–272.

[21] Alfred H. Mueller. "On the Multiplicity of Hadrons in QCD Jets". In: *Phys. Lett. B* 104 (1981), pp. 161–164.

[22] Yuri L. Dokshitzer, Victor S. Fadin, and Valery A. Khoze. "Double Logs of Perturbative QCD for Parton Jets and Soft Hadron Spectra". In: *Z. Phys. C* 15 (1982), p. 325.

[23] A. Bassetto, M. Ciafaloni, and G. Marchesini. "Jet Structure and Infrared Sensitive Quantities in Perturbative QCD". In: *Phys. Rept.* 100 (1983), pp. 201–272.

[24] Yakov I. Azimov et al. "Similarity of Parton and Hadron Spectra in QCD Jets". In: *Z. Phys. C* 27 (1985), pp. 65–72.

[25] Gavin P. Salam. "Towards Jetography". In: *Eur. Phys. J. C* 67 (2010), pp. 637–686. arXiv: 0906.1833 [hep-ph].

[26] John C. Collins, Davison E. Soper, and George F. Sterman. "Factorization of Hard Processes in QCD". In: *Adv. Ser. Direct. High Energy Phys.* 5 (1989), pp. 1–91. arXiv: hep-ph/0409313.

[27] John C. Collins, Davison E. Soper, and George F. Sterman. "Factorization for Short Distance Hadron - Hadron Scattering". In: *Nucl. Phys. B* 261 (1985), pp. 104–142.

[28] S. Catani et al. "New clustering algorithm for multi - jet cross-sections in e^+e^- annihilation". In: *Phys. Lett.* B269 (1991), pp. 432–438.

[29] Yuri L. Dokshitzer et al. "Better jet clustering algorithms". In: *JHEP* 08 (1997), p. 001. arXiv: hep-ph/9707323 [hep-ph].

[30] M. Wobisch and T. Wengler. "Hadronization corrections to jet cross-sections in deep inelastic scattering". In: *Workshop on Monte Carlo Generators for HERA Physics (Plenary Starting Meeting)*. Apr. 1998, pp. 270–279. arXiv: hep-ph/9907280.

[31] Matteo Cacciari, Gavin P. Salam, and Gregory Soyez. "The anti-k_t jet clustering algorithm". In: *JHEP* 04 (2008), p. 063. arXiv: 0802.1189 [hep-ph].

[32] Bo Andersson et al. “Coherence Effects in Deep Inelastic Scattering”. In: *Z. Phys.* C43 (1989), p. 625.

[33] Frédéric A. Dreyer, Gavin P. Salam, and Grégory Soyez. “The Lund Jet Plane”. In: *JHEP* 12 (2018), p. 064. arXiv: 1807.04758 [hep-ph].

[34] S. Catani et al. “Resummation of large logarithms in e+ e- event shape distributions”. In: *Nucl. Phys.* B407 (1993), pp. 3–42.

[35] Andy Buckley et al. “General-purpose event generators for LHC physics”. In: *Phys. Rept.* 504 (2011), pp. 145–233. arXiv: 1101.2599 [hep-ph].

[36] Mrinal Dasgupta et al. “Logarithmic accuracy of parton showers: a fixed-order study”. In: *JHEP* 09 (2018), p. 033. arXiv: 1805.09327 [hep-ph].

[37] Mrinal Dasgupta et al. “Parton showers beyond leading logarithmic accuracy”. In: *Phys. Rev. Lett.* 125.5 (2020), p. 052002. arXiv: 2002.11114 [hep-ph].

[38] Georges Aad et al. “Jet energy measurement and its systematic uncertainty in proton-proton collisions at $\sqrt{s} = 7$ TeV with the ATLAS detector”. In: *Eur. Phys. J. C* 75 (2015), p. 17. arXiv: 1406.0076 [hep-ex].

[39] Vardan Khachatryan et al. “Jet energy scale and resolution in the CMS experiment in pp collisions at 8 TeV”. In: *JINST* 12.02 (2017), P02014. arXiv: 1607.03663 [hep-ex].

[40] Gosta Gustafson and Ulf Pettersson. “Dipole Formulation of QCD Cascades”. In: *Nucl. Phys.* B306 (1988), pp. 746–758.

[41] Torbjörn Sjöstrand et al. “An Introduction to PYTHIA 8.2”. In: *Comput. Phys. Commun.* 191 (2015), pp. 159–177. arXiv: 1410.3012 [hep-ph].

[42] Enrico Bothmann et al. “Event Generation with Sherpa 2.2”. In: *SciPost Phys.* 7.3 (2019), p. 034. arXiv: 1905.09127 [hep-ph].

[43] G. Marchesini and B. R. Webber. “Monte Carlo Simulation of General Hard Processes with Coherent QCD Radiation”. In: *Nucl. Phys.* B310 (1988), pp. 461–526.

[44] G. Corcella et al. "HERWIG 6: An Event generator for hadron emission reactions with interfering gluons (including supersymmetric processes)". In: *JHEP* 01 (2001), p. 010. arXiv: hep-ph/0011363 [hep-ph].

[45] Johannes Bellm et al. "Herwig 7.2 release note". In: *Eur. Phys. J. C* 80.5 (2020), p. 452. arXiv: 1912.06509 [hep-ph].

[46] Gavin Bewick et al. "Logarithmic Accuracy of Angular-Ordered Parton Showers". In: (2019). arXiv: 1904.11866 [hep-ph].

[47] M. Dasgupta and G.P. Salam. "Resummation of nonglobal QCD observables". In: *Phys. Lett. B* 512 (2001), pp. 323–330. arXiv: hep-ph/0104277.

[48] Andrea Banfi, Gennaro Corcella, and Mrinal Dasgupta. "Angular ordering and parton showers for non-global QCD observables". In: *JHEP* 03 (2007), p. 050. arXiv: hep-ph/0612282 [hep-ph].

[49] Zoltan Nagy and Davison E. Soper. "Summations of large logarithms by parton showers". In: (Nov. 2020). arXiv: 2011.04773 [hep-ph].

[50] Zoltan Nagy and Davison E. Soper. "Summations by parton showers of large logarithms in electron-positron annihilation". In: (Nov. 2020). arXiv: 2011.04777 [hep-ph].

[51] Jeffrey R. Forshaw, Jack Holguin, and Simon Plätzer. "Building a consistent parton shower". In: *JHEP* 09 (2020), p. 014. arXiv: 2003.06400 [hep-ph].

[52] Andrea Banfi, Gavin P. Salam, and Giulia Zanderighi. "Principles of general final-state resummation and automated implementation". In: *JHEP* 03 (2005), p. 073. arXiv: hep-ph/0407286 [hep-ph].

[53] T. Sjostrand and Peter Z. Skands. "Transverse-momentum-ordered showers and interleaved multiple interactions". In: *Eur. Phys. J.* C39 (2005), pp. 129–154. arXiv: hep-ph/0408302 [hep-ph].

[54] Stefan Hoeche and Stefan Prestel. "The midpoint between dipole and parton showers". In: *Eur. Phys. J.* C75.9 (2015), p. 461. arXiv: 1506.05057 [hep-ph].

[55] Christer Friberg, Gosta Gustafson, and Jari Hakkinen. "Color connections in e^+e^- annihilation". In: *Nucl. Phys.* B490 (1997), pp. 289–305. arXiv: hep-ph/9604347 [hep-ph].

[56] Gosta Gustafson. "Multiplicity distributions in QCD cascades". In: *Nucl. Phys.* B392 (1993), pp. 251–280.

[57] S. Catani et al. "Average number of jets in e+ e- annihilation". In: *Nucl. Phys.* B377 (1992), pp. 445–460.

[58] Melissa van Beekveld et al. "PanScales parton showers for hadron collisions: formulation and fixed-order studies". In: *JHEP* 11 (2022), p. 019. arXiv: 2205.02237 [hep-ph].

[59] Melissa van Beekveld et al. "PanScales showers for hadron collisions: all-order validation". In: *JHEP* 11 (2022), p. 020. arXiv: 2207.09467 [hep-ph].

[60] Keith Hamilton et al. "Matching and event-shape NNDL accuracy in parton showers". In: *JHEP* 03 (2023), p. 224. arXiv: 2301.09645 [hep-ph].

[61] Bo Andersson, Per Dahlkvist, and Gosta Gustafson. "AN INFRARED STABLE MULTIPLICITY MEASURE ON QCD PARTON STATES". In: *Phys. Lett. B* 214 (1988), pp. 604–608.

[62] Andrew J. Larkoski, Duff Neill, and Jesse Thaler. "Jet Shapes with the Broadening Axis". In: *JHEP* 04 (2014), p. 017. arXiv: 1401.2158 [hep-ph].

[63] S. Catani, Yuri L. Dokshitzer, and B.R. Webber. "Average number of jets in deep inelastic scattering". In: *Phys. Lett. B* 322 (1994), pp. 263–269.

[64] Guido Altarelli and G. Parisi. "Asymptotic Freedom in Parton Language". In: *Nucl. Phys.* B126 (1977), pp. 298–318.

[65] Yuri L. Dokshitzer et al. *Basics of perturbative QCD*. Editions frontières, 1991.

[66] S. D. Badger, E. W. Nigel Glover, and Valentin V. Khoze. "MHV rules for Higgs plus multi-parton amplitudes". In: *JHEP* 03 (2005), p. 023. arXiv: hep-th/0412275.

[67] W. Bartel et al. “Experimental Studies on Multi-Jet Production in e+ e- Annihilation at PETRA Energies”. In: *Z. Phys. C* 33 (1986). Ed. by J. Tran Thanh Van, p. 23.

[68] S. Catani, B. R. Webber, and G. Marchesini. “QCD coherent branching and semiinclusive processes at large x”. In: *Nucl. Phys.* B349 (1991), pp. 635–654.

[69] Mrinal Dasgupta and Basem Kamal El-Menoufi. “Dissecting the collinear structure of quark splitting at NNLL”. In: *JHEP* 12 (2021), p. 158. arXiv: 2109.07496 [hep-ph].

[70] Yuri L. Dokshitzer, G. Marchesini, and G. Oriani. “Measuring color flows in hard processes: Beyond leading order”. In: *Nucl. Phys.* B387 (1992), pp. 675–714.

[71] Stefano Catani and Massimiliano Grazzini. “Infrared factorization of tree level QCD amplitudes at the next-to-next-to-leading order and beyond”. In: *Nucl. Phys.* B570 (2000), pp. 287–325. arXiv: hep-ph/9908523 [hep-ph].

[72] Keith Hamilton et al. “Soft spin correlations in final-state parton showers”. In: *JHEP* 03 (2022), p. 193. arXiv: 2111.01161 [hep-ph].

[73] S. Catani and M. H. Seymour. “The Dipole formalism for the calculation of QCD jet cross-sections at next-to-leading order”. In: *Phys. Lett.* B378 (1996), pp. 287–301. arXiv: hep-ph/9602277 [hep-ph].

[74] S. Catani and M. H. Seymour. “A General algorithm for calculating jet cross-sections in NLO QCD”. In: *Nucl. Phys.* B485 (1997). [Erratum: Nucl. Phys.B510,503(1998)], pp. 291–419. arXiv: hep-ph/9605323 [hep-ph].

[75] P. Pfeifenschneider et al. “QCD analyses and determinations of alpha(s) in e+ e- annihilation at energies between 35-GeV and 189-GeV”. In: *Eur. Phys. J. C* 17 (2000), pp. 19–51. arXiv: hep-ex/0001055.

[76] Christian Bierlich et al. “A comprehensive guide to the physics and usage of PYTHIA 8.3”. In: (Mar. 2022). arXiv: 2203.11601 [hep-ph].

[77] M. Bahr et al. “Herwig++ Physics and Manual”. In: *Eur. Phys. J.* C58 (2008), pp. 639–707. arXiv: 0803.0883 [hep-ph].

[78] Johannes Bellm et al. "Herwig 7.0/Herwig++ 3.0 release note". In: *Eur. Phys. J.* C76.4 (2016), p. 196. arXiv: 1512.01178 [hep-ph].

[79] Erik Gerwick et al. "Soft evolution of multi-jet final states". In: *JHEP* 02 (2015), p. 106. arXiv: 1411.7325 [hep-ph].

[80] Yi Chen et al. "Jet energy spectrum and substructure in e^+e^- collisions at 91.2 GeV with ALEPH Archived Data". In: (Nov. 2021). arXiv: 2111.09914 [hep-ex].

[81] Anthony Badea et al. "Measurements of two-particle correlations in e^+e^- collisions at 91 GeV with ALEPH archived data". In: *Phys. Rev. Lett.* 123.21 (2019), p. 212002. arXiv: 1906.00489 [hep-ex].

[82] Georges Aad et al. "Measurement of the Lund Jet Plane Using Charged Particles in 13 TeV Proton-Proton Collisions with the ATLAS Detector". In: *Phys. Rev. Lett.* 124.22 (2020), p. 222002. arXiv: 2004.03540 [hep-ex].

[83] Andrew Lifson, Gavin P. Salam, and Gregory Soyez. "Calculating the primary Lund Jet Plane density". In: *JHEP* 10 (2020), p. 170. arXiv: 2007.06578 [hep-ph].

[84] Frédéric A. Dreyer and Huilin Qu. "Jet tagging in the Lund plane with graph networks". In: *JHEP* 03 (2021), p. 052. arXiv: 2012.08526 [hep-ph].

[85] Frédéric A. Dreyer, Gregory Soyez, and Adam Takacs. "Quarks and gluons in the Lund plane". In: *JHEP* 08 (2022), p. 177. arXiv: 2112.09140 [hep-ph].

[86] Georges Aad et al. "Measurement of the charged-particle multiplicity inside jets from $\sqrt{s} = 8$ TeV pp collisions with the ATLAS detector". In: *Eur. Phys. J. C* 76.6 (2016), p. 322. arXiv: 1602.00988 [hep-ex].

[87] Armen Tumasyan et al. "Study of quark and gluon jet substructure in Z+jet and dijet events from pp collisions". In: *JHEP* 01 (2022), p. 188. arXiv: 2109.03340 [hep-ex].

[88] Morad Aaboud et al. "Measurement of jet-substructure observables in top quark, W boson and light jet production in proton-proton collisions at $\sqrt{s} = 13$ TeV with the ATLAS detector". In: *JHEP* 08 (2019), p. 033. arXiv: 1903.02942 [hep-ex].

[89] M. Aaboud et al. "Jet energy scale measurements and their systematic uncertainties in proton-proton collisions at $\sqrt{s} = 13$ TeV with the ATLAS detector". In: *Phys. Rev. D* 96.7 (2017), p. 072002. arXiv: 1703.09665 [hep-ex].

[90] R. Keith Ellis, G. Marchesini, and B. R. Webber. "Soft Radiation in Parton Parton Scattering". In: *Nucl. Phys. B* 286 (1987). [Erratum: Nucl.Phys.B 294, 1180 (1987)], p. 643.

[91] Mrinal Dasgupta et al. "On jet mass distributions in Z+jet and dijet processes at the LHC". In: *JHEP* 10 (2012), p. 126. arXiv: 1207.1640 [hep-ph].

[92] Y. Hatta et al. "Resumming double non-global logarithms in the evolution of a jet". In: *JHEP* 02 (2018), p. 075. arXiv: 1710.06722 [hep-ph].

[93] Matteo Cacciari, Gavin P. Salam, and Gregory Soyez. "FastJet User Manual". In: *Eur. Phys. J.* C72 (2012), p. 1896. arXiv: 1111.6097 [hep-ph].

[94] J. Alwall et al. "The automated computation of tree-level and next-to-leading order differential cross sections, and their matching to parton shower simulations". In: *JHEP* 07 (2014), p. 079. arXiv: 1405.0301 [hep-ph].

[95] Zoltan Nagy. "Next-to-leading order calculation of three jet observables in hadron hadron collision". In: *Phys. Rev. D* 68 (2003), p. 094002. arXiv: hep-ph/0307268.

[96] Andrea Banfi, Gavin P. Salam, and Giulia Zanderighi. "Accurate QCD predictions for heavy-quark jets at the Tevatron and LHC". In: *JHEP* 07 (2007), p. 026. arXiv: 0704.2999 [hep-ph].

[97] Richard D. Ball et al. "The PDF4LHC21 combination of global PDF fits for the LHC Run III". In: *J. Phys. G* 49.8 (2022), p. 080501. arXiv: 2203.05506 [hep-ph].

[98] Samuel Bright-Thonney and Benjamin Nachman. "Investigating the Topology Dependence of Quark and Gluon Jets". In: *JHEP* 03 (2019), p. 098. arXiv: 1810.05653 [hep-ph].

[99] M. Cacciari et al. "The t anti-t cross-section at 1.8-TeV and 1.96-TeV: A Study of the systematics due to parton densities and scale dependence". In: *JHEP* 04 (2004), p. 068. arXiv: hep-ph/0303085.

[100] Peter Skands, Stefano Carrazza, and Juan Rojo. "Tuning PYTHIA 8.1: the Monash 2013 Tune". In: *Eur. Phys. J. C* 74.8 (2014), p. 3024. arXiv: 1404.5630 [hep-ph].

[101] Richard Corke and Torbjorn Sjostrand. "Interleaved Parton Showers and Tuning Prospects". In: *JHEP* 03 (2011), p. 032. arXiv: 1011.1759 [hep-ph].

[102] *ATLAS Pythia 8 tunes to 7 TeV data*. Tech. rep. All figures including auxiliary figures are available at https://atlas.web.cern.ch/Atlas/GROUPS/PHYSICS/PUBNOTES/ATL-PHYS-PUB-2014-021. Geneva: CERN, 2014.

[103] S. Abreu et al. "Leading-color two-loop QCD corrections for three-jet production at hadron colliders". In: *JHEP* 07 (2021), p. 095. arXiv: 2102.13609 [hep-ph].

[104] Michal Czakon, Alexander Mitov, and Rene Poncelet. "Next-to-Next-to-Leading Order Study of Three-Jet Production at the LHC". In: *Phys. Rev. Lett.* 127.15 (2021). [Erratum: Phys.Rev.Lett. 129, 119901 (2022), Erratum: Phys.Rev.Lett. 129, 119901 (2022)], p. 152001. arXiv: 2106.05331 [hep-ph].

[105] G. Abbiendi et al. "Determination of alpha(s) using jet rates at LEP with the OPAL detector". In: *Eur. Phys. J. C* 45 (2006), pp. 547–568. arXiv: hep-ex/0507047.

[106] A. Banfi, G. P. Salam, and G. Zanderighi. "Semi-numerical resummation of event shapes". In: *JHEP* 01 (2002), p. 018. arXiv: hep-ph/0112156 [hep-ph].

[107] Daniele Bertolini, Tucker Chan, and Jesse Thaler. "Jet Observables Without Jet Algorithms". In: *JHEP* 04 (2014), p. 013. arXiv: 1310.7584 [hep-ph].